Received OSTI
SEP 21 1992

NUREG/CR-5840
ANL-92/3

FASTGRASS: A Mechanistic Model for the Prediction of Xe, I, Cs, Te, Ba, and Sr Release from Nuclear Fuel under Normal and Severe-Accident Conditions

User's Guide for Mainframe, Workstation, and Personal Computer Applications

Prepared by
J. Rest, S. A. Zawadzki

Argonne National Laboratory

Prepared for
U.S. Nuclear Regulatory Commission

DISTRIBUTION OF THIS DOCUMENT IS UNLIMITED

DISCLAIMER

This report was prepared as an account of work sponsored by an agency of the United States Government. Neither the United States Government nor any agency Thereof, nor any of their employees, makes any warranty, express or implied, or assumes any legal liability or responsibility for the accuracy, completeness, or usefulness of any information, apparatus, product, or process disclosed, or represents that its use would not infringe privately owned rights. Reference herein to any specific commercial product, process, or service by trade name, trademark, manufacturer, or otherwise does not necessarily constitute or imply its endorsement, recommendation, or favoring by the United States Government or any agency thereof. The views and opinions of authors expressed herein do not necessarily state or reflect those of the United States Government or any agency thereof.

DISCLAIMER

Portions of this document may be illegible in electronic image products. Images are produced from the best available original document.

AVAILABILITY NOTICE

Availability of Reference Materials Cited in NRC Publications

Most documents cited in NRC publications will be available from one of the following sources:

1. The NRC Public Document Room, 2120 L Street, NW., Lower Level, Washington, DC 20555

2. The Superintendent of Documents, U.S. Government Printing Office, P.O. Box 37082, Washington, DC 20013-7082

3. The National Technical Information Service, Springfield, VA 22161

Although the listing that follows represents the majority of documents cited in NRC publications, it is not intended to be exhaustive.

Referenced documents available for inspection and copying for a fee from the NRC Public Document Room include NRC correspondence and internal NRC memoranda; NRC bulletins, circulars, information notices, inspection and investigation notices; licensee event reports; vendor reports and correspondence; Commission papers; and applicant and licensee documents and correspondence.

The following documents in the NUREG series are available for purchase from the GPO Sales Program: formal NRC staff and contractor reports, NRC-sponsored conference proceedings, international agreement reports, grant publications, and NRC booklets and brochures. Also available are regulatory guides, NRC regulations in the *Code of Federal Regulations*, and *Nuclear Regulatory Commission Issuances*.

Documents available from the National Technical Information Service include NUREG-series reports and technical reports prepared by other Federal agencies and reports prepared by the Atomic Energy Commission, forerunner agency to the Nuclear Regulatory Commission.

Documents available from public and special technical libraries include all open literature items, such as books, journal articles, and transactions. *Federal Register* notices, Federal and State legislation, and congressional reports can usually be obtained from these libraries.

Documents such as theses, dissertations, foreign reports and translations, and non-NRC conference proceedings are available for purchase from the organization sponsoring the publication cited.

Single copies of NRC draft reports are available free, to the extent of supply, upon written request to the Office of Administration, Distribution and Mail Services Section, U.S. Nuclear Regulatory Commission, Washington, DC 20555.

Copies of industry codes and standards used in a substantive manner in the NRC regulatory process are maintained at the NRC Library, 7920 Norfolk Avenue, Bethesda, Maryland, for use by the public. Codes and standards are usually copyrighted and may be purchased from the originating organization or, if they are American National Standards, from the American National Standards Institute, 1430 Broadway, New York, NY 10018.

DISCLAIMER NOTICE

This report was prepared as an account of work sponsored by an agency of the United States Government. Neither the United States Government nor any agency thereof, or any of their employees, makes any warranty, expressed or implied, or assumes any legal liability of responsibility for any third party's use, or the results of such use, of any information, apparatus, product or process disclosed in this report, or represents that its use by such third party would not infringe privately owned rights.

NUREG/CR--5840

TI92 040783

FASTGRASS: A Mechanistic Model for the Prediction of Xe, I, Cs, Te, Ba, and Sr Release from Nuclear Fuel under Normal and Severe-Accident Conditions

User's Guide for Mainframe, Workstation, and Personal Computer Applications

Manuscript Completed: April 1992
Date Published: September 1992

Prepared by
J. Rest, S. A. Zawadzki

Argonne National Laboratory
9700 South Cass Avenue
Argonne, IL 60439

Prepared for
Division of Systems Research
Office of Nuclear Regulatory Research
U.S. Nuclear Regulatory Commission
Washington, DC 20555
NRC FIN A2271

MASTER

DISTRIBUTION OF THIS DOCUMENT IS UNLIMITED

Previous Documents In Series

J. Rest, GRASS-SST: A Comprehensive, Mechanistic Model for the Prediction of Fission-Gas Behavior in UO_2-base Fuels during Steady-State and Transient Conditions, NUREG/CR-0202, ANL-78-53 (June 1978).

FASTGRASS: A Mechanistic Model for the Prediction of Xe, I, Cs, Te, Ba, and Sr Release from Nuclear Fuel under Normal and Severe-Accident Conditions

User's Guide for Mainframe,

Workstation, and Personal Computer Applications

by

J. Rest and S. A. Zawadzki

Abstract

The primary physical/chemical models that form the basis of the FASTGRASS mechanistic computer model for calculating fission-product release from nuclear fuel are described. Calculated results are compared with test data and the major mechanisms affecting the transport of fission products during steady-state and accident conditions are identified.

Table of Contents

Abstract iii

Nomenclature xiii

Executive Summary 1

1 Introduction 3

2 FASTGRASS Theory of Fission-Gas Behavior in Solid Fuel 6

2.1 Intragranular Fission Gas 8

2.2 Intergranular Fission Gas: Grain Faces 14

2.3 Intergranular Fission Gas: Grain Edges 15

2.4 Calculation of Average Number of Atoms per Bubble N_b, N_f, and N_e 17

2.5 Fission-Gas Release 18

2.6 Options for Calculating Bubble Radii 18

2.6.1 General Formulation 18

2.6.2 Van der Waals Equation of State 19

2.6.3 Harrison's Extrapolated Equation of State 21

2.6.4 Modified Hard-Sphere Equation of State 21

2.7 Grain Growth/Grain-Boundary Sweeping 23

2.8 Fuel Oxidation Effects 29

3 FASTGRASS Theory of Fission-Gas Behavior in Solid Fuel: Precipitation-Hindering Option 29

3.1 Introduction 29

3.2 Model X: the Conventional Model 32

3.3 Model Y: Modified Calculation of Gas Precipitation in Solids..... 33

3.4 Effect of Materials Properties on the Conventional-Model Calculation of Gas Precipitation in Solids..... 36

4 Validation 1: Behavior of Fission Gas during Postirradiation Annealing Experiments..... 37

4.1 Data Base Selection for Validation of Models X, Y, and Z..... 37

4.2 Comparison of Models X, Y, and Z for Gas Precipitation in Solids..... 43

4.2.1 Simulation of In-Reactor Irradiation..... 44

4.2.2 Simulation of Postirradiation Annealing Experiments..... 47

4.3 Discussion..... 52

4.4 In-Pile Gas Release..... 56

4.5 Average Size of Fission-Gas Bubbles..... 58

4.6 Retained Fission Gas..... 59

4.7 Fission-Gas Swelling..... 61

4.8 Microcracking during Transient Conditions..... 62

4.9 Transient Fission-Gas Release..... 66

5 FASTGRASS Theory of Fission-Product Behavior in Solid Fuel: UO_2/Fission-Product Chemistry..... 68

6 FASTGRASS Theory of Gas Bubble Behavior in Degraded Fuel..... 75

6.1 Effect of Fuel Liquefaction..... 75

6.2 Effect of Fuel Dissolution..... 76

7 Validation 2: Comparison between Predictions and Data for Fission-Product Release during Severe-Accident Conditions..... 82

7.1 Comparison with Out-of-Reactor Data..... 82

7.1.1 Data of Parker and Barton 82

7.1.2 Fission-Product Behavior in High-Burnup Fuel during ORNL In-Cell Heating Tests with No Fuel Liquefaction 84

7.1.3 Fission-Product Behavior in High-Burnup Fuel during ORNL In-Cell Heating Tests with Fuel Liquefaction 89

7.2 Comparison with In-Reactor Data 91

7.2.1 Fission-Product Behavior in Trace-Irradiated Fuel during SFD Tests in the PBF Reactor with No Fuel Liquefaction 91

7.2.2 Fission-Product Behavior in Trace-Irradiated and High-Burnup Fuel during SFD Tests in the PBF Reactor with Fuel Liquefaction 95

8 Comparison of FASTGRASS with Empirical Models 102

9 FASTGRASS Input Description 107

10 FASTGRASS Output Description 123

11 CONCLUSIONS 129

APPENDIX A: FASTGRASS Model for Determining Ductile/Brittle Fuel Response 131

APPENDIX B: Solution of Harrison's Equation of State with Capillarity Equation 134

APPENDIX C: Gas Release Data 140

APPENDIX D: Mobility of Fission-Gas Bubbles during Normal and Transient Conditions 145

12 References 150

List of Figures

1. Configuration of the two-zone model 10

2. Method of Regula Falsi 20

3. The results of MINITAB regression analyses for data (individual) from Refs. 35–42 and Tables C1–C8 39

4. The results of MINITAB regression analyses for data (total) from Refs. 35–42 and Tables C1–C8 45

5. Fractional gas release for the postirradiation annealing experiments of G. J. Small 48

6. Fractional gas release as a function of as-irradiated burnup for the postirradiation annealing experiments of Burbach and Zimmermann 51

7. Mean bubble diameter, calculated with FASTGRASS Models X and Y, compared with measured values from Ref. 35 53

8. Intragranular bubble density as a function of mean bubble diameter for anneal times of 300 and 900 s 53

9. Fractional gas release, fraction of gas retained in grain lattice, and fraction of gas in fission-gas bubbles as a function of time 55

10. Bubble excess pressure as a function of time for three values of the hold temperature, calculated with FASTGRASS Model Y 56

11. Fractional gas release as a function of time for the Small 2000°C postirradiation anneal experiment 56

12. Predicted fractional fission-gas release at 1250, 1500, 1750, and 2000 K 57

13. Comparison of theoretical predictions with measured end-of-life gas release 58

14. Predicted average bubble size 58

15. Predicted retained fission gas at 3 and 12 at.% burnup 60

16. Predicted retained fission gas in matrix at 3 and 12 at.% burnup 60

17. Predicted retained fission gas in pores at 3 and 12 at.% burnup 61

18. Predicted swelling rates as a function of fuel temperature for burnups of 0–1% and 1–2% 62

19. Predicted swelling rates as a function of fuel temperature for burnups of 2–3%, 3–4%, and 4–5% 63

20. Interrelationship between fuel fracturing, temperature scenario, and fission-gas-bubble response 64

21. Predictions of pore–solid surface area, S_V, as a function of pellet radius for Tests 22 and 32 65

22. Predictions of pore–solid surface area, S_V, as a function of pellet radius for Tests 24 and 29 65

23. Predictions of pore–solid surface area, S_V, as a function of pellet radius for Tests 33 and 37 66

24. Predictions of the theory of transient gas release vs. experimentally measured values from ten DEH tests 67

25. Equilibrium pseudobinary phase diagram between UO_2 and oxygen–saturated α-Zr(O) 76

26. Size dependence of bubble velocities in liquid UO_2 in a temperature gradient of 100 K/cm at 2200 K 77

27. Size dependence of bubble velocities in liquid UO_2 in a temperature gradient of 5000 K/cm at 3135 K 79

28. FASTGRASS–VFP predictions of fission–gas and Cs release during ORNL Test HI–1, compared with measured values 86

29. FASTGRASS–VFP predictions of fission–gas and Cs release during ORNL Test HI–3, compared with measured values 87

30. FASTGRASS–VFP predictions of fission–gas and Cs release during ORNL Test HI–2, compared with measured values 88

31. FASTGRASS predictions of fission–gas release during ORNL Test HI–3 with and without the effects of fuel liquefaction..... 90

32. FASTGRASS predictions of grain growth during ORNL Test HI–3 with and without the effects of fuel liquefaction..... 90

33. FASTGRASS predictions of fission–gas release during ORNL Test HI–4 with and without the effects of fuel liquefaction..... 91

34. FASTGRASS–VFP predictions of fission–gas release rates during the SFD–ST experiment..... 92

35. FASTGRASS–VFP predictions of fission gas retained intragranularly at the hottest fuel region during the SFD–ST experiment..... 94

36. FASTGRASS–VFP predictions of grain growth in the hottest fuel region during the SFD–ST experiment..... 94

37. FASTGRASS-calculated fission-gas release rates for SFD 1–1 with and without the effects of liquefaction/dissolution..... 97

38. FASTGRASS-calculated percent noble-gas release for SFD 1–1 with and without the effects of fuel liquefaction/dissolution..... 98

39. GRASS–SST– and FASTGRASS–calculated bubble size distribution in liquefied fuel just subsequent to fuel dissolution for SFD 1–1 and SFD 1–4..... 99

40. FASTGRASS-calculated fission-gas release during fuel heatups to 1800–2800 K and during subsequent hold periods..... 104

41. FASTGRASS-calculated Cs release during fuel heatups to 1800–2800 K and during subsequent hold periods..... 104

42. FASTGRASS-calculated Ba release during fuel heatups to 2200–2800 K and during subsequent hold periods..... 105

43. Predictions of transient gas release vs. experimentally measured values from the ORNL HBU, HT, and HI tests..... 106

44. FASTGRASS-calculated release rates from solid fuel obtained from the fractional release curves shown in Fig. 40..... 107

List of Tables

1. Ranking of Radionuclides with Respect to Health Effects 4
2. Definition of Variables in Eq. 1 7
3. Values of Key Materials Properties Used in Eqs. 16, 20, and 47–50, which Define Model X 33
4. Values of Key Materials Properties Used in Eqs. 51–59, which Define Model Y 37
5. Regression Equations Developed for Figs. 3 and 4, with Pertinent Statistical Information 44
6. Model Predictions for As–Irradiated Fuel Compared with Experimental Estimates 46
7. Free Energy of Formation of Ba and Sr Fission Product Oxides 70
8. Values of Various Parameters Used in FASTGRASS 80
9. Xe, Ba, and Sr Release Data of Parker and Barton, Ref. 42, Compared with FASTGRASS Predictions 83
10. Predicted Intragranular Migration of Xe and Ba in 4000–MWd/t Fuel Fragments during the Parker and Barton Tests 84
11. Predicted Chemical Form of Retained Ba 85
12. FASTGRASS–VFP Predictions of Fission–Product Release during the SFD–ST Test, Compared with Measured Values 95
13. Percentage Fission–Product Release Measured during Two PBF–SFD Tests, Compared with FASTGRASS Predictions 96
14. FASTGRASS–Calculated I, Cs, and Xe Morphology for Test SFD 1–1 101
15. FASTGRASS–Calculated Ba and Sr Morphology for Test SFD 1–1 102

B1. Possible Roots of the Quartic Equation 138

B2. Roots of the Quartic Equation 139

B3. Numerical Values of SL_j, BI_j, and DI_j Obtained from Harrison's Equation of State 139

C1. Summary of Gas Release Data Obtained by Small, Ref. 35, with the Sweep Gas Technique 140

C2. Summary of Gas Release Data Measured by Burbach and Zimmerman, Ref. 36 140

C3. Summary of Gas Release Data Obtained by Killeen and Baker, Ref. 37 141

C4. Summary of Gas Release Data Obtained by Bridge, Cordall, and Young, Ref. 38 141

C5. Summary of Series-1 Annealing Experiments of Small, Ref. 39 142

C6. Summary of Gas Release Data Obtained by Zimmermann, Ref. 40 142

C7. Summary of Data from Fission-Product Release Tests Conducted on Commercial LWR Fuel by Collins, Osborne, Lorenz, and Malinauskas, Ref. 41 143

C8. Summary of Gas Release Data Obtained by Parker and Barton, Ref. 42, for UO_2 Heated 5.5 h in Pure Helium 144

Nomenclature

A	C_aD_a
A_F	projected areal coverage of grain-face bubbles
A_f	maximum areal coverage of grain-face bubbles
A_{gb}	area of a portion of grain boundary
AT	constant in Harrison's extrapolated equation of state
A_v	Avogadro's number
A_x	function of T_r
a_o	lattice constant
area	cross–sectional area of node boundary
B	Van der Waals constant
B_v	D_u
B_{vcrit}	Critical value of grain edge swelling required for long-range tunnel interlinkage
B_{vedge}	average value of grain edge swelling
B_{vpor}	contribution of edge swelling from as-fabricated porosity
B_x	1 or a function of T_r term in G(t)
b	irradiation–induced re–solution rate
b_o	measurable constant in equation for irradiation–induced re-solution rate
C_b, C_f, C_e	concentration of bubbles
$\overline{C}_g$	average concentration within grains
C_1^g, C_2^g, C_3^g	concentrations at ρ_1, ρ_2, and ρ_3
C_g	concentration of gas in solid

C_g^o	gas solubility
C_v	vacancy concentration
D_b	diffusion coefficient of gas bubble of radius R
D_g	diffusion coefficient of gas in solid
D_{gb}	grain boundary diffusion coefficient
DI	molar volume
DLM	constant in Harrison's extrapolated equation of state
D_o	preexponential factor for surface diffusion
D_u	uranium diffusivity
D_v	species diffusivity in the vapor phase
dc	0.0265 moles/cm^3
$d_g/2$	grain radius of a gas bubble
$\frac{dh}{dt}$	rate of gas precipitation into bubbles
d_i	gas density
$(dN/dt)_n$	gas bubble nucleation rate
d_r	reduced density, d_i/d_c
E_s	activation energy for surface diffusion
e	grain–boundary–sweeping efficiency
FAWGE	average number of grain faces per grain
F_b, F_f, F_e	force exerted by a bubble on the boundary
F_{gb}	adhesive force
F_i's	terms in the diffusive–flow calculation
F_n	nucleation factor

$f_f(\theta)$	geometrical factor that accounts for the lenticular shape of grain face bubbles
$f(T)$	$\Sigma\beta^n q_n n^n$
$G(t)$	term in precipitation-hindering equation
g	gas released
g_s	strain energy
H	$\left(B_v^2 + 4AB_v\right)^{1/2}$
h	concentration of gas in bubbles
J	flux of gas atoms to or across boundary
J_g	gas flux into bubbles
J_v	vacancy flux into bubbles
K	fission rate
K_e	= 1 if edge bubbles larger than critical size required for detachment; otherwise = 0
K_f	= 1 if face bubbles larger than critical size required for detachment; otherwise = 0
kT	thermal energy
L	geometrical factor related to the fraction of the grain boundary area occupied by pores
M	moles of gas
m_1, m_2	masses of species diffusing in vapor
N_b, N_f, N_e, N	average number of gas atoms in a bubble
n	moles of gas precipitated in bubble
P_A	grain face channel interlinkage fraction
P_h	external hydrostatic pressure

P_I	grain edge tunnel interlinkage fraciton
P_i, P	internal gas pressure
P_o	preexponential factor in the expression for equilibrium vapor pressure
P_{O_2}	oxygen partial pressure
Q	activation energy for grain boundary motion
Q_v	volume diffusion heat of transport
q_1-q_{12}	coefficients in the diffusive–flow calculation
q_n	constants given by Ronchi
R_b, R_f, R_e, R	average radius of the bubbles
R_g	radius of a gas atom
R_g	gas constant
R_J	average jump distance of an atom diffusing by surface diffusion
r	radius of spherical volume of gas
r_c	radius of curvature
$2r_{gb}$	characteristic distance of bubble spacing
$S_v^{\alpha\alpha}$	grain boundary area per unit volume
T_c	289.8 K
T_r	reduced temp., T/T_c
t	time
V	volume of pore
V_b	velocity of gas bubble in a temperature gradient
V_f, V_e	velocity of grain face and grain edge bubbles

V_g	velocity of gas atom in a temperature gradient
V_{gb}	velocity of grain boundary
v	effective volume of gas
v_o	$\frac{2\pi}{3} A_V \sigma L^3$
vol	volume of node
w	boundary thickness
X_i's	terms in the diffusive-flow calculation
x	distance from center of bubble
x_o	radius of spherical volume
y_i	$vd_i/2$
Z_i^{hs}	$\frac{1+y_i-y_i^2-y_i^3}{(1-y_i)^3}$
β	$1/T$
δ	re-solution efficiency on grain boundaries
$\varepsilon(R)$	increase in strain energy due to precipitation of one gas atom in bubble
ε_L	constant in Lennard-Jones potential
$< \varepsilon R >$	average of εR between 0 and t
ϕ, ϕ_f, ϕ_e	angle of contact between bubble and boundary
γ	surface energy
γ_{gb}	grain boundary surface tension
κ	number of atoms produced per fission
λ	average distance traveled by an atom ejected from a bubble
μ	elastic modulus

$\mu(r)$	Lennard-Jones potential
ν	vibration frequency of an atom
μ_L	viscosity of liquefied fuel
$\pi\sigma^2$	collision cross section between diffusing species and the principal component in the gas phase
ΔE	energy difference
Δg	interaction energy
Δt	time increment
ΔH_v	heat of vaporization
∇T	temperature gradient
ΔZ_i	correction term
ρ	radius of curvature
ρ_e	radius ratios or density of liquid fuel mixture
ρ_g	gas density in bubble
σ	stress field around bubble
σ_e	width of distribution of grain edge porosity interlinkage probability
σ_L	constant in Lennard-Jones potential
σ_f	width of grain face channel interlinkage probability distribution
τ	relaxation time
Ω	lattice molecular volume

FASTGRASS: A Mechanistic Model for the Prediction of Xe, I, Cs, Te, Ba, and Sr Release from Nuclear Fuel under Normal and Severe-Accident Conditions

User's Guide for Mainframe, Workstation, and Personal Computer Applications

by

J. Rest and S. A. Zawadzki

Executive Summary

This report describes the primary physical/chemical models that form the basis of the FASTGRASS mechanistic computer model for calculating fission product release from nuclear fuel. In addition, it compares calculated results with test data. Input instructions for execution on mainframe and personal computers are provided, as is a description of FASTGRASS output. The theory of noble-gas behavior and its effect on the release of I, Cs, Te, Ba, and Sr is discussed. The behavior of these fission products in the presence of grain-growth phenomena and fuel liquefaction/dissolution and oxidation is presented, as is the chemistry of the Sr, Ba, I, and Cs in the fuel system.

Validation of mechanistic models for gas release and swelling is complicated by data containing large systematic errors, phenomena characterized by synergistic effects, and uncertainties in material properties. Statistical regression analysis is recommended for the selection of a reasonably well-characterized data base for gas release from irradiated fuel under normal and transient heating conditions. It is demonstrated that an appropriate data selection method is required to realistically examine the impact of differing descriptions of the phenomena, and uncertainties in selected materials properties, on the validation results. Comparison of FASTGRASS predictions with test data indicates two major trends: (1) fission-product release behavior from solid fuel depends strongly on fuel microstructure and irradiation history, as well as on fuel temperature, transient scenario, and internal fuel-rod chemistry; and (2) fuel liquefaction/dissolution, fracturing, and oxidation also exert a pronounced effect on release during fuel-rod degradation.

The FASTGRASS mechanistic approach to the prediction of fission-product release during normal irradiation, postirradiation annealing, and severe core–damage accident conditions compares well with release trends noted from in– and out–of–reactor experiments. The FASTGRASS predictions agree much better with the data over a wide range of temperature, fuel burnup, and fuel-damage conditions than the conventional temperature–only, semiempirical correlations.

1 Introduction

Both the Three Mile Island (TMI)-2 and Chernobyl accidents have increased public awareness of the potential for large-scale fission-product release during severe core-damage accidents. Both events resulted in significant release of noble gases (Xe, Kr), and volatile (I, Te, Cs) and alkaline earth (Sr, and Ba) radionuclides from the fuel itself. Differences in primary coolant and design of containment buildings largely determined the ultimate release characteristics of the plants. However, a detailed analysis of fission-product release for severe accidents requires adequate time-dependent prediction of the release of volatile and alkaline-earth fission products, (VFPs) and (AEFPs), respectively, from fuel, and subsequent analysis of the transport behavior of the fission products from the degraded core, primary system, and containment. The first step in this analysis is the prediction of VFP and AEFP release from severely damaged fuel. This paper describes the primary physical/chemical models that form the basis of the Fast Gas Release and Swelling Subroutine (FASTGRASS) mechanistic code for the estimation of the release of six fission products, including those with the most serious effects on human health. In terms of the health consequences, as indicated in Table 1, I, Te, and Cs are the primary risk-dominant radionuclides associated with the release of fission products during severe core accidents.[1] The next most important fission products with respect to public health are Sr, Ru, and Ba. Based on an assessment of long- versus short-lived fission products,[2] FASTGRASS does not directly include the effects of radioactive decay. However, this effect can be indirectly modeled in FASTGRASS by using effective generation rates (obtained, for example, from the ORIGEN code).[3]

In recent years, considerable progress has been made in identifying gas-release mechanisms in UO_2-base fuels during steady-state conditions.[4] This progress has been made through both experimental and theoretical work and has been tested and utilized in the development and application of computer codes. The delineation of fission-gas behavior during off-normal or transient conditions, and a predictive capability for this phenomenon is much less advanced. An understanding of and the capability to predict the behavior of fission gases in nuclear fuel during off-normal conditions are essential to any rational estimate of fuel-element integrity, fission-product source, and the associated safety issues.

Table 1. Ranking of Radionuclides with Respect to Health Effects

Element	Rank	Ranking Factor[a]
Iodine, I	1	38
Tellurium, Te	2	37
Cesium, Cs	3	31
Strontium, Sr	(4)[b]	16
Ruthenium, Ru	(4)	16
Barium, Ba	6	11
Yttrium, Y	7	6
Cerium, Ce	(8)	5
Antimony, Sb	(8)	5
Plutonium, Pu	(10)	4
Curium, Cm	(10)	4
Molybdenum, Mo	(12)	3
Lanthanum, La	(12)	3

[a]Ranking factor is based upon amount of species released and health consequences.
[b]Parentheses denote equivalence in rank.

In general, most of the theoretical and computer code development on fission-gas behavior has separately addressed either the steady-state regime (e.g., Ref. 5) or the transient regime (e.g., Ref. 6). Relatively little effort has been directed toward developing a consistent, comprehensive picture of the full range of possible reactor operating conditions. Indeed, some authors have indicated that understanding the steady-state regime is sufficient to predict the transient regime (e.g., see last paragraph of Ref. 2). That this is *not so* has been demonstrated extensively in the literature.[7-14]

FASTGRASS is a mechanistic computer code for predicting fission-product behavior in UO_2-base fuels during steady-state and transient conditions. This code represents an attempt to develop a predictive capability for the full range of possible reactor operating conditions, and acknowledges an intimate relationship between the pretransient history and the accident scenario. FASTGRASS was originally developed to satisfy the need for a fast-running alternative to the Steady-State and Transient-Gas

Release and Swelling Subroutine (GRASS–SST).[15] Both GRASS–SST and FASTGRASS have been developed under U.S. Nuclear Regulatory Commission sponsorship. (GRASS–SST development was initiated in 1974, and FASTGRASS, in 1978.) Subsequently, additional fission products (Cs, I, Ba, Sr, and Te) were added to the FASTGRASS calculation. The most important differences between FASTGRASS gas-behavior models and GRASS–SST are in the algorithms used for calculating the densities of bubbles in each of a number of bubble size classes. Each bubble size class is characterized by an average number of atoms per bubble, the value of which differs from that of the preceding size class by a constant multiplier. The number of size classes is a variable that is determined dynamically during a computer run. Changes in the bubble size distribution, caused by bubble coalescence and irradiation-induced re–solution, for example, are determined by solving a large number of integral/differential equations for each time-step. Solutions are carried out for bubbles on grain surfaces (faces and edges), along dislocations, and in the bulk matrix. An iterative solution of a large number of coupled equations is a major contributor to the computer running times of GRASS–SST.

In contrast to the multiclass description of the bubble size distribution in GRASS–SST, FASTGRASS calculates the evolution of the average size bubble (e.g., corresponding to the peak in a GRASS–SST-calculated distribution). A typical calculation of one-node gas release with FASTGRASS entails the simultaneous solution of five equations: intragranular gas atom and bubble density, bubble densities on the grain faces and edges, and gas release due to long–range porosity interconnection along the grain edges. Single gas atoms are characterized by their number density and atomic radius, whereas gas bubbles are characterized by number density and average size, expressed as the average number of atoms per bubble. The equilibrium radii of the bubbles are determined with a modified hard-sphere equation of state, and the nonequilibrium radii are determined on the basis of vacancy kinetics and interactions between reactive fission products (e.g., I, Cs, Ba, and Sr) and the fuel.

Sections 2 and 3 of this report present an overview of the modeling of noble-gas release from solid fuel. The release of noble gases plays a major role in establishing a route for fission-product migration from the interior of the solid fuel matrix to the exterior or escape surface. In Section 4, the models are compared with postirradiation annealing data. Section 5 describes the chemical interactions between reactive fission products (e.g.,

I, Cs, Ba, and Sr) and the fuel. Section 6 describes phenomena affecting fission-product release under severe accident conditions, where fuel-oxidation-induced grain growth, molten-zircaloy-cladding-induced fuel dissolution/liquefaction, and quench-induced fuel shattering occur. In Section 7 the theory is compared with data. Section 8 compares fission-product release from conventionally irradiated fuel during out-of-reactor high-temperature heating tests in a flowing-steam atmosphere, as determined by an NRC empirical model and FASTGRASS. Sections 9 and 10 describe FASTGRASS input and output, respectively. FASTGRASS configuration has been designed to provide flexibility in altering model options (e.g., invoking or not invoking microcracking, grain growth, etc., model options for gas precipitation in solids, etc.) and materials properties. For example, FASTGRASS has been used to analyze the behavior of He bubbles in austenitic stainless steels,[16] Kr implanted into Ni,[17] as well as the behavior of fission gas in uranium silicide (U_3Si, U_3Si_2) aluminum dispersion fuels.[18] Finally, Section 11 presents remarks and conclusions.

2 FASTGRASS Theory of Fission-Gas Behavior in Solid Fuel

The FASTGRASS code mechanistically predicts atomic and bubble behavior of fission gas in UO_2 fuel under steady-state and transient conditions. Models are included that assess the effects of fission-product generation, atomic migration, bubble nucleation and re-solution, bubble migration and coalescence, and channel formation on grain faces, of interlinking on grain edges, and microcracking on both the amount of released fission products and on their distribution within the fuel. FASTGRASS solves a set of coupled nonlinear differential equations for the intra and intergranular concentrations of fission-product atoms and gas bubbles of the form

$$\frac{dC_i}{dt} = -a_i C_i^2 - b_i C_i + e_i. \qquad (1)$$

The variables in Eq. 1 are defined in Table 2. The basic equations solved in FASTGRASS are described below. In these basic equations, C_g, C_b, C_f, and C_e are the concentrations of intragranular gas atoms, gas bubbles, grain face bubbles, and grain edge bubbles, respectively, and N_b, N_f, and N_e are the corresponding number of gas atoms per bubble.

Table 2. Definition of Variables in Eq. 1, $dC_i / dt = -a_i C_i^2 - b_i C_i + e_i$

C_i	$a_i C_i^2$	$b_i C_i$	e_i
Concentration of intra-granular gas atoms, VFPs, and AEFPs	Rate at which gas atoms are lost due to gas bubble nucleation	Rate at which gas atoms, VFPs, and AEFPs are lost due to radiolytic decay, diffusive flow to the grain boundaries, grain boundary sweeping, diffusion into gas bubbles, chemical reactions, and fuel dissolution	Rate at which atoms, VFPs, and AEFPs are gained due to atom re-solution, fission of uranium nuclei, chemical reactions, and long-range migration
Concentration of intra-granular gas bubbles	Rate at which gas bubbles are lost due to bubble coalescence	Rate at which gas bubbles are lost due to diffusive flow to the grain boundaries, grain boundary sweeping, gas atom re-solution, and fuel dissolution	Rates at which gas bubbles are gained due to bubble nucleation, diffusion of gas atoms into bubbles, and long-range migration
Concentration of grain face gas bubbles, VFPs, and AEFPs	Rate at which gas bubbles are lost due to bubble coalescence	Rate at which gas bubbles, VFPs, and AEFPs are lost due to diffusion to grain edges, formation of grain face, channels, microcracking, chemical reactions, fuel liquefaction/dissolution, and long-range migration	Rate at which gas bubbles, VFPs, and AEFPs are gained due to intragranular migration to grain faces, chemical reactions, and long-range migration
Concentration of grain edge bubbles, VFPs, and AEFPs	Rate at which gas bubbles are lost due to bubble coalescence	Rate at which gas bubbles, VFPs, and AEFPs are lost due to long-range grain edge/bubble interconnection, microcracking, chemical reactions, and fuel liquefaction/dissolution	Rate at which gas bubbles, VFPs, and AEFPs are gained due to migration of grain-face fission products to grain edges, and chemical reactions

2.1 Intragranular Fission Gas

The concentration of gas atoms, C_g, is determined by solving the equation

$$\frac{dC_g}{dt} = -16\pi F_N R_g D_g C_g^2 - 4\pi\left(D_g + D_b\right)\left(R_g + R_b\right)C_g C_b$$

$$-\pi\left|V_b - V_g\right|\left(R_g + R_b\right)^2 C_g C_b - S_v^{\alpha\alpha} V_g C_g + \frac{6D_g}{dg}\frac{\partial C_g}{\partial r}\bigg|_{r = d_g/2}$$

$$-3C_g d_g(t) V_{gb} / d_v^g + \kappa K + bN_b C_b + \delta bN_f C_f + \delta bN_e C_e. \qquad (2)$$

In Eq. 2, R_g, R_b, D_g, D_b, and V_g, V_b are the radii of the intragranular gas atom and gas bubble, diffusion coefficients, and velocities, respectively. F_N is the nucleation factor, i.e., the probability that two gas atoms that have come together actually stick. $S_v^{\alpha\alpha}$ is the grain boundary area per unit volume; d_g, the grain diameter; K, the fission rate (fissions/cc/s); and x, the number of gas atoms produced per fission. The successive terms on the right-hand side (RHS) of Eq. 2 represent, respectively, 1. the loss of gas atoms due to bubble nucleation; 2. and 3. the random and biased capture of gas atoms by bubbles; 4. and 5. biased and random diffusion of gas atoms to grain boundaries; 6. loss of gas atoms due to grain boundary sweeping; 7. gas atom generation due to fission; and 8–10. the gain of gas atoms due to gas atom re–solution from intragranular, grain face, and grain edge bubbles.

The fifth term on the RHS of Eq. 2, the flux of gas atoms diffusing to the grain boundaries in a concentration gradient, is obtained by solving for the concentration of gas atoms, C_g, within a spherical grain satisfying the equation

$$\frac{\partial C_g}{\partial t} = \frac{1}{r^2}\frac{\partial}{\partial r}\left(D_g r^2 \frac{\partial C_g}{\partial r}\right) + \kappa K. \qquad (3a)$$

In general, Eq. 3a is solved with the boundary conditions

$$C_g = 0 \text{ at } t = 0 \text{ for } o \le r \le d_g/2, \tag{3b}$$

$$C_g = 0 \text{ at } r = d_g/2 \text{ for } t_0 \le t \le t_0\ \Delta t, \tag{3c}$$

$$\frac{\partial C_g}{\partial r} = 0 \text{ at } r = 0 \text{ for } t_0 \le t \le t_0 + \Delta t, \tag{3d}$$

where Δt is an increment of time.

The concentration of gas atoms in a spherical grain described in Eq. 3a is

$$\frac{1}{r^2}\frac{d}{dr}\left(D_g r^2 \frac{dc_g}{dr}\right) - \frac{C_g}{\delta t} + \frac{C_g^o}{\delta t} + \kappa K = 0. \tag{4}$$

Euler's theorem may now be used to obtain a variational principle equivalent to Eq. 4:

$$\delta \int_0^{1/2d_g} 4\pi \left[\frac{D_g}{2}\left(\frac{dC_g}{dr}\right)^2 + \frac{C_g^2}{2\delta t} - \left(\frac{C_g^o}{\delta t} + \kappa K\right) C_g\right] r^2 dr = 0, \tag{5a}$$

which assumes that Dirichlet boundary conditions are to be applied. An approximate solution to the problem may now be obtained by choosing a trial function that satisfies the boundary conditions and minimizes the integral in Eq. 5 in terms of free parameters in the function. Many types of trial function could be chosen, but piecewise functions are easier to handle than global functions. Quadratic functions are attractive because they allow an exact representation of Eq. 3a for long times. To meet the objective of a realistic level of accuracy with a minimum of computer storage and running time, the spherical grain is split into two concentric regions of approximately equal volume (Fig. 1). In each region, the gas concentration is represented by a quadratic function constrained to have $dC_g/dr = 0$ at $r = 0$. In the outer Region II (Fig. 1), the concentration function is constrained to a value of $C_g = 0$ at $r = d_g/2$. The two functions are also constrained to be continuous at the common boundary of the two regions. This leaves three

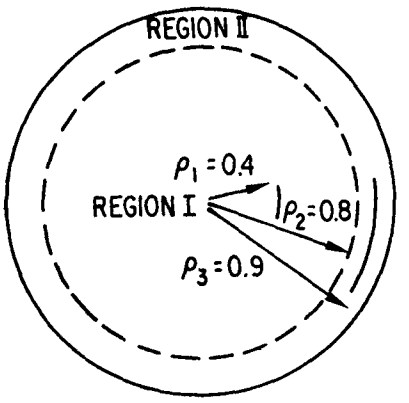

Fig. 1. Configuration of the two-zone model

free parameters. Matthews and Wood[19] chose these to be the concentrations C_1^g, C_2^g, and C_3^g, respectively, for the radius ratios $\rho_1 = 0.4$, $\rho_2 = 0.8$, and $\rho_3 = 0.9$, where $\rho = 2r/d_g$. These positions are the midpoint radius of Region I, the boundary between the regions, and the midpoint radius of Region II, respectively. Thus, the trial functions are as follows:

For Region I,

$$C_g = C_1^g\left(0.64 - \rho^2\right)/0.48 + \left(\rho^2 - 0.16\right)/0.48. \tag{5b}$$

For Region II,

$$C_g = 5C_2^g\left(10\rho^2 - 19\rho + 9\right) + 10C_3^g\left(18\rho - 10\rho^2 - 8\right). \tag{5c}$$

Eqs. 5b and 5c are substituted for C_g in Eq. 5a and an extremum is found by differentiating with respect to C_1^g, C_2^g, and C_3^g in turn. The following three linear equations are thus obtained:

$$\begin{aligned}&\left(q_1 D_g / d_g^2 + q_{2/\delta t}\right)C_1^g + \left(q_3 D_g / d_g^2 + q_{4/\delta t}\right)C_2^g \\ &\quad = K_g q_5 + \left(C_1^0 q_2 + C_2^0 q_4\right)/\delta t,\end{aligned} \tag{5d}$$

$$\left(q_3 D_g / d_g^2 + q_{4/\delta t}\right) C_1^g + \left(q_2 D_g / d_g^2 + q_{7/\delta t}\right) C_2^g + \left(q_8 D_g / d_g^2 + q_{9/\delta t}\right) C_3^g = K_g q_{10} + \left(C_1^0 q_4 + C_2^0 q_7 + C_3^0 q_9\right) / \delta t, \tag{5e}$$

$$\left(q_9 D_g / d_g^2 + q_{9/\delta t}\right) C_2^g + \left(q_{11} D_g / d_g^2 + q_{12/\delta t}\right) C_3^g = K_g q_{13} + \left(C_2^0 q_9 + C_3^0 q_{12}\right) / \delta t, \tag{5f}$$

where C_1^0, C_2^0, and C_3^0 are the values of the concentrations at the evaluation points at the start of the time increment. The various q coefficients are integrals, which, when directly evaluated, are, to four figures,

$q_1 = 4.552,$	$q_2 = 0.06935,$	$q_3 = -4.552,$
$q_4 = 0.02167,$	$q_5 = 0.09102,$	$q_6 = 37.78,$
$q_7 = 0.07615,$	$q_8 = -38.72,$	$q_9 = 0.008456,$
$q_{10} = 0.01008,$	$q_{11} = 87.04,$	$q_{12} = 0.08656,$
$q_{13} = 0.1083.$		

Equations (5d)–(5f) can be directly solved to obtain the concentrations C_1, C_2, and C_3 as follows:

$$C_1^g = \frac{X_1 - F_2 C_2^g}{F_1},$$

$$C_2^g = \frac{\frac{F_2}{F_1} X_1 + \frac{F_s}{F_7} X_3 - X_2}{\frac{F_2}{F_1} F_2 + \frac{F_s}{F_7} F_s - F_4}, \tag{5g}$$

and

$$C_3^g = \left(X_3 - F_5 C_2^g\right) / F_7, \tag{5h}$$

where

$$F_1 = q_1 D_g / d_g^2 + q_2 / \delta t, \quad F_2 = q_3 D_g / d_g^2 + q_4 / \delta t,$$

$$X_1 = K_g q_s + (C_1 q_2 + C_2 q_4) / \delta t,$$

$$F_4 = q6 D_g / d_g^2 + q_7 / \delta t, \quad F_5 = q8 D_g / d_g^2 + q_9 / \delta t,$$

$$X_2 = K_g q_{10} + \left(C_1 q_4^0 + C_2^0 q_7 + C_3^0 q_9\right) / \delta t,$$

$$F_7 = q_{11} D_g / d_g^2 + q_{12} / \delta t, \text{ and}$$

$$X3 = K_g q_{13} + \left(C_2^0 q_9 + C_3^0 q_{12}\right) / \delta t.$$

The flux of gas atoms to the boundary (in units of atoms/cm^3/s) is given by

$$J = -\frac{6D_g}{dg} \frac{\partial C}{\partial r}\bigg|_{r=d_g/2}. \tag{5i}$$

$$J = -\frac{D_g}{d_g^2}\left(-60C_2^g + 240C_3^g\right). \tag{5j}$$

For proper coupling of the diffusive flow process to other processes that affect fission-gas behavior, (e.g., gas atom re-solution, gas atom trapping by bubbles, and gas bubble nucleation and coalescence) information is required on the average concentration of fission gas within the grain.

Matthews and Woods[19] determined that the best expression for the average concentration within the grains, $\overline{C}_g$. is given by

$$\overline{C}_g = 0.2876C_1^g + 0.2176C_2^g + 0.4261C_3^g. \tag{5k}$$

At the end of an iteration, the concentrations C_1, C_2, and C_3 in Eq. 5k are scaled by imposing the condition that the average concentration calculated by use of Eq. 5k is equal to the average concentration calculated by use of Eq. 2, i.e., that

$$\overline{C}_g = C. \tag{5l}$$

The modified C_1^g, C_2^g, and C_3^g then become the initial values of these concentrations (i.e., C_1^0, C_2^0, and C_3^0) to be used for the next iteration. The diffusive flow of fission-gas bubbles is treated in a manner analogous to that for fission-gas atoms, but with K = 0 in Eq. 3. This method of coupling diffusive flow to other processes that affect fission-gas behavior (e.g., gas atom re-solution, gas atom trapping by gas bubbles, gas nucleation and coalescence) is computationally efficient and has been benchmarked against various analytical solutions.[19]

The last three terms on the RHS of Eq. 2, which account for the effects of fission-induced gas atom re-solution, depend on the rate, b, at which gas atoms are ejected from the bubble. The rate b is calculated under the assumption that gas atom re-solution from a spherical bubble is isotropic and proceeds by the knocking out of single gas atoms. Thus,

$$b = \frac{3b_0 K}{R^3}\int_{R-\lambda}^{R}\left(\frac{1+\cos\theta}{2}\right)r^2 dr, \tag{6a}$$

where $\cos\theta = (R^2 - \lambda^2 - r^2)/2r\lambda$. A straightforward integration of Eq. 6a results in

$$b = \frac{3b_0 \dot{f}}{R^3}(F_2 - F_1), \tag{6b}$$

where

$$F_2 = R^2\left[\frac{R}{6} + \frac{R^2}{16\lambda} + \frac{1}{8}\left(\lambda - \frac{R}{\lambda}\right)\right], \tag{6c}$$

$$F_1 = (R-\lambda)^2\left[\frac{R-\lambda}{6} + \frac{(R-\lambda)^2}{16\lambda} + \frac{1}{8}\left(\lambda - \frac{R}{\lambda}\right)\right], \tag{6d}$$

where λ is the average distance an ejected atom travels, b_0 is a measurable property of the material, and δ is a measure of the "strength" of gas atom re-solution from grain boundary bubbles.

To solve for C_g with Eq. 2, a number of terms on the RHS must be determined. RHS Terms 2, 3, 6, and 8 depend on C_b. The equation for C_b, the concentration of intragranular bubbles, is given by

$$\frac{dC_b}{dt} = 16\pi F_N R_g D_g C_g^2 / N_b + 4\pi\left(D_g + D_b\right)\left(R_g + R_b\right) C_g C_b / N_b$$

$$+\pi\left|V_b - V_g\right|\left(R_g + R_b\right)^2 C_g C_b / N_b - S_v^{aa} V_b C_b + \frac{6D_b}{d_g}\frac{\partial C_b}{\partial r}\bigg|_{r=d_g/2}$$

$$-\frac{3\,C_b}{d_g} V_{gb} - bC_b + \frac{3V_{gb}}{d_g} N_b\left(\frac{K_f}{N_f} C_f + \frac{K_e}{N_e} C_e\right). \tag{7}$$

The interpretations of the first six terms on the RHS of Eq. 7 are analogous to those given for Eq. 2. The last term accounts for the introduction of grain face and grain edge bubbles into the lattice due to bubble pulloff (if the bubbles are bigger than a given critical size K_f and/or K_e = 1; otherwise they are equal to zero) from a moving grain boundary, and/or the presence of large temperature gradients.

2.2 Intergranular Fission Gas: Grain Faces

Six basic quantities must still be determined before Eqs. 2 and 7 can be solved: N_b, N_f, N_e, C_f, C_e, and V_{gb}, the velocity of a moving grain boundary. The equation for C_f, the concentration of gas bubbles on the grain faces (assuming that the grains have an approximate tetrakeidecahedral structure) is given by

$$\frac{dC_f}{dt} = -\delta b C_f - \frac{3V_{gb}}{d_g} K_f C_f - V_f(\text{area} / \text{vol}) C_f - V_f\,\text{FAWGE} / d_g C_f - P_A C_f / t$$

$$+S_v^{\alpha\alpha}\left(V_g C_g / N_f + V_b C_b N_b / N_f\right) - \frac{6}{d_g}\left[\frac{D_g}{N_f}\frac{\partial C_g}{\partial r}\bigg|_{r=d_g/2} + \frac{D_b N_b}{N_f}\frac{\partial C_b}{\partial r}\bigg|_{r=d_g/2}\right]$$

$$+3d(t) V_{gb}\left(C_g / N_f + C_b N_b / N_f\right) / d_g. \tag{8}$$

The first and second terms on the RHS of Eq. 8 are loss terms due to bubble destruction by gas atom re-solution, and bubble pulloff, respectively. The third term on the RHS of Eq. 8 is the loss of grain face bubbles due to biased migration out of the node (area = cross-sectional area of node boundary, and vol = volume of node; in general, for solid fuel, a node has the shape of a cylindrical annulus). The fourth and fifth terms represent the biased grain

face bubble migration, and migration of grain face gas through grain face channels to the grain edges. FAWGE is the average number of grain faces per grain.

FASTGRASS calculates grain face saturation by fission gas by directly addressing the calculated distribution of fission-gas bubble sizes. The projected areal coverage of the grain face by these bubbles, per unit volume, is given by

$$A_F = \pi R_f^2 C_f f_f(\theta), \tag{9}$$

where $f_f(\theta)$ is a geometrical factor that accounts for the lenticular shape of the grain face bubbles. If the gas is assumed to be made up of equal, closely packed, touching bubbles, the maximum areal coverage per unit area of grain face is $A_F^* = 0.907$. (Under conditions where this assumption is not valid, $A_F^*{}^* < 0.907$, the FASTGRASS code utilizes a nominal value of $A_F^* = 0.50$). Grain face saturation (i.e., the initiation of gas channel formation) occurs when

$$A_F \geq A_F^* S_V^{\alpha\alpha} \tag{10}$$

where $S_V^{\alpha\alpha}$ is the grain face area per unit volume

Equations 9 and 10 do not account for local variations in fuel microstructure. To include these effects in the calculation of grain face channel formation, it is assumed that the local variations in fuel microstructure can be represented by the width, σ_f, of a distribution of A, Eq. 9, such that the fraction of grain face channel interlinkage is given by

$$P_A = \frac{1}{\sigma_f \sqrt{2\pi}} \int_{x=A_F^* S_V^{\alpha\alpha}} \exp\left[(-x-A)^2 / 2\sigma_f^2\right] dx. \tag{11}$$

The width of the distribution in Eq. 11 is a function of erratic structural parameters, depending on local fuel condition and heterogeneity; in principle, it can be determined experimentally.

2.3 Intergranular Fission Gas: Grain Edges

The equation for C_e, the grain edge bubble concentration, is given by

$$\frac{dC_e}{dt} = -\delta b C_e - \frac{3V_{gb}K_eC_e}{d_g} + V_f \frac{FAWGE}{d_g}\frac{Ne}{N_f}(1-P_I)C_f$$

$$+P_A \frac{N_e}{N_f}(1-P_I)C_f / t - \frac{dP_I}{dt}C_e. \qquad (12)$$

In Eq. 12, the last term on the RHS represents the loss of gas due to release through long-range interconnection of grain edge porosity to a free surface. The FASTGRASS model for calculating the probability of long-range grain edge tunnel interconnection is based on the assumption that the long-range interconnection is a function of the swelling of grain edge bubbles. This assumption is supported by experiment[8] as well as theory.[9] To account for local fluctuations in fuel microstructure and gas bubble morphology, the grain edge/porosity interlinkage fraction, P_I, is assumed to be a statistical distribution around an average value of the grain edge swelling, B_{vedge}:

$$P_I = \frac{1}{\sigma_e\sqrt{2\pi}}\int_{x=B_{vcrit}}^{\infty} \exp\left[-\left(x - B_{vedge} - B_{vpor}\right)^2 / 2\sigma_e^2\right]dx, \qquad (13)$$

where $B_{vedge} = 4/3\pi R_e^3\sigma_e C_e$, and σ_e is a geometrical factor that accounts for the ellipsoidal shape of grain edge bubbles. $B_{vcrit} = 0.05$ is the value of the grain edge swelling at which long-range interconnection would take place if the fuel microstructure and gas bubble morphology were homogeneous; $B_{vpor} = 0.0$ for $\rho \geq 92\%$ of theoretical density. In the absence of microcracking, the fission gas that would have been vented via the crack remains on the grain boundaries. (FASTGRASS contains a model for intergranular microcracking due to overpressurized fission-gas bubbles. This model has been discussed in a previous paper,[8] and is summarized in Appendix A. The effects of microcracking on interlinkage are included by redefining P_I as P_I = maximum (P_I, M_C), where M_C is the fraction of the grain boundary area/volume which has opened up due to microcracking. Retained grain edge fission gas causes the deformation of the grain edges (i.e., grain edge fission-gas-bubble swelling), and the subsequent increased long-range interconnections of grain edge tunnels. This interconnection of grain edge tunnels provides the pathways for enhanced fission-gas release.

The FASTGRASS intergranular swelling model has been benchmarked against experimental results.[13]

2.4 Calculation of Average Number of Gas Atoms per Bubble N_b, N_f, and N_e

Equations 2, 7, 8, and 12 express mass balance and are solved by assuming that the average number of atoms per bubble does not change over the integration time-step, i.e., $\dot{N}_b = \dot{N}_f = \dot{N}_e = 0$. Subsequent to the calculation of the C_i's, changes in N_i are calculated by examining the bubble growth and shrinkage fluxes that influence the average size bubble. For example, changes in N_b are calculated by evaluating

$$\dot{N}_b \;\alpha\; \frac{1}{C_b}\Bigg[16\pi R_b D_b C_b^2 + \pi R_b^2 \alpha_b V_b C_b^2 + 4\pi\left(D_g + D_b\right)\left(R_g + R_b\right) C_g C_b / N_b$$

$$-bC_b - 16\pi F_N R_g D_g C_g^2 + \frac{3V_{gb}N_b}{d_g}\left(\frac{K_f}{N_f}C_f + \frac{K_e}{N_e}\right)\Bigg]. \qquad (14)$$

In Eq. 14, the first three terms on the RHS correspond to the growth of the average size bubble due to random and biased coalescence of these bubbles with each other, and the growth of these bubbles due to accumulation of gas atoms. The fourth and fifth terms on the RHS of Eq. 14 represent the shrinkage of the average size bubble due to destruction of bubbles by fission-induced gas atom re-solution, and generation of very small bubbles by gas atom nucleation (i.e., the introduction of small bubbles will tend to weight the average-size bubble toward smaller sizes). The last two terms represent the growth of the average-size bubble by introducing into the lattice larger grain face and grain edge bubbles that have become detached from a moving grain boundary. The proportionality sign in Eq. 14 indicates that the changes in Nb are computed with a numerical algorithm that evaluates Eq. 14 and increments or decrements N_b by an amount proportional to this value. When N_b is calculated in this fashion, the results agree very well with the results obtained when the evolution of bubble size distribution is calculated with the GRASS-SST mechanistic model. The equations for N_f and N_e are obtained in a fashion analogous to that of Eq. 14.

2.5 Fission-Gas Release

Contributions to fission-gas release, g, come from the venting of grain face gas into interconnected grain edge tunnels, from the venting of previously trapped grain edge gas through newly interconnected tunnels, and from long–range migration of fission-gas bubbles up the temperature gradient:

$$\frac{dg}{dt} = \left(\frac{V_f FAWGE}{d_g} C_f + P_A C_f / t \right) P_I + C_e \frac{dP_I}{dt} + V_f (\text{area} / \text{vol}) C_f \tag{15}$$

For a multinode calculation, the various gas release contributions from each individual node, given by Eq. 15, are summed up to obtain the total gas released during time t. The total contribution of gas released due to long–range migration of fission-gas bubbles up the temperature gradient depends on the cross–sectional area of the inner or outer mode, depending on the direction of the gradient that bounds a free surface.

2.6 Options for Calculating Bubble Radii

2.6.1 General Formulation

Whereas intragranular bubbles are assumed to be spherical, the intergranular gas bubbles are assumed to be lenticular on the grain faces and ellipsoidal along the grain edges. Grain corner bubbles are grouped with edge bubbles and are assumed to have the same shape.

The diffusional growth of nonequilibrium intragranular bubbles is based on an analysis by Gruber.[20] The rate of change of the bubble radius is given by

$$\frac{dR_b}{dt} = \frac{D_u}{R_b} \left[1 - \exp - \left(P - P_h - \frac{2\gamma}{R_b} \right) \frac{\Omega}{kT} \right], \tag{16}$$

where D_u is the vacancy diffusion coefficient, Ω is the atomic volume, kT is the thermal energy, P is the internal gas pressure, P_h is the external

hydrostatic pressure, and γ is the surface energy. For ease in calculating, Gruber[20] provided an approximation for the relaxation time of the form

$$R_b = R_b^o + \left(R_b^{eq} - R_b^o\right)\left(1 - e^{-t/\tau}\right), \tag{17}$$

where τ is defined by the initial growth rate calculated with Eq. 16. In FASTGRASS, R_b^{eq} is obtained by solving an approximate equation of state simultaneously with the capillarity relation.

The diffusional growth of nonequilibrium intergranular bubbles is taken from Speight and Beere.[21] Accordingly, the rate of volume change of grain boundary pores is given by

$$\frac{dV}{dt} = \frac{2D_{gb}W}{kTL}\left(P - \frac{2\gamma}{\rho} - P_h\right), \tag{18}$$

where V is the volume of the pore, ρ is the radius of curvature of the pore, L is a function of the fraction of the grain boundary area occupied by pores, D_{gb} is the grain boundary diffusion coefficient, and W is the boundary thickness. FASTGRASS provides three choices for the Xe equation of state: Van der Waals, Harrison's extrapolation, and a perturbed hard-sphere model. The perturbed hard-sphere model also provides an equation of state for Kr and Ar.

2.6.2 Van der Waals Equation of State

The Van der Waals equation of state is

$$P(V - BN) = NkT, \tag{19}$$

where B is the Van der Waals constant (8.5×10^{-23} cm^3/atom), and N is the number of gas atoms in the bubble. Equation 19 is solved simultaneously with the capillarity relation

$$P = \frac{2\gamma}{R_b^{eq}} + P_h. \tag{20}$$

The method of solving for R_b^{eq} consists of an interpolation (Regula Falsi, Fig. 2) that is applicable to any equation. Let $\bar{x}$ be the value of x for which chord AB (in Fig. 2) intersects the x-axis.

From similar triangles

$$\frac{\bar{x}-x_1}{-f(x_1)} = \frac{x_1'-\bar{x}}{f(x_1')}. \tag{21}$$

Solving for $\bar{x}$ gives

$$\bar{x} = \frac{x_1 f(x_1') - x_1' f(x_1)}{f(x_1') - f(x_1)}. \tag{22}$$

The value $\bar{x}$ is clearly a better approximation than either x_1 or x_1'.

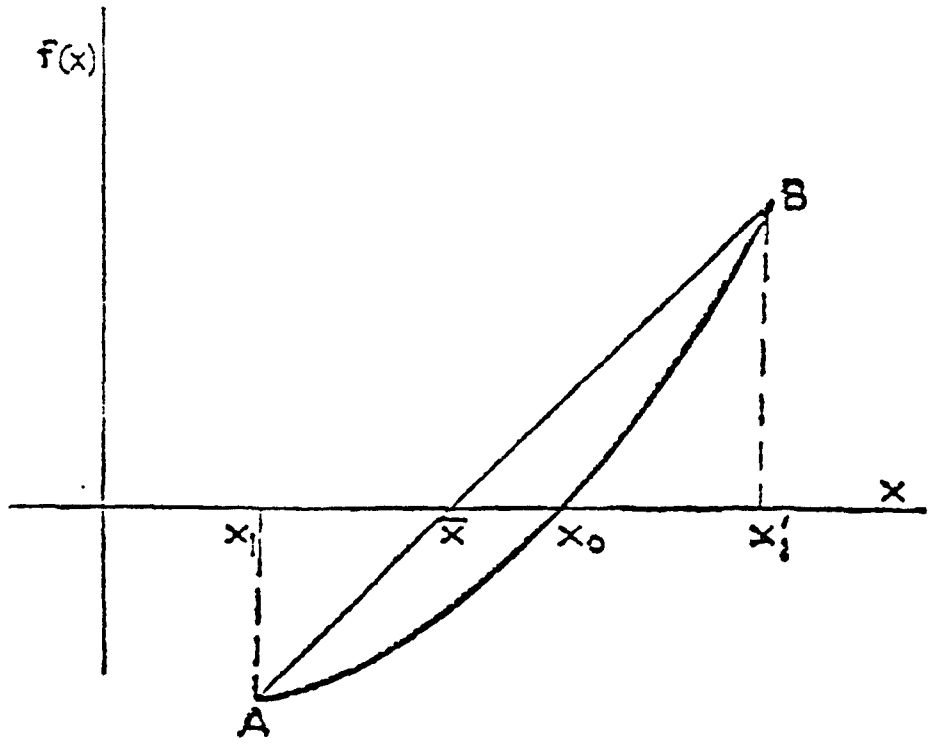

Fig. 2. Method of Regula Falsi

2.6.3 Harrison's Extrapolated Equation of State

FASTGRASS calculates the equilibrium bubble radius (cm) given the number of atoms/bubble, the temperature (K), the surface energy (erg/cm^2), and the hydrostatic stress (dynes/cm^2). The extrapolated equation of state for Xe, based on Harrison's work,[22] is solved simultaneously with the general capillarity equation, Eq. 20.

The equation of state assumed for Xe is

$$P(DI - DLM) = AT, \tag{23}$$

where P is the gas pressure, DI is the inverse of the density, i.e., the molar volume, and DLM and AT are constants to be determined from the tabulated form of the equation of state for Xe published by Harrison.[22] For a bubble of radius R that contains M moles (N atoms) of gas, the molar volume is given by

$$DI = \frac{4}{3}\pi R^3 / M, \tag{24}$$

where $M = N / 6.023\text{x}10^{23}$.

The sign convention for P_h is such that P_h is positive when the fuel is in compression. Equations 23–25 combine to form a quartic equation in R

$$R^4 + \frac{2\gamma}{P_h}R^3 - \frac{3M}{4\pi}\left(DLM + \frac{AT}{P_h}\right)R - \frac{3M}{4\pi P_h}2\gamma DLM = 0, \tag{25}$$

which, in general, has four roots. The solutions to Eq. 25 are given in Appendix B.

2.6.4 Modified Hard-Sphere Equation of State

Based on a perturbed hard–sphere model, Ronchi[23] utilized an equation of state of the form

$$\frac{\frac{4}{3}\pi r^3 P}{RgT} = Z^{hs}(y) - dv_o f(T) - \Delta Z, \tag{26}$$

where r is the radius of the spherical volume of gas, Rg is the gas constant, $Z^{hs}(y) = \left[1 + y - y^2 - y^3\right] / (i - y)^3$ (y = vd/4, where v is the effective gas volume and d is the gas density), ΔZ is a correction term discussed later, v_o is defined in Eq. 28 below, and f(T) is a function that can be calculated for a given interatomic potential and has the form

$$f(T) = \sum_{1}^{\infty} \beta^n q_n^n, \tag{27}$$

where $\beta = 1/T$, and q_n = constants based on those suggested by Ronchi.[14]

The effective volume of the gas, v, is given by

$$v = \frac{2}{3}\pi A_v \sigma_L^3 \left[B^+ + f(T)\right] \equiv v_o \left[B^+ + f(T)\right], \tag{28}$$

where

A_v is Avogadro's number and

$$B^+ = 3/\sigma_L^3 \int_0^{\infty} \left[1 - \exp(u/kT)\right] r^2 dr \cong \frac{1.843\left[1 - 1.078(T_l - 0.162)\right]}{\left[(T_l - 0.553)T_l\right] T_r^{0.25}}, \tag{29}$$

where T_r is the reduced temperature and $T_l = T_r^{5/7}$.

The interatomic potential used in evaluating Eq. 29 is the Lennard–Jones F(12,7) potential,

$$u(r) = \varepsilon_L F(12,7)\left[(\sigma_L / r)^{12} - \left(\sigma_L / r^7\right)\right], \tag{30}$$

where F(12,7) is a constant.

The ΔZ term in Eq. 26 is essentially a correction term that is proportional to the gas density to powers higher than 1 and has been determined by a fit to experimental data:

$$\Delta Z = d_r^2\left[\frac{d_r}{T_r}(7d_r - 1.33/T_r) + A_x\left(1 + d_r^3 B_x\right)\right], \tag{31}$$

where

d_r = reduced density, d_l/d_c (d_c = 0.0265 moles/cm^3),

T_r = reduced temperature, T/T_c (T_c = 289.8 K),

$$A_x = 0.615\left(\frac{1.538}{T_r}\right)^4\left(\frac{1.538}{T_r} - 1\right), \text{ and}$$

$$B_x = \begin{cases} 1 \text{ when } T \le 1000\text{ K}, \\ 50.2\left(\frac{1}{T_r} - 0.25\right)\left(\frac{1}{T_r} - 0.84\right) - 5.4 \text{ when } T > 1000\text{ K}. \end{cases}$$

The hard-sphere equations of state, Eqs. 26–31, are solved simultaneously with the capillarity relation using the Regula Falsi method of interpolation described by Eqs. 21–22.

2.7 Grain Growth/Grain–Boundary Sweeping

FASTGRASS has been applied[9,24] to the interpretation of the release of fission gas, I, Cs, and Te from irradiated high–burnup LWR fuel in a flowing-steam atmosphere during high–temperature, in–cell heating tests performed at Oak Ridge National Laboratory (ORNL)[25] and from trace–irradiated and high-burnup LWR fuel during severe–fuel–damage (SFD) tests performed in the Power Burst Facility (PBF) Reactor in Idaho.[26] The results of these analyses demonstrated that intragranular fission-product behavior during both types of tests can be interpreted in terms of a grain–growth/grain–boundary–sweeping mechanism that enhances the flow of fission products from within the grains to the grain boundaries. Basically, the model assumes that small intragranular bubbles, generally consisting of Xe, Kr, I, Cs, and various fission-product compounds in the vapor phase, and gaseous VFP and A2EFP atoms in the path of a growing grain are swept up by grain boundary adhesive forces. Such grain boundary sweeping provides another mechanism for the collection of fission products at grain faces and edges.

The FASTGRASS theory of grain boundary sweeping of gas bubbles considers the interaction between the moving grain boundary and bubbles in two distinct size classes: those on grain faces and those on grain edges. In addition, FASTGRASS provides a means of determining whether gas bubbles are caught up and moved along by a moving grain boundary or the grain boundary is only temporarily retarded by the bubbles and then breaks away.

Speight and Greenwood[27] proposed a grain growth theory that includes the sweeping of entrapped microbubbles by the front of an advancing grain boundary. The basic postulate of their theory is that small bubbles, because they exert a minimal drag force on an advancing grain surface, are swept along with the moving boundary, whereas large bubbles, because of their higher drag, detach from the advancing surface. To assess the efficiency of bubble sweeping, they compared the magnitude of the force exerted by a bubble on the boundary, i.e.,

$$F_b = \pi R_b \gamma_{gb} \sin 2\phi, \tag{32}$$

with the adhesive effects of the interfacial surface tension, i.e.,

$$F_{gb} = \frac{2\gamma_{gb}}{r_c} \pi r_{gb}^2, \tag{33}$$

where R_b = bubble radius, γ_{gb} = grain boundary surface tension, ϕ= angle of contact between the bubble and the boundary, r_c = radius of curvature of the grain, and $2r_{gb}$ = characteristic distance of bubble spacing.

Whereas Speight and Greenwood[27] considered the effects of the moving boundary interacting with a population of equal-sized bubbles, the theory presented here includes the effects on the moving boundary of two distinct distributions of bubble size, i.e., those on the grain faces and those on the grain edges (the motion of the moving boundary is retarded by the presence of both grain face and grain edge bubbles). In addition, because FASTGRASS provides for a mechanistic calculation of intra- and intergranular fission-product behavior, the coupled calculation between fission-gas behavior and grain growth is kinetically comprehensive. The magnitude of the total force exerted by the bubbles on the boundary, or vice versa, depends on bubble radius and angle of contact according to the relationship

$$F_b = \pi R_b N_f \gamma_{gb} \sin 2\phi_f + \pi R_e N_e \gamma_{gb} \sin 2\phi_e \equiv N_f F_f + N_e F_e, \tag{34}$$

where the subscripts f and e denote grain face and grain edge bubbles, respectively; R_f and R_e are the corresponding bubble radii; N_f and N_e are the corresponding numbers of bubbles; ϕ_f and ϕ_e are the corresponding angles of contact between the bubbles and the boundary; and F_f and F_e represent, respectively, the forces exerted by a grain face and grain edge bubble on the boundary.

The velocity of these bubbles can be determined from the individual forces on the bubbles by utilizing the Nernst–Einstein equation. Assuming that the movement of grain face and grain edge bubbles is controlled by surface diffusion, the velocity of these bubbles can be expressed as

$$V_f = \frac{D_f F_f}{kT} = \frac{3}{4}\frac{a_o^4 D_o}{R_f^3}\frac{2\gamma_{gb}}{kT}\sin 2\phi_f \exp\left(\frac{-E_s}{kT}\right) \tag{35}$$

and

$$V_f = \frac{D_f F_f}{kT} = \frac{3}{4}\frac{a_o^4 D_o}{R_f^3}\frac{2\gamma_{gb}}{kT}\sin 2\phi_e \exp\left(\frac{-E_s}{kT}\right), \tag{36}$$

where V_f and V_e, and D_f and D_e are the velocities and diffusion coefficients of the face and edge bubbles, respectively; k is Boltzmann's constant; T is the absolute temperature; a_o is the lattice constant; D_o is the preexponential factor for surface self–diffusion of the matrix solid; and E_s is the activation energy for this process.

To determine the contact angles ϕ_f and ϕ_e in Eqs. 35 and 36, the velocity of the moving grain boundary must be evaluated. At temperatures of about 1900 K, atomic mobilities in UO_2 result in an enhanced migration of atoms from the convex to the concave side of a curved boundary. The atoms move toward the concave side of the boundary because, in that location, they are surrounded by a somewhat large number of neighboring atoms and thereby exhibit a lower effective energy state. In other words, the net flux of atoms, J, across a curved grain boundary occurs because the binding energy of the atoms in the matrix is somewhat higher on the concave than on the convex side of the boundary. The net result of this atomic motion is shrinkage of small grains with predominantly convex surfaces and growth of larger grains with concave surfaces. The net flux of atoms across the boundary can be expressed as[28]

$$J = \frac{\nu^2}{a_o^2}\frac{\Delta E}{kT}\exp(-Q/kT), \tag{37}$$

where ν is the frequency of vibration of an atom in the solid lattice adjacent to the boundary, ΔE is the difference in energy between two atoms located on opposite sides of the boundary, and Q is the activation energy for grain boundary motion. The velocity of the grain boundary, V_{gb}, is the product of the flux, J, and the atomic volume, which is approximately equal to the cube of the lattice constant,

$$V_{gb} = Ja_o^3 = \nu a_o \frac{\Delta E}{kT}\exp(-Q/kT). \tag{38}$$

The energy difference, ΔE, can be related to the intrinsic properties of the curved grain boundary and to the size and number of gas bubbles attached to the boundary. In the absence of differential strain between adjacent grains, the intrinsic tension force of the grain boundary is the primary force acting on the boundary, and it acts to move the boundary toward the center of curvature of the convex grain. The grain face and grain edge bubbles exert a drag force in the opposite direction. If a section of grain boundary with area A_{gb} moves a distance dx, then

$$\Delta E = \left[\frac{2\gamma_{gb}}{r_c}\left(A_{gb}\right) - F_b\right]dx, \tag{39}$$

where F_b is given by Eq. 34. The first term in the brackets in Eq. 39 represents the adhesive effects of interfacial surface tension, i.e., F_{gb} of Eq. 33. The number of atoms displaced from one side of the boundary to the other is $A_{gb}dx/a_o^3$.

Dividing this expression into the preceding one gives the following equation for the energy change per atom transferred across the boundary:

$$\Delta E = \frac{2a_o^3\gamma_{gb}}{r_c}\left(1 - \frac{\pi R_f N_f r_c \sin 2\phi_f}{2A_{gb}} - \frac{\pi R_e N_e r_c \sin 2\phi_e}{2A_{gb}}\right). \tag{40}$$

Inserting Eq. 40 into Eq. 38 yields the grain boundary velocity, i.e.,

$$V_{gb} = \frac{2a_o^4 v\gamma_{gb}}{r_c kT}\exp(-Q/kT)\left[1 - \tfrac{1}{2}\left(\frac{\pi N_f R_f^2}{A_{gb}}\right)\left(\frac{r_c}{R_f}\right)\sin 2\phi_f\right. \tag{41}$$

$$\left. - \tfrac{1}{2}\left(\frac{\pi N_e R_e^2}{A_{gb}}\right)\left(\frac{r_c}{R_e}\right)\sin 2\phi_e\right]$$

When the bubbles are widely spaced or very small, the second and third terms in the brackets of Eq. 41 are negligible compared to unity, and V_{gb} reduces to the intrinsic velocity of the curved grain boundary. The second and third terms in the brackets in Eq. 41 account for the retarding effects of the bubbles on grain boundary motion.

If both the grain face and grain edge bubbles are swept along with the moving boundary, then

$$V_f = V_e = V_{gb}. \tag{42}$$

The first equality in Eq. 42 yields

$$\frac{\sin 2\phi_f}{R_f^3} = \frac{\sin 2\phi_e}{R_e^3}. \tag{43}$$

From Eqs. 41–43, one obtains

$$\sin 2\phi_e = \left[\frac{3}{4}\frac{D_o r_c}{R_e^3 v}\exp\left(-\frac{E_s - Q}{kT}\right) + \tfrac{1}{2}\left(\frac{\pi N_e R_e^2}{A_{gb}}\right)\left(\frac{r_c}{R_e}\right)\right.$$

$$\left. + \tfrac{1}{2}\left(\frac{\pi N_f R_f^2}{A_{gb}}\right)\left(\frac{r_c}{R_e}\right)\left(\frac{R_f}{R_e}\right)^3\right]^{-1}. \tag{44}$$

Because $\sin 2\phi$ cannot exceed unity, the condition for bubble detachment is met when the RHS of Eq. 44 exceeds unity. If this condition

is satisfied and $R_f = R_e$, both face and edge bubbles become detached from the boundary. If $R_f \neq R_e$, the larger bubble becomes detached (we assume for the sake of this discussion that $R_e > R_f$) and the condition that the smaller bubble be swept along with the moving boundary is examined by requiring that $V_f = V_{gb}$. This results in

$$\sin 2\phi_f = \left[\frac{3}{4}\frac{D_o r_c}{R_f^3 v}\exp\left(-\frac{E_s - Q}{kT}\right) + \frac{1}{2}\left(\frac{\pi N_f R_f^2}{A_{gb}}\right)\left(\frac{r_c}{R_f}\right)\right]^{-1} . \tag{45}$$

If the RHS of Eq. 45 exceeds unity, the smaller bubble (R_f in this case) is also detached from the boundary. If the RHS of Eq. (44) or (45) is less than unity, both face and edge bubbles, or just face bubbles, respectively, are swept along with the moving boundary. The contact angles ϕ_f and ϕ_e can be computed from Eqs. 43–45 and used in Eqs. 35 and 36 or 41 to determine the bubble or grain edge velocity.

As the boundary moves, the rate at which fission products are swept up by the moving boundary is proportional to the rate of change of the volume of the grain, i.e.,

$$\frac{dC_{gb}}{dt} = \frac{3eC_I}{d_g}\frac{d(d_g)}{dt} = \frac{3eC_I V_{gb}}{d_g}, \tag{46}$$

where C_I is the *intra*granular concentration of a fission product, d_g is the grain diameter at time t, and e is a factor that describes the sweeping efficiency of the grain boundary. The value of e is assumed to be unity for the fission gases and atomic I, and 0.6 for atomic Cs. The lower value of e for Cs is consistent with the high chemical affinity of Cs for UO_2, other fission products, and metallic inclusions.

For each fission product, Eq. 41 provides one term in the rate equations for *intra*granular fission products, e.g., Eqs. 2 and 7, and one term in the rate equations for the *inter*granular fission products. The bubble radii, the *intra* and *inter*granular concentrations of the fission products, the grain size, the fraction of the grain boundary area occupied by bubbles ($\pi N_f R_f^2/A_{gb}$ and $\pi N_e R_e^2/A_g$), and the probability of grain edge tunnel interlinkage are some of the key quantities calculated as a function of time.

2.8 Fuel Oxidation Effects

Fuel stoichiometry can have a pronounced effect on atomic mobilities in UO_2 fuel and thus on grain growth kinetics. Data[29] on the diffusivity of ^{133}Xe in $UO_2 + x$ as a function of the fuel stoichiometric condition show that increased levels of O in solution in UO_2 lead to observed increases in the diffusivity of ^{13}Xe and ^{85}Kr. For example, a change from $UO_{2.0}$ to $UO_{2.12}$ can increase the diffusivity of ^{133}Xe by more than two orders of magnitude. Thus, the stoichiometry of the oxide can have a significant impact on atomic mobility and grain growth characteristics. Indeed, in the highly oxidizing environment of fuel exposed to steam flow at elevated temperatures, UO_2 can be expected to become hyperstoichiometric ($0 < x \leq 0.15$) during the course of a severe core–damage accident.[30]

To account for such oxidation effects, two values of the activation energy, Q, are employed in the present version of FASTGRASS. For stoichiometric $UO_{2.00}$ (nominal grain growth), Q = 357 kJ/mole. This value of Q for stoichiometric fuel is close to the value of 360 kJ/M determined by MacEwan and Hayashi.[31] For hyperstoichiometric (oxidized) fuel, the activation energy is decreased to Q = 294 kJ/Mole, approximately proportional to the difference in activation energy between UO_2 and UO_{2+x} reported by Turnbull.[32] This value of Q, for oxidized UO_2, was determined by the requirement that the integrated *intra*granular Xe release as calculated by FASTGRASS be consistent with measured total (end–of–test) release values for SFD–scoping test.[18]

3 FASTGRASS Theory of Fission-Gas Behavior in Solid Fuel: Precipitation-Hindering Option

3.1 Introduction

As discussed in Section 3, conventional theories of gas precipitation in solids are based on the kinetics of gas bubble nucleation and growth (e.g., see Refs. 9, 33, and 34). A gas bubble is nucleated when two or more gas atoms come together in the proximity of one or more vacancies or a vacancy cluster. Subsequently, bubble growth is determined by the relative rates at which atoms are gained (by gas atom diffusion to the bubble and by bubble coalescence) and lost (by irradiation–induced re-solution processes). In all cases, the rate of growth or shrinkage of the bubble to an equilibrium size depends on vacancy concentration and diffusivity.

Conventional theory encounters conceptual difficulty during isothermal annealing of nuclear fuel that has been irradiated at relatively low power. Under these conditions, the as-irradiated material contains a high percentage of gas in solution within the grain matrix.[27–34] Experimentally,[35–42] relatively high rates of gas release from low-power fuel have been observed during and after heatups to relatively low temperatures (1300-2000°C). For "reasonable" choices of certain materials properties (i.e., those affecting gas atom diffusion and bubble nucleation), conventional theory predicts a high rate of trapping of the gas in solution by the existing bubble population and, hence, a low rate of gas release to the grain boundaries and to the fuel surface. The equation for transport of a gas to the grain boundaries in a grain of radius $d_g/2$ in the presence of intragranular precipitation, gas bubble nucleation, and irradiation-induced re-solution can be written as

$$\partial C_g / \partial t = D_g \nabla^2 C_g - dh / dt + bNC_b - (dN / dt)_n + K, \tag{47}$$

where $(dN/dt)_n$ = gas bubble nucleation rate.

The rate of gas precipitation into bubbles, dh/dt, can be expressed as

$$dh / dt = 4\pi\left(R_g + R_b\right)\left(D_g + D_b\right)C_b\left(C_g - C_g^o\right), \tag{48}$$

where C_g^o is the gas solubility.

In solving Eq. 47, it is generally assumed that the grain boundary represents a perfect sink for the gas, i.e., $C_g(d_g/2) = 0$ for $t > 0$, e.g., see Eqs. 3a–3d. The effect of irradiation-induced re-solution, i.e., the term bNC_b in Eq. 2, although not important for postirradiation annealing conditions, plays a significant role in determining fission-gas dynamics during irradiation. In turn, gas response during anneals is dependent on the initial conditions (e.g., bubble size distribution) set by the prior irradiation history.

The fission gases are believed to be highly insoluble within the fuel matrix. Consequently, bubble nucleation is favored and occurs when two or more gas atoms come together in the presence of one or more vacancies or a vacancy cluster. The rate at which gas bubbles are nucleated can be expressed as

$$(dN / dt)_n = 16\pi F_N D_g R_g C_g, \tag{49}$$

where F_N, the nucleation factor, is the probability that two gas atoms that come together actually form a stable nucleus. Once nucleated, the fission-gas bubbles can grow by the accumulation of gas atoms and vacancies and by bubble coalescence, and can shrink by irradiation-induced re-solution:

$$dC_b / dt = -16\pi R_b D_b C_b + (dh / dt) / N + (dN / dt)_n / N - bC_b . \qquad (50)$$

Diffusional growth of nonequilibrium intragranular bubbles is based on vacancy dynamics; bubble equilibration is assumed to occur by volume diffusion of vacancies. The rate of change of the bubble radius is given by Eq. 16, i.e., $dR_b / dt = D_u / R_b \{1 - \exp[-(P - P_h - 2\gamma / R_b)\Omega / kT]\}$.

The equilibrium radius is obtained by using an appropriate equation of state and the generalized capillary relation given by Eq. 20, i.e., $P = 2\gamma / R_b + P_h$.

To address the deficiencies of conventional theory as applied to transient heating conditions, modifications to the conventional theory were proposed by MacInnes and Brearly[43] in a model for the thermal re-solution of fission-gas atoms from gas bubbles. They showed that, with selected materials properties (e.g., gas atom solution energy), the high gas releases observed during transient heating could be due to thermal re-solution from bubbles, together with single-gas-atom diffusion to the grain boundaries. More recently, Ronchi[44] criticized this model and proposed an alternative theory, which considers the precipitation of gas into highly pressurized bubbles and predicts that the elastic strain field produced increases with gas precipitation, and finally leads to a lowering of the precipitation rate. Ronchi[44] showed, in an analogous fashion to the thermal re-solution model, that lowering the gas precipitation rate, combined with single-gas-atom diffusion to the grain boundaries, qualitatively explained the high gas releases observed in postirradiation annealing experiments.

Alternatively, Rest[10] showed that, within the conventional theory, fission gas, I, and Cs release from irradiated high-burnup fuel in a flowing-steam atmosphere during in-cell heating tests to 1700-2000°C, could be interpreted in terms of a grain-growth/grain-boundary sweeping mechanism that enhances the flow of fission-gas and volatile-fission-product atoms from within the grains to the grain boundaries. Fission-product release as a function of time (heat-up and isothermal hold) was predicted accurately by the model, as was the observed grain growth.

However, appreciable grain growth has not been observed in several postirradiation annealing experiments where relatively high rates of gas release were measured.[38,39] In addition, it is difficult to assess the validation results for the thermal re-solution model,[45] because the results strongly depend on the values chosen for certain critical materials properties (e.g., fuel oxygen-to-metal ratio, gas atom solution energy) and on the relative importance of other fission-gas release mechanisms (e.g., bubble coalescence, interlinkage of porosity on grain faces and grain edges). Presumably, Ronchi[44] was unable to provide quantitative validation for his gas precipitation model (separate-effects model) because of a lack of coupling to other key fission-gas behavior models (multiple-effects phenomena).

The purpose of this section is to assess the validation of mechanistic models for gas release and swelling by addressing the complications that generally arise from the use of data characterized by synergistic-effects phenomena and by uncertainties in materials properties. The use of a reasonably well-characterized data base for gas release from irradiated fuel under isothermal annealing conditions allows one to examine the effect of differing descriptions of the phenomena and uncertainties in selected materials properties on the validation results.

3.2 Model X: The Conventional Model

The FASTGRASS gas precipitation model for the conventional theory that will be explored in this report is given by Eqs. 16, 20, and 47-50. In particular, the conventional gas precipitation model (Model X) is given by Eqs. 1-6, with the values of key materials properties listed in Table 3. The first and second terms in the expression for D_g in Table 3 represent thermal[46] and athermal[47] gas atom diffusion, respectively.

A great variety of experimental techniques have been used in attempts to determine the diffusion kinetics of U ions in UO_2 and UO_{2+x}.[48-49] In general, the poor agreement among the many diffusion coefficient measurements has been ascribed, in part, to variations in, or lack of control of the stoichiometry of the samples. Measurements of the preexponential factor in an Arrehnius fit to the data reported in Ref. 40 vary from 4×10^{-7} to ≈ 1 cm^2/s, whereas experimentally deduced activation energies range from 70 to ≈ 105 kcal/mole. The variation in the metal self-diffusion coefficient at 1600°C covers approximately five orders of magnitude for variations in the O-to-metal ratio of 1.98 to 2.10.[49] For purposes of this

Table 3. Values of Key Materials Properties Used in Eqs. 16, 20, and 47–50, which Define Model X

Parameter	Value
D_g (cm^2/s)	$2.1 \times 10^4 \exp(-45820/T + 3.5 \times 10^{-30}K)$
F_n	2.0×10^{-7}
D_u (cm^2/s)	$2.0 \exp(-65000/T)$

study, the activation energy for U self-diffusion in stoichiometric UO_2 is taken from the solution of the mass-action equations for the various defects, together with an expression for the diffusion coefficient of an individual vacancy.[35] For Model X, an upper bound on the preexponential factor[20,50] is utilized to de-emphasize the effects of bubble overpressurization. A larger value of D_u in the Model X calculations results in larger bubbles, i.e., the bubbles approach equilibrium at a faster rate, as described by Eq. 16.

3.3 Model Y: Modified Calculation of Gas Precipitation in Solids

The conventional gas precipitation model, Model X, described above is a phenomenological description of one aspect of fission-gas behavior. Many authors (e.g., Refs. 33, 34, 35, and 9) have relied on this description of gas precipitation in a solid in modeling integral gas release behavior, where a multitude of synergistic mechanisms of behavior are simultaneously operative (e.g., diffusive flow, grain growth, grain face channel formation, grain edge tunnel interlinkage, microcracking). In addition, the multitude of models for integral gas release described in the literature do not incorporate a consistent set of materials properties. The situation is further complicated when one realizes that a consistent data base is not used for model validation. Thus, one is presented with a confusing array of models, validation results, claims, and criticisms.

To shed some light on the effects of differing mechanistic descriptions of a natural phenomenon (each incorporating different sets of materials properties) and on the differentiability of the models when validated against the same data base, the conventional gas precipitation model has been

modified to arrive at "Model Y." Model Y is based on a model presented by Ronchi[44] for the precipitation of gas into highly pressurized bubbles. Ronchi[44] showed that the elastic strain field produced by the overpressurized bubbles increases with gas precipitation and finally leads to a lowering of the precipitation rate. The increased level of gas in solution is available for diffusion to the grain boundaries and for subsequent release to the fuel surface.

Ronchi[44] developed equations of the following form for the interaction energy, Δg, of vacancies and gases in solids with the strain field of the bubble:

$$\frac{d(\Delta g)}{dt} = \pi R_b^2 \varepsilon(R)\left(J_g - J_v\right), \tag{51}$$

with

$$\pi R_b^2 J_g = 4\pi R_b D_g C_g \exp(-\Delta g / kT) \tag{52}$$

and

$$\pi R_b^2 J_v = 4\pi R_b D_v C_v \exp(+\Delta g / kT), \tag{53}$$

where J_g and J_v are the fluxes of gas and vacancies into the bubbles, respectively; $\varepsilon(R)$ is the increase in strain energy caused by the precipitation of one gas atom; and D_v and C_v are vacancy diffusivity and concentration, respectively. The physical basis for Eqs. 51–53 is as follows. Because gas precipitation produces a volume increase, the free energy due to strains created by a volume misfit, g_s, is positive and vanishes when the bubble achieves its equilibrium size, i.e., when vacancy diffusion (plastic deformation) further reduces the internal energy of the system by relieving the strains produced by precipitation. Under steady–state conditions, the energy gain of the gas atoms jumping from the lattice to the gas phase is preponderant and the bubble is an energy well for the gas in the solids. However, the strain energy of the bubble may affect the potential of the incoming atoms: the gas in bubbles has a lower potential than that in the solid, but, within the strain field of the bubble, the potential of the dissolved atoms increases.

The increase in strain energy, g_s, caused by the precipitation of one gas atom is, by definition,

$$\varepsilon(R) = dg_s / dn, \tag{54}$$

where n is the moles of gas precipitated into the bubble. The strain energy in the vicinity of the bubble is given by

$$g_s = \sigma^2 \Omega / \mu, \tag{55}$$

where σ is the stress field around the bubble, Ω is the lattice molecular volume, and μ is the elastic modulus. The stress field around the bubble is given by Ref. 51 as

$$\sigma(x) = (P - 2\gamma / R_b) R_b^3 \left(1 - x_o^3 / x^3\right) / \left(x_o^3 - R_b^3\right), \tag{56}$$

where x is the distance from the center of the bubble and x_o is the radius of the spherical volume on the surface of which the stress is assumed to be completely relaxed. Evaluating $\sigma(x)$ near the bubble surface, and assuming that $x_o >> R_b$ (usually the case), Eqs. 54–56 reduce to

$$\varepsilon(R) = dg_s / dn = 2\Omega / \mu (P_i - 2\gamma / R) dP_i / dn. \tag{57}$$

To evaluate dP/dn, the modified hard-sphere equation of state (Section 2.6.4) is utilized.

Using Eqs. 51–56,

$$\frac{dP_i}{dn} = \frac{kT}{v}\left(\frac{\frac{4}{3}\pi R_i^3 P_i}{RgT} + d_i\right)\left\{v\frac{(1+y)}{(1-y)^3} - v_o f\right.$$

$$\left. + \frac{1}{d_c}\left[\frac{2\Delta Z_i}{d_r} + d_r^2\left(\frac{1}{T_r}(14 d_r - 1.333 / T_r) + 3A_x B_x d_r^2\right)\right]\right\}. \tag{58}$$

Once $\varepsilon(R)$ has been evaluated with Eq. 58, Eq. 51 can be integrated to obtain

$$\exp(+\Delta g / RgT) = \frac{\left[B_v + H - (B_v - H)G(t)\right]}{2B_v\left[1 - G(t)\right]}, \tag{59}$$

where

$$G(t) = \left[(B_v - B' + H)/(B_v - B' - H)\right] \exp(-4\pi < \varepsilon R_b > Ht/RT),$$

$$A = C_g D_g,$$

$$B_v = C_v D_v = D_u,$$

$$B' = 2B_v \exp(+\Delta g/R_g T) \text{ at } t = 0,$$

$$H = \left(B_v^2 + 4AB_v\right)^{1/2}, \text{and}$$

$\langle \varepsilon R \rangle =$ average of εR_b between 0 and t.

In Eq. 59, $C_v D_v$ has been replaced by D_u because U diffusion is rate controlling. The term $\exp(-\Delta g/RT)$ is the precipitation–hindering function: it starts at a given initial value and, for increasing t, tends to an asymptotic value. The modified calculation of gas precipitation in solids consists of multiplying Eqs. 48 and 49 by the precipitation–hindering function. This modification entails the assumption that bubble overpressure will result in a general state of stress in the matrix, which will, on average, hinder bubble nucleation as well as bubble growth by gas atom precipitation. This modified model will be designated in what follows as Model Y. FASTGRASS calculations for Model Y utilize Eqs. 51–59 and incorporate the values of key materials properties listed in Table 4. The thermal component of the gas atom diffusivity listed in Table 4 is that recommended by Matzke;[52] the athermal component is within the scatter of values reported in Ref. 47. At 1500°C, the thermal gas atom diffusivity measured by Matzke[52] is ≈250 times larger than that measured by Cornell (Table 3 and Ref. 46). This variance in reported values of certain materials properties is, in part, responsible for the difficulty in interpreting results of model validation. The values of the nucleation factor, F_n, and the U diffusivity, D_u, are a factor of 500 larger and 200 smaller, respectively, than are those used in the conventional model (Table 3). The value for D_u shown in Table 4 is a factor of 10 larger than the value used in Ref. 35.

3.4 Effect of Materials Properties on the Conventional-Model Calculation of Gas Precipitation in Solids

The different values of the key materials properties listed in Tables 3 and 4 represent experimental uncertainties, which contribute to the difficulty of model validation. For example, Ronchi[44] has criticized the value

Table 4. Values of Key Materials Properties Used in Eqs. 51–59, which Define Model Y

Parameter	Value
D_g (cm^2/s)	$3.9 \times 10^{-2} \exp(-45280/T) + 1.0 \times 10^{-30}K$
F_N	1.0×10^{-4}
D_u (cm^2/s)	$0.01 \exp(-65000/T)$

for the gas bubble nucleation factor, F_N, used by Rest[9] in a conventional-model description of gas precipitation in solids as being "hardly justifiable" in that such a low value of F_N would preclude gas bubble nucleation at relatively low temperatures. However, as will be shown in Section 4.2.1, although the combination of properties listed in Table 3 results in a reduced rate for gas precipitation during the heatup phase of isothermal anneals, the results of calculating bubble size distribution on the basis of the properties listed in Table 3, in the context of the conventional model, are consistent with experimental observations. To assess the effects of the different values of the properties listed in Tables 3 and 4, Model X and Y calculations will be compared with calculations for "Model Z," defined as the conventional model incorporating the properties listed in Table 4 (in contrast to Model X, which incorporates the properties listed in Table 3).

4 Validation 1: Behavior of Fission Gas during Postirradiation Annealing Experiments

4.1 Data Base Selection for Validation of Models X, Y, and Z

The importance of utilizing well–characterized data for model validation should be obvious. Data analysis is performed here with the MINITAB statistical regression model.[53] The data listed in Appendix C were used to generate the scatter plots shown in Fig. 3. The upper half of each panel of Fig. 3 shows a MINITAB plot of the natural log of measured fractional gas release vs. gas release predictions obtained from a linear regression model fit to the data for the experiments reported in Refs. 35–42. The lower half of each panel shows the corresponding plot of the standardized residuals for

the regression fits vs. the natural log of the predictions of the fit. A random distribution of points about the horizontal line at standardized residuals = 0 indicates an absence of bias or systematic error in the regression model.

The regression equations incorporate the reported test temperature and time, the irradiation burnup, the heating rate (when available), and pretest grain size (when available) as independent variables. Table 5 lists the regression equations developed for Figs. 3a-h, along with pertinent statistical information.

The coefficients of the 1/T terms (i.e., slopes of the Arrhenius plots) derived from the regression analyses illustrated in Table 5 vary from 9,595 to 77,673 K. However, groups of data have reasonably consistent slope values: slopes associated with Figs. 3a, f, g, and h vary from 15,765 to 21,669 K; slopes associated with Figs. 3d and e vary from 47,830 to 54,510 K. The standard deviations of the regression fits shown in Table 5 vary from s = 0.21 to s = 1.916. The top half of Fig. 4 shows a MINITAB plot of the natural log of measured fractional gas release vs. gas release predictions obtained from a linear regression model fit to the combined data of Figs. 3a-h. The regression equation developed for Fig. 4 is listed in Table 5.

The bottom half of Fig. 4 shows a plot of the standardized residuals for the regression fit shown in the top half of the figure vs. the natural log of the predictions of the fit. Again, a random distribution of points about the horizontal line at standardized residuals = 0 indicates an absence of bias or systematic error in the regression model. The distribution of points in the bottom half of Fig. 4 shows a high degree of systematic error; the distribution of points tends to fan out as the gas release values become smaller. The presence of systematic error in the data is also readily apparent in Figs. 3b, f, and h, and in the large variation of derived activation energies listed in Table 5 for the data sets shown in Figs. 3a-h. Systematic error is introduced into the data when key operating parameters, such as temperature and the external environment, are not accurately controlled. For example, only two of the eight experiments analyzed in Fig. 3 and Table 5 reported values for the fuel heating rate. Brearly et al.[45] interpreted the variation in release observed by Bridge et al.[38] (see Figs. 3d and 4 and Ref. 38) as due to small changes in the fuel O-to-metal ratio.

The presence of systematic error in the data (e.g., as shown in Fig. 4) complicates the validation of mechanistic models for gas release and

swelling. It is clear that an appropriate data selection method is required to realistically examine the influence of differing descriptions of the phenomena and uncertainties in selected materials properties on the validation results. The statistical regression analysis described above is proposed for the selection of a "reasonably" well-characterized data base for gas release from irradiated fuel under transient heating conditions. The selection criteria consist of a "reasonably" small value of the standard deviation, s, and the absence of any undue bias in the distribution of the standardized residuals. In the next section, it will be demonstrated that an appropriate data selection method, such as the one being proposed, is required to realistically compare Models X, Y, and Z for gas precipitation in solids during postirradiation annealing experiments.

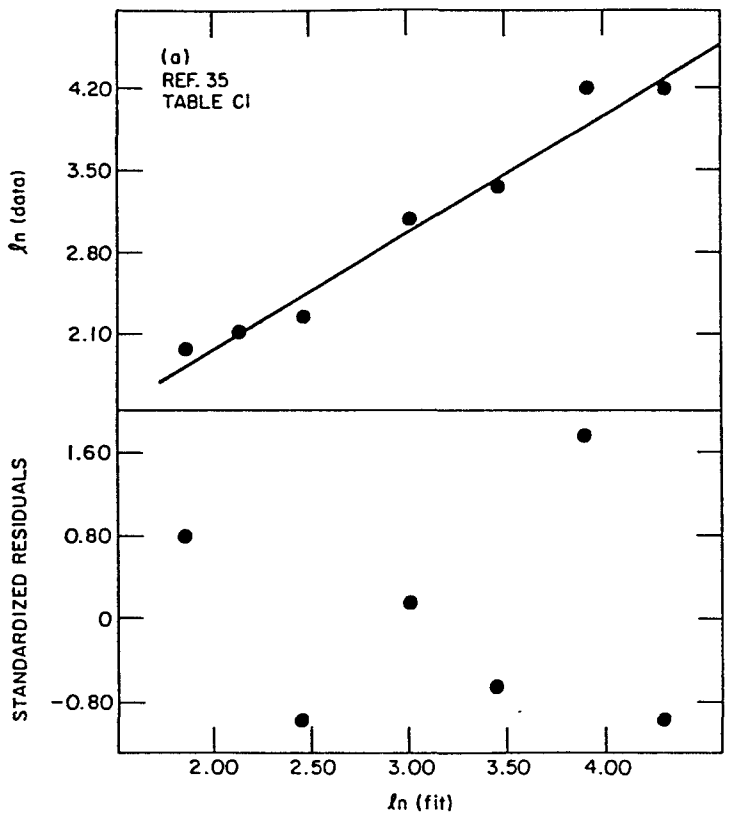

Fig. 3. The results of MINITAB regression analyses for data (individual) from Refs. 35–42 and Tables C1–C8. The upper and lower parts of the figures show the natural log of the observed gas release, and the standardized residuals, respectively, plotted against the log of the predictions obtained with the regression fit. The open circles show the location of two overlapping points. In each case, the solid diagonal line indicates perfect agreement between the regression fit and the data.

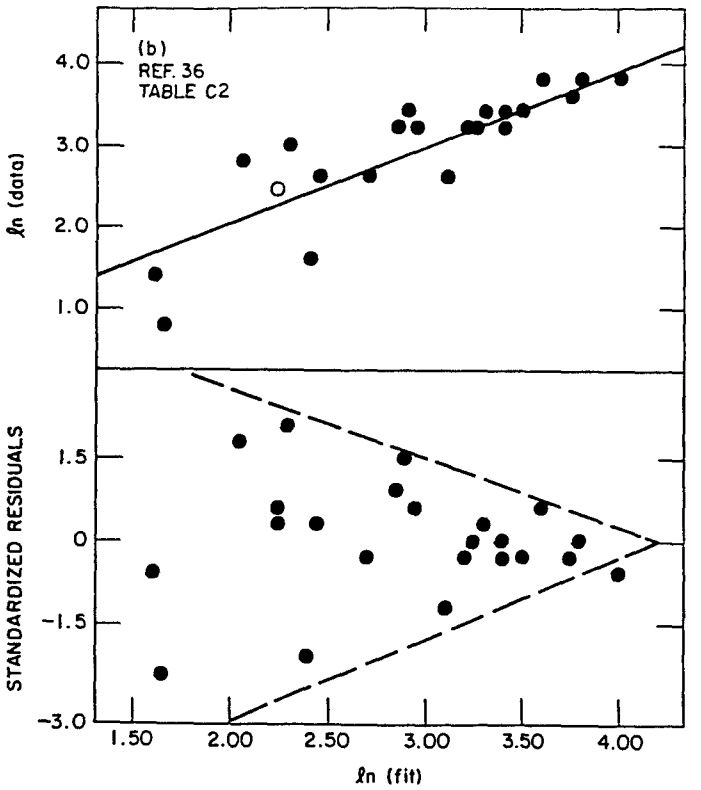

Fig. 3 (Cont'd)

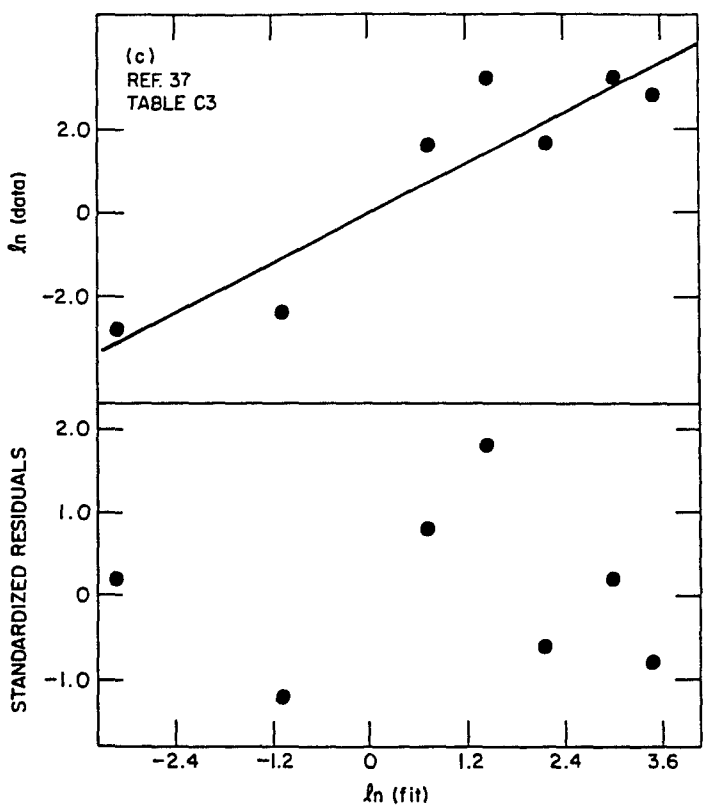

Fig. 3 (Cont'd)

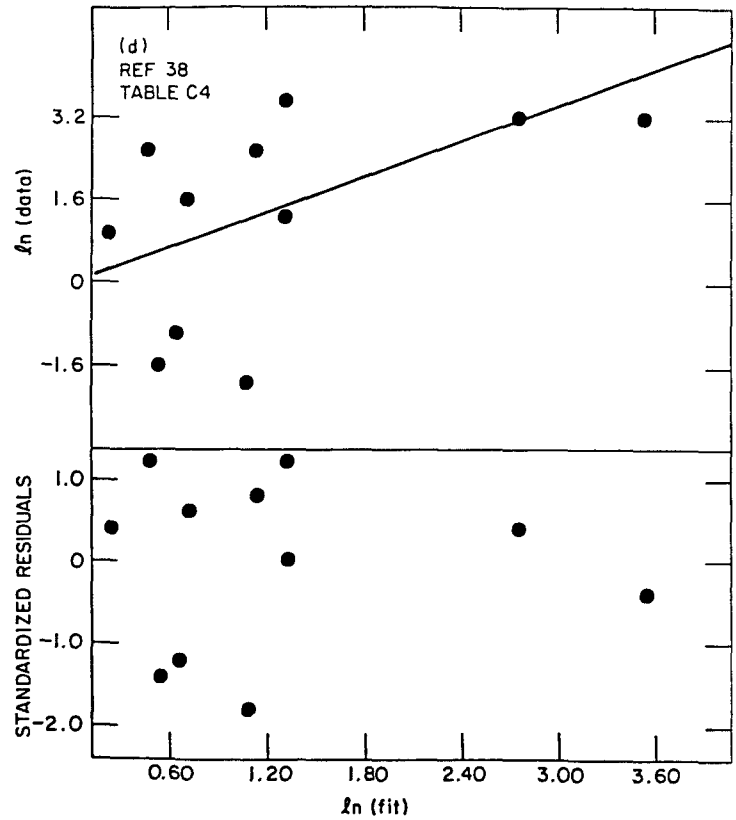

Fig. 3 (Cont'd)

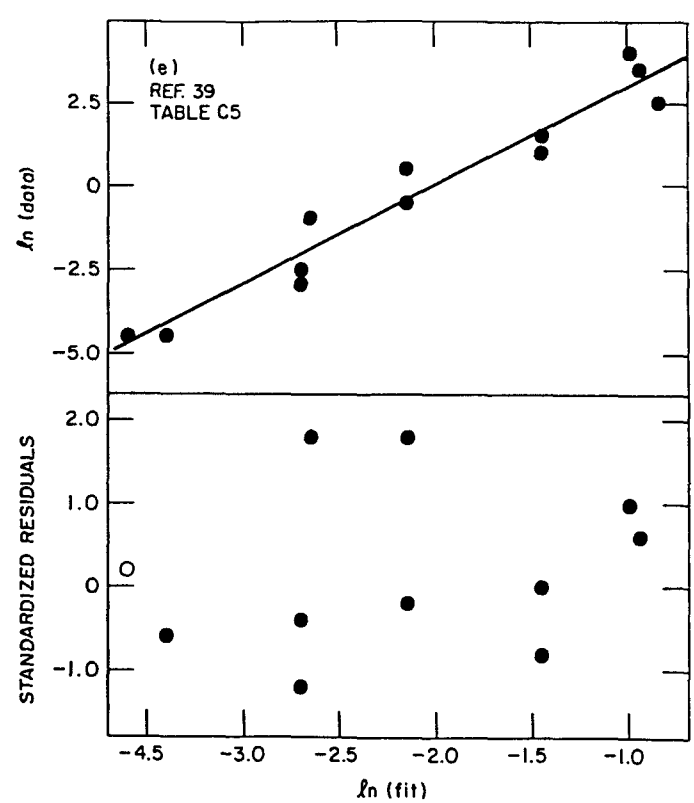

Fig. 3 (Cont'd)

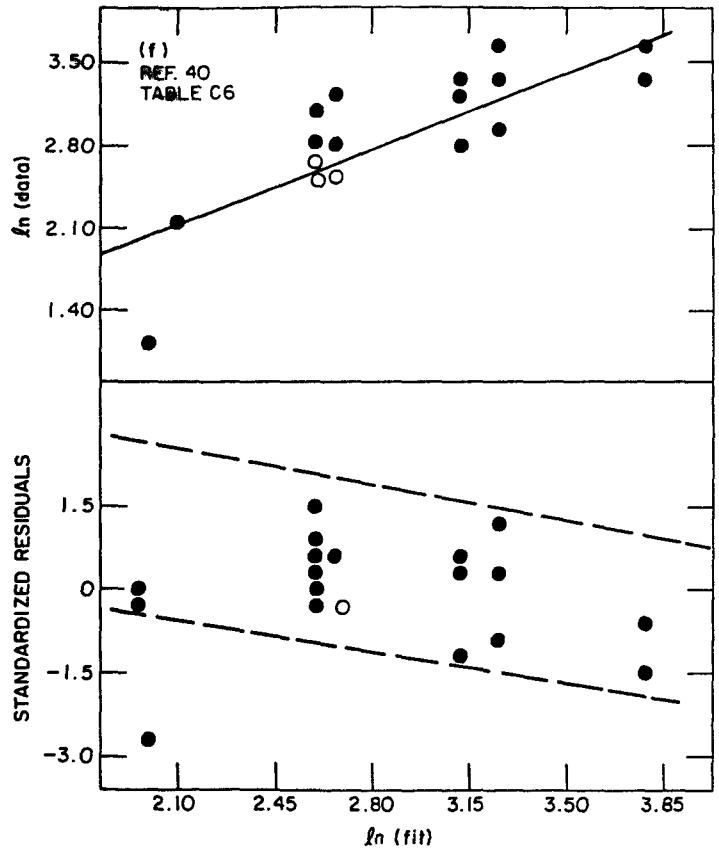

Fig. 3 (Cont'd)

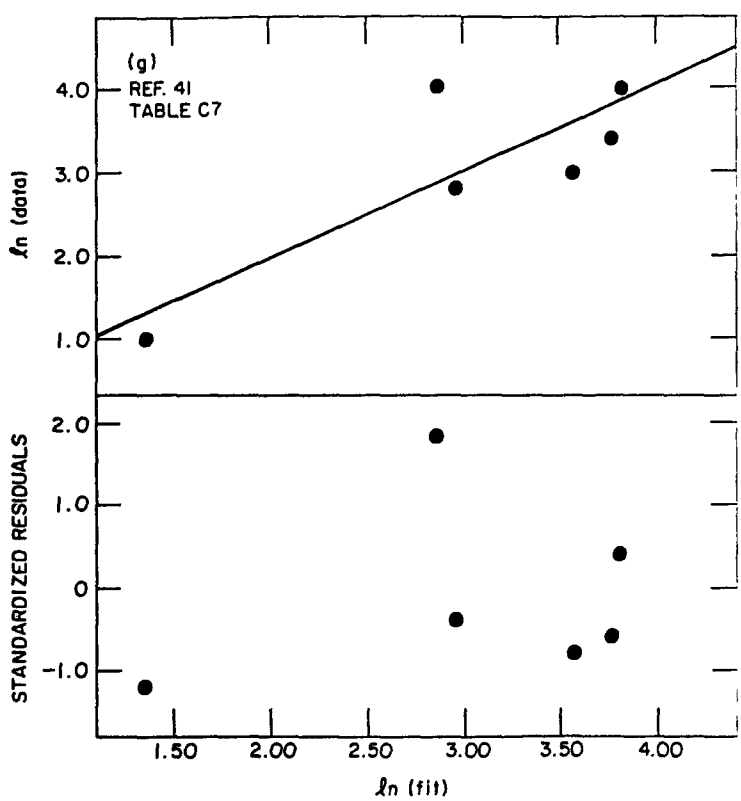

Fig. 3 (Cont'd)

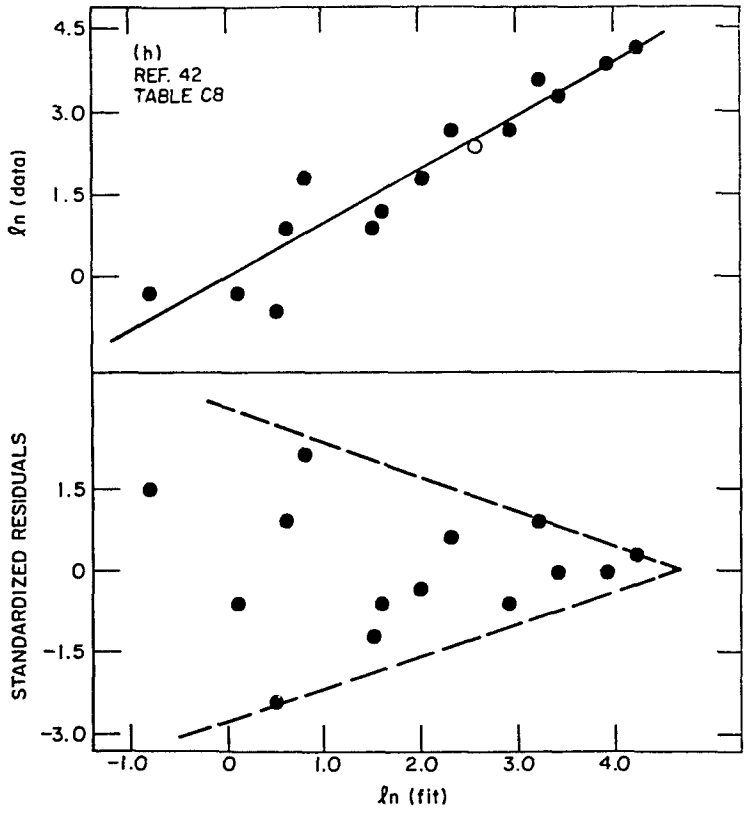

Fig. 3 (Cont'd)

4.2 Comparison of Models X, Y, and Z for Gas Precipitation in Solids

The data characterized by the smallest value of s and an absence of any undue bias in the distribution of standardized residuals are those of Ref. 35 (see Fig. 3a and Table 5), listed in Table C2 in Appendix C. These data were accumulated by a sweep gas technique and thus have the added advantage of exhibiting time-dependent gas release.[54] In addition, the data from Ref. 35 consist of microstructural characterizations of the retained fission gases (e.g., intra and intergranular bubble size distributions and grain size). If we arbitrarily assign the value of s = 0.5 as an acceptable level for the standard deviation (a factor of 2.5 times larger than the standard deviation of the data from Ref. 35) and exclude any data with an obvious bias in the standardized residuals (Figs. 3b, 3f, and 3h), only the data from Ref. 35 remain "reasonably" well characterized. In this section, Models X, Y, and Z will be compared on the basis of model predictions for the experiment of Ref. 35. To highlight the effect of systematic error on limiting the validation value of a data base, the data of Ref. 36 (s = 0.41, visible bias in the standardized residuals) will also be used to assess predictions of Models X, Y, and Z.

Table 5. Regression Equations Developed for Figs. 3 and 4, with Pertinent Statistical Information

Fig.	Equation[a]	s[b]	R^2 (adj)[c] (%)
3a	ln(data) = 12.9 - 19515/T	0.2100	94.8
3b	ln(data) = 6.54 - 9595/T + 0.361 ln(t) + 0.517 ln(BU)	0.4080	72.4
3c	ln(data) = 37.3 - 77673/T + 1.11 ln(t)	1.220	77.3
3d	ln(data) = 42.6 - 47830/T - 2.00 ln(t)	1.9160	7.7
3e	ln(data) = 23.0 - 54510/T + 1.88 ln(dT/dt)	0.7882	92.8
3f	ln(data) = 11.3 - 17804/T + 1.54 ln(BU)	0.3311	69.7
3g	ln(data) = 10.7 - 15765/T	0.6628	63.9
3h	ln(data) = 14.0 - 21669/T - 1.99 ln(BU)	0.5573	86.6
4	ln(data) = 13.1 - 22673/T + 0.253 ln(t) + 0.295 ln(BU)	1.494	37.5

[a]Only independent variables having t-ratio absolute values greater than 2.0 (which is often regarded as indicating a significant relationship between the dependent and independent variables) are included (except for Fig. 3d, where none of the independent variables have t-ratios greater than 2).

[b]s is the root-mean-square (standard) deviation.

[c]R^2 (adj) is the proportion of the total sum-of-the-squares that is explained by the regression line, adjusted for degrees of freedom (when the sample size for the regression is small, R^2 adjusted for degrees of freedom may differ considerably from the unadjusted value).

4.2.1 Simulation of In-Reactor Irradiation

Calculations from Models X, Y, and Z were incorporated within the context of the FASTGRASS code. Because the as-irradiated condition of the fuel is an important input into transient fission–gas response, it is clearly necessary to identify differences in model predictions for the as-irradiated distribution of retained gases to more fully understand differences in the transient calculations.

A one–node simulation of irradiation and a subsequent annealing experiment were performed. A one-node simulation is adequate for low–power irradiations where diffusion is primarily athermal, and for transients

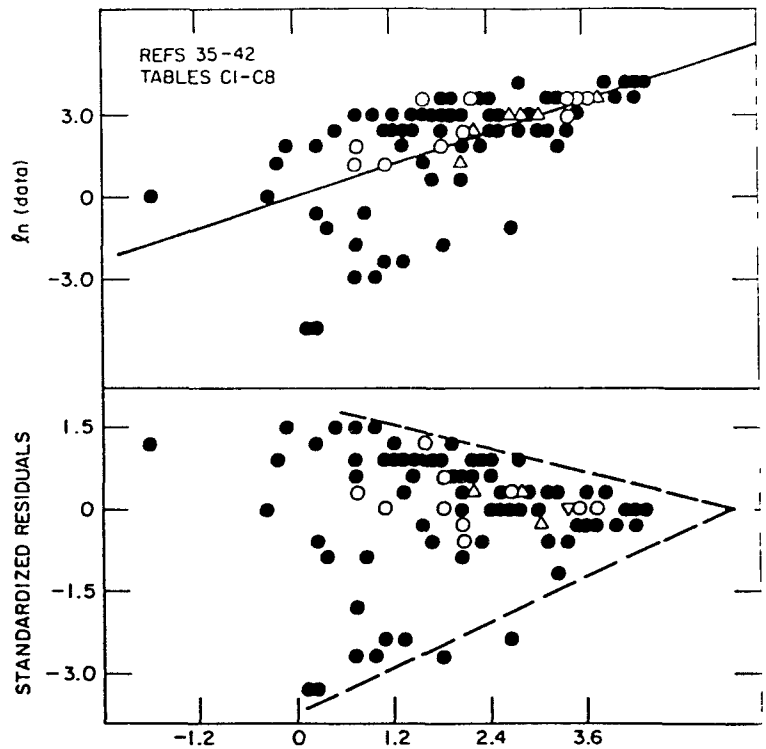

Fig. 4. The results of MINITAB regression analyses for data (total) from Refs. 35–42 and Tables C1–C8. The upper and lower parts of the figures show the natural log of the observed gas release, and the standardized residuals, respectively, plotted against the log of the predictions obtained with the regression fit. The open circles, upright triangles, and inverted triangles show the location of two, three, and four overlapping points, respectively. The solid diagonal line indicates perfect agreement between the regression fit and the data.

where relatively low temperature gradients are encountered. The as-irradiated condition of the fuel (fuel burnup of ≈2%) was simulated with the assumption of an average irradiation temperature of 1273 K. Table 6 shows values of average intragranular bubble radius and density, fractional amount of gas trapped, and fraction of gas on grain boundaries calculated with Models X, Y, and Z, compared with estimates obtained from electron microscopy of irradiated fuel.[55]

The differences between the Model X, Y, and Z calculations, shown in Table 6, can be explained in terms of the different values of the key materials properties used (Tables 3 and 4). Model Y calculations result in a higher density of bubbles and a greater percentage of trapped gas than Model X because of a higher rate of gas bubble nucleation (i.e., higher value

Table 6. Model Predictions for As-Irradiated Fuel Compared with Experimental Estimates

Model	Bubble Radius (nm)	Bubble Density (m^{-3})	Fraction Gas Trapped	Fraction Gas on Boundaries
X	0.65	5×10^{23}	0.10	0.15
Y	0.27	2.6×10^{25}	0.375	0.11
Z	0.38	1.8×10^{25}	0.674	0.06
Experimental Estimate	0.5	1×10^{24}	-	-

of F_n). On the other hand, the Model–Y calculation results in smaller size bubbles owing to a smaller value for the athermal gas atom diffusivity. The lower atom mobility reduces the bubble growth rate in an environment where the bubble shrinkage rate remains relatively constant (both calculations use the same model for gas atom re-solution from bubbles). Model–Y prediction of the fraction of gas trapped (0.375) is consistent with the value (0.40) assumed by Small and MacInnes[54] to provide agreement between model calculations (SINGAR) and the data of Ref. 35.

Model–X calculation of the fraction of gas trapped in bubbles results in the lowest percentage of the three models: 10%, vs. 38% for Model Y and 67% for Model Z. The effect of increased values for F_n and D_g on gas precipitation is evident in the increased value for the fraction of gas trapped calculated with Model Z, compared to Model X. The trapped–gas fraction calculated with Model Y is lower than that calculated with Model Z, owing to the asymptotic value of the precipitation–hindering function given in Eq. 59. In contrast to Ronchi's criticism of Model X, discussed in Section 3.4, values calculated with Model X for the average bubble radius and bubble density are in excellent agreement with the experimentally observed quantities listed in Table 6.

4.2.2 Simulation of Postirradiation Annealing Experiments

FASTGRASS calculations with Models X, Y, and Z for the postirradiation annealing experiments incorporated the steady-state conditions discussed above, a 60–s hold at 1273 K (out of reactor), a ramp to temperature at 12.5 K/s, and a hold at temperature for ≈1800 s. Figures 5a-5f show values for fractional gas release vs. annealing time, calculated with Models, X, Y, and Z, for annealing temperatures of 1500, 1600, 1700, 1800, 1900, and 2000°C, respectively. Also shown in Figs. 5a-f are the time-dependent data from Ref. 54. For each experiment, the cumulative release data are represented by a band covering the range of reported experimental error. The results from Models X, Y, and Z are shown as continuous curves. As is demonstrated in Figs. 5a-f, the time dependence of the fractional release is reproduced more adequately by Model Y than by Models X or Z. In general, Model X predictions are in better agreement with the data than the predictions from Model Z. In these experiments, the observed early rapid release, followed by a flattening of the release rate, is qualitatively reproduced by Model Y (the data at 1900°C are anomalous in that the release increases with a decrease in temperature, e.g., compare with results obtained at 2000°C).

If only the total gas release values at the end of the anneal were available, differentiation between Models–X and –Y would be ambiguous. An explanation of the differences between Model–X and –Y predictions for total gas release, based on uncertainties in various materials properties (e.g., grain size), could easily be provided. Model validation, however, is most often performed with only total gas release data.

To underscore the importance of "reasonably" well–characterized data for model validation, it is instructive to compare Models X and Y with data that show bias in the standardized residuals. The statistical analysis performed in Section 4.1 for the data of Burbach and Zimmermann[36] gave an acceptable standard deviation of 0.4080 (Table 5), but a clear bias in the standardized residuals (Fig. 3b). Figure 6a shows Model Y–calculated values of fractional gas release vs. annealing time for a hold temperature of 1800°C at as-irradiated burnups of 0.3, 0.9, and 3.7 at.%. Also shown in Fig. 6a are the time–dependent data from Ref. 54. As is evident upon inspection of Fig. 6a, the effect of systematic bias in the data precludes any definitive conclusion on the validity of Model Y for describing gas precipitation in solids during an 1800°C anneal.

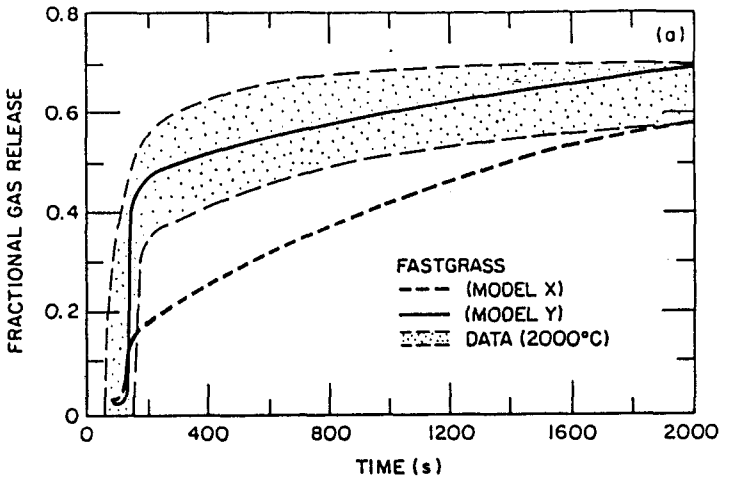

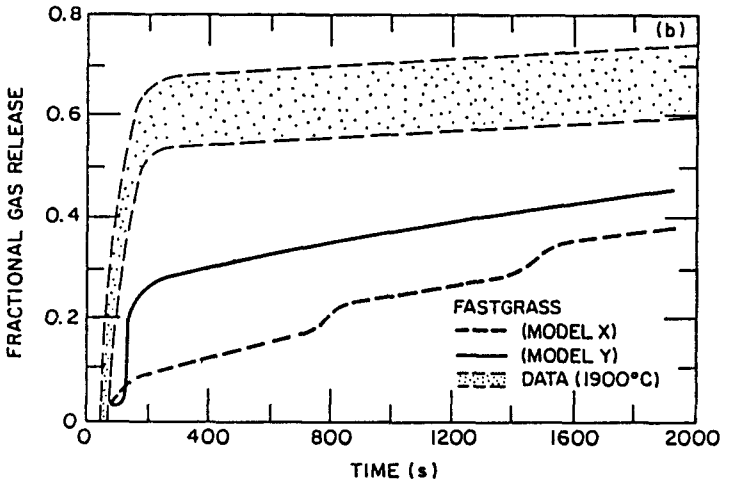

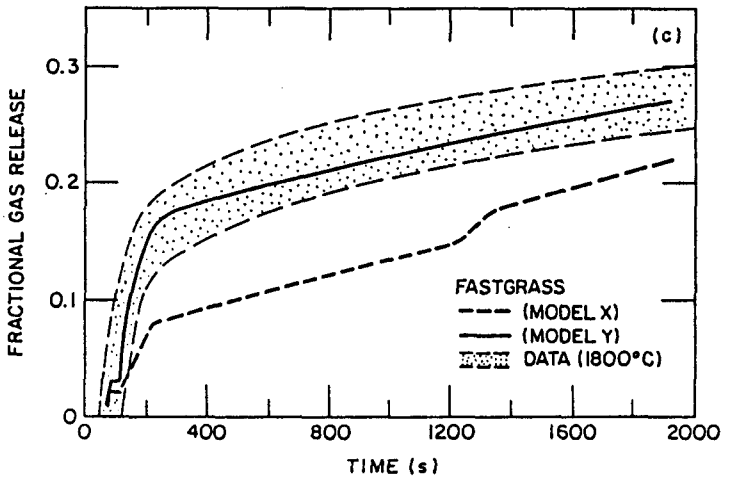

Fig. 5.
Fractional gas release for the postirradiation annealing experiments of G. J. Small (Refs. 35 and 54), calculated with FASTGRASS Models X, Y, and Z and compared with measured values for hold temperatures of (a) 2000, (b) 1900, (c) 1800, (d) 1700, (e) 1600, and (f) 1500°C

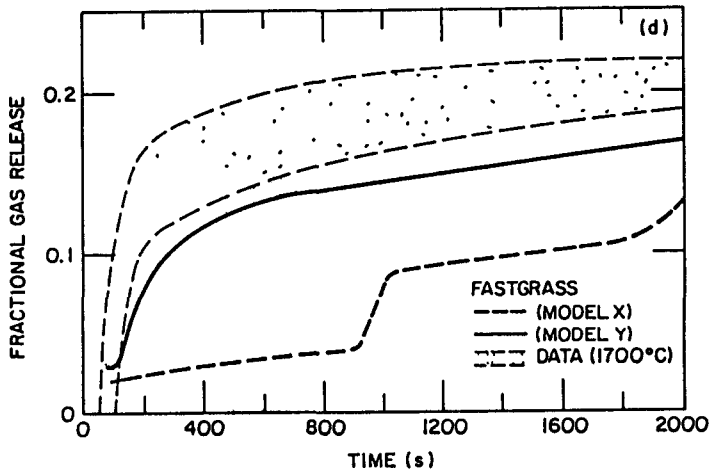
(d)
FRACTIONAL GAS RELEASE
0.2
0.1
0
0
400
800
1200
1600
2000
TIME (s)
FASTGRASS
(MODEL X)
(MODEL Y)
DATA (1700°C)

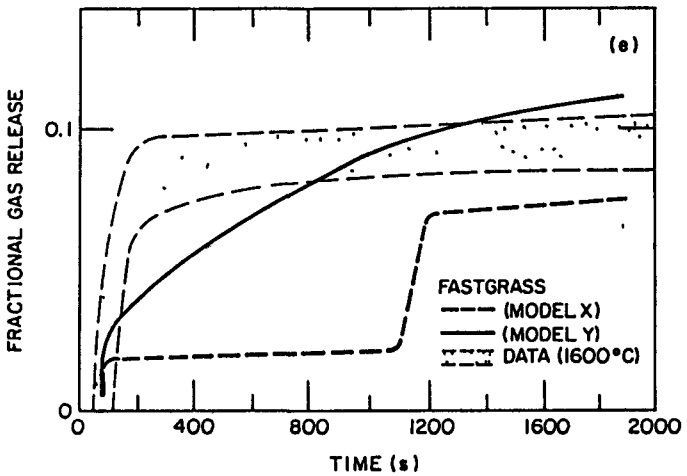
(e)
FRACTIONAL GAS RELEASE
0.1
0
0
400
800
1200
1600
2000
TIME (s)
FASTGRASS
(MODEL X)
(MODEL Y)
DATA (1600°C)

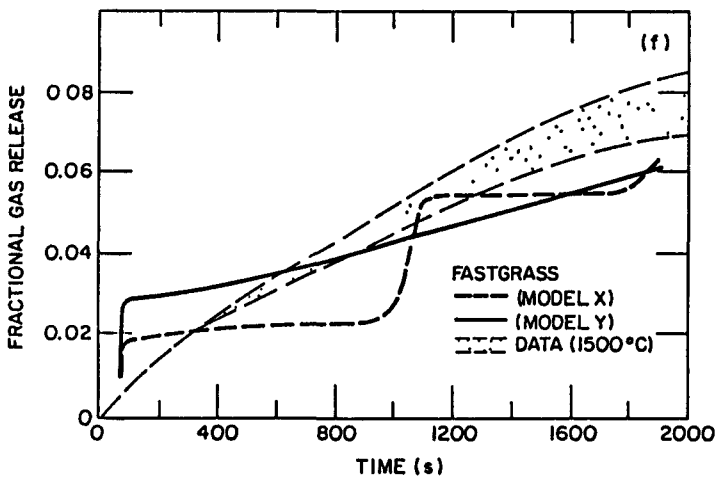
(f)
FRACTIONAL GAS RELEASE
0.08
0.06
0.04
0.02
0
0
400
800
1200
1600
2000
TIME (s)
FASTGRASS
(MODEL X)
(MODEL Y)
DATA (1500°C)

Fig. 5 (Cont'd)

Figures 6b and c show values for fractional gas release vs. annealing time, calculated with Models X and Y, for hold temperatures of 1900°C and 2000°C, respectively, compared with time-dependent data from Ref. 54. Systematic bias is less effective in the higher-temperature/higher burnup regime (e.g., see Fig. 3b). The results shown in Figs. 6b and c, although not nearly as definitive as those shown in Figs. 5a-f, suggest that Model Y is a more appropriate description of precipitation kinetics in these experiments than Model X.

A more rigorous level of model validation can be obtained if microstructural data are available. Figure 7 shows bubble diameters vs. temperature at 1800 s into the anneal, as calculated with Models X and Y, compared with data from Ref. 35 (obtained by electron microscopy) on mean bubble diameter. The results shown in Fig. 7 indicate that, although Model X is more in line with the data, neither Model X nor Model Y can explain the observed bubble diameters. Model Y provides smaller values of bubble diameter than Model X, owing to the precipitation-hindering effect of overpressurized bubbles. This difference in model prediction will be more fully discussed in the following section.

It would be easy to dismiss the validity of Models X and Y on the basis of the results shown in Fig. 7. However, one must be very careful in interpreting the measured "mean-bubble" diameter and the FASTGRASS-calculated "average-size-bubble" radius. It is not obvious a priori that the measured and calculated quantities are one and the same. For the calculated average size, the average is taken on the sink strength (i.e., from the sum of the sink diameters), whereas the experimental size histograms usually refer to the observable bubble volume distribution (i.e., they are measured and scaled on the basis of the largest sizes with morphologically significant concentrations; the smallest classes are practically cut off by the optical resolution limits of the correspondingly adopted detection method, transmission electron microscopy, scanning electron microscopy, etc.).

To examine this issue further, GRASS-SST code calculations of the intragranular bubble size distribution, incorporating the X and Y gas precipitation models, were performed for the 1700°C anneal of Ref. 35. Figure 8 shows the GRASS-SST-calculated values of the bubble number density vs. the mean bubble diameter for anneal times of 300 and 900 s. Also shown in Fig. 8 are the FASTGRASS (Model X and Y)-calculated and the

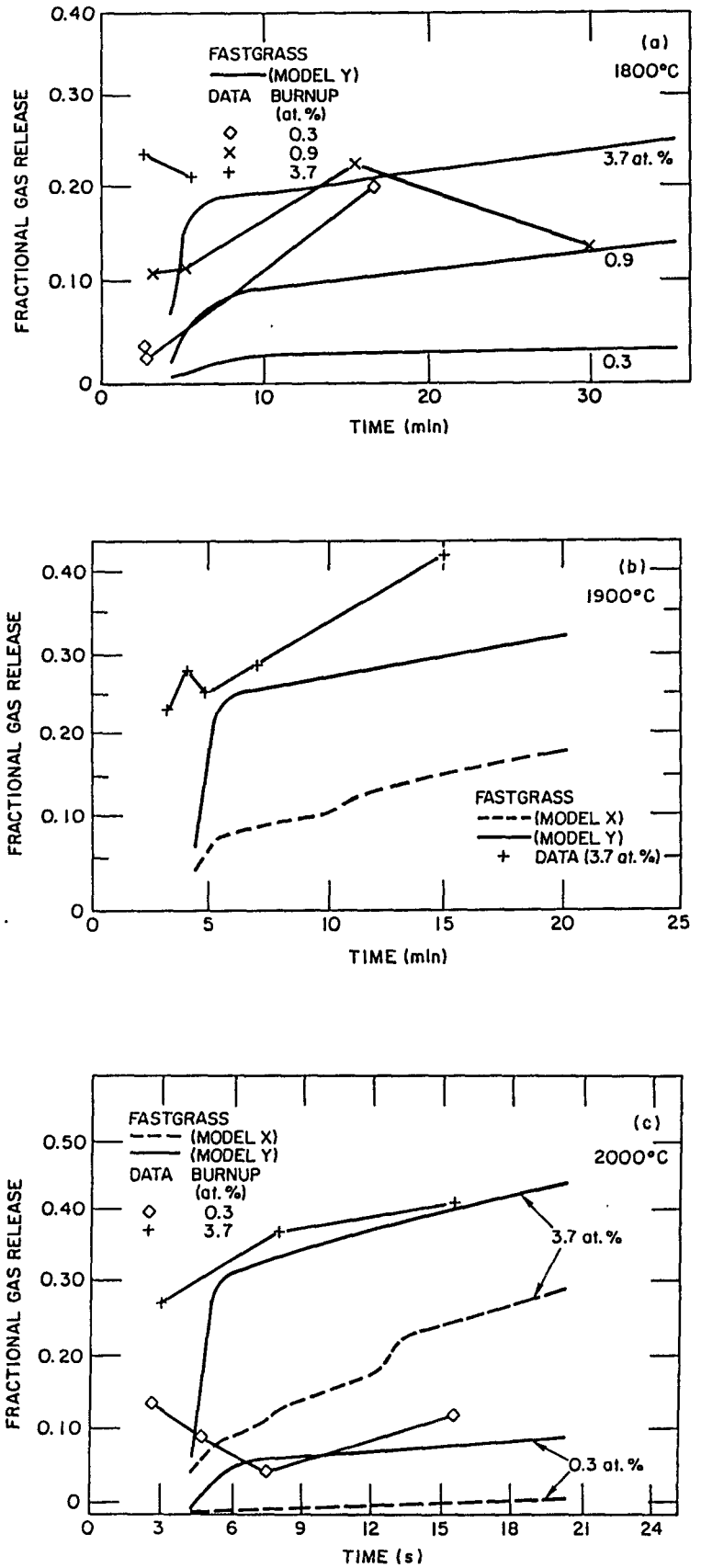

Fig. 6.
Fractional gas release as a function of as-irradiated burnup for the post-irradiation annealing experiments of Burbach and Zimmermann (Ref. 36), calculated with FASTGRASS Models X and/or Y, compared with measured values for hold temperatures of (a) 1800, (b) 1900, and (c) 2000°C. Lines connecting the data are to help guide the eye.

experimentally determined quantities. The experimental observations in Fig. 8 include the reported uncertainty (±1 standard deviation) in mean bubble diameter (no uncertainty in bubble counting was reported). As shown in Fig. 8, both the FASTGRASS–calculated and the experimentally determined bubble densities are in reasonable agreement with the GRASS-SST–calculated bubble size distributions: the FASTGRASS–calculated densities represent the peak region of the GRASS-SST–calculated distribution (i.e., an average of the bubble size distribution); the observed quantities reflect bubble counting and diameter measurements within the limit of experimental resolution. In addition, the measured bubble size histograms in Ref. 35 are in good agreement with the calculated results shown in Fig. 8. The results shown in Figs. 7 and 8 demonstrate that great care must be taken when comparing calculated bubble densities based on "average bubble size evolution" models with measured quantities.

4.3 Discussion

The qualitative (and quantitative) differences between the Model–X, –Y, and –Z predictions, discussed in Section 4.2.2, have been ascribed to differences in the kinetics of gas precipitation in solids. It is important to point out that gas precipitation is not the only mechanism operative in describing gas release under conditions of postirradiation annealing: a complete description of intergranular gas bubble behavior is required to model the progress of the gas after its arrival at the grain boundaries. Within the context of the FASTGRASS code, Models X, Y, and Z have all incorporated the same model for intergranular bubble behavior (see Sections 2.2–2.3). However, it is clear that differences in the as-irradiated bubble size distribution (as a function of fuel morphology), as well as differences in intragranular behavior during the anneal, can affect the intergranular bubble response and hence the time–dependent release predictions. The Model X, Y, and Z results, shown in Figs. 9a–c, respectively, help clarify the role of gas precipitation in solids under isothermal annealing conditions. Plotted in Figs. 9a–c are the time–dependent fractional gas release, the fraction of intragranular gas in bubbles, and the fraction of the retained gas that resides within the grains for the 1800°C anneal of Small[35] (corresponding to the results shown in Fig. 5c). Also shown in Figs. 9a–c are the time–dependent data, represented by a band covering the range of reported experimental error.

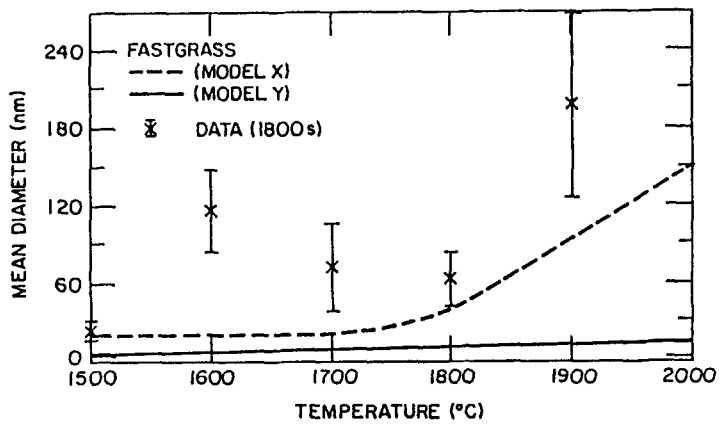

Fig. 7.
Mean bubble diameter, calculated with FASTGRASS Models X and Y, compared with measured values from Ref. 35. The error bars on the data reflect a reported variation of plus or minus one standard deviation in the observed values.

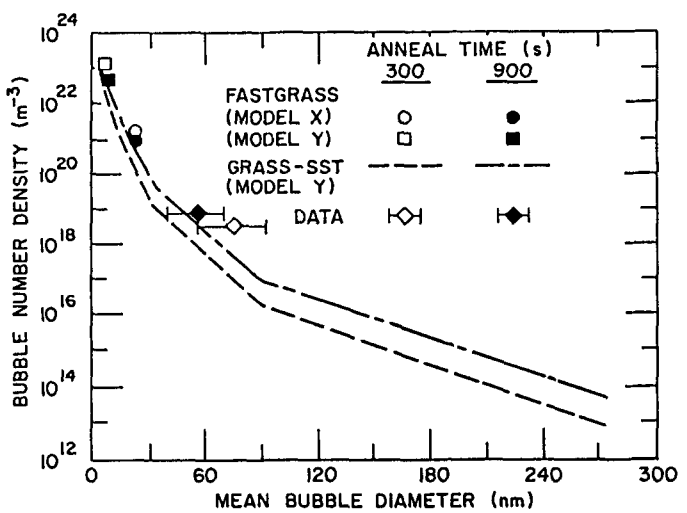

Fig. 8.
Intragranular bubble density as a function of mean bubble diameter for anneal times of 300 and 900 s, calculated with FASTGRASS Models X and Y and GRASS–SST Model Y, compared with measured values from Ref. 35

As shown in Fig. 9, Models X and Y provide for a delayed precipitation of the atomic fission gas, compared to Model Z, which predicts that 100% of the intragranular gas has precipitated into bubbles by ≈90 s into the anneal, compared with ≈2000 s predicted by Model X and ≈375 s predicted by Model Y. The result of the delayed precipitation is the availability of intragranular atomic fission gas for diffusion to the grain boundaries. The fission gas diffuses to the boundaries at a rate set by the gas atom diffusivity. This combination of availability and mobility is reflected in the differences between the model calculations of the fraction of the retained gas that resides within the grains: at ≈400 s into the anneal, Model Y predicts that this fraction is ≈70%, compared to ≈30% predicted by Model X, and 88% predicted by Model Z. Although Model X predicts a delayed precipitation of gas in bubbles, the relatively low value for the gas atom diffusivity results in less gas release to the grain boundaries. Thus, the amount of gas reaching

the grain boundaries is greater for Model Y than for either Model X or Model Z.

The effect of bubble overpressurization on gas precipitation as a function of the hold temperature is further demonstrated by the results shown in Fig. 10, which shows the excess pressure (overpressure) in intragranular bubbles as a function of annealing time for the 1600, 1800, and 2000°C anneals of Small,[35] as calculated by Model Y. As shown in Fig. 10, the excess pressure falls rapidly from an initial value reached at the end of the heatup to a somewhat stable value that is maintained for the duration of the experiment. Because of decreased vacancy diffusivity, D_u, experiments performed at lower temperatures give larger values for bubble overpressure. Thus, anneals performed at lower temperatures will sustain a larger percentage of gas atoms in solution within the grains for a longer period of time than those performed at higher temperatures.

If very little gas is left within solution at the higher temperatures, one would expect a flattening out of the fractional release curve as a function of time for the anneals at higher temperatures, shown in Figs. 5a-c. However, as is evident from Figs. 5a-c, the fractional release continues to increase, even at the end of the temperature hold. This calculated (and observed) behavior is due to the effects of a grain-growth/grain-boundary–sweeping mechanism. As will be shown in Section 7.1.2, within the conventional Model X theory, fission gas, I, and Cs release from irradiated high-burnup fuel in a flowing–steam atmosphere during in–cell heating tests to 1700-2000°C can be interpreted in terms of a grain-growth/grain-boundary–sweeping mechanism that enhances the flow of fission gas and volatile fission–product atoms from within the grains to the grain boundaries. Fission–product release as a function of time (heatup and isothermal hold) is predicted accurately by the model, as is the observed grain growth.

Figure 11 shows the results of FASTGRASS calculations for the 1800°C Small[35] anneal based on the Model Y gas precipitation model with and without the mechanistic grain-growth/grain-boundary–sweeping model (see Section 7). As shown in Fig. 11, calculations performed without the grain-growth/grain-boundary–sweeping model give a flat fractional release curve after an anneal time of ≈200 s has been reached. The reason for this is that after ≈200 s into the anneal, the intragranular gas is fully precipitated into bubbles (see Fig. 9b), and the retained fission gas is basically frozen within the material (for these isothermal conditions, the bubble mobility is

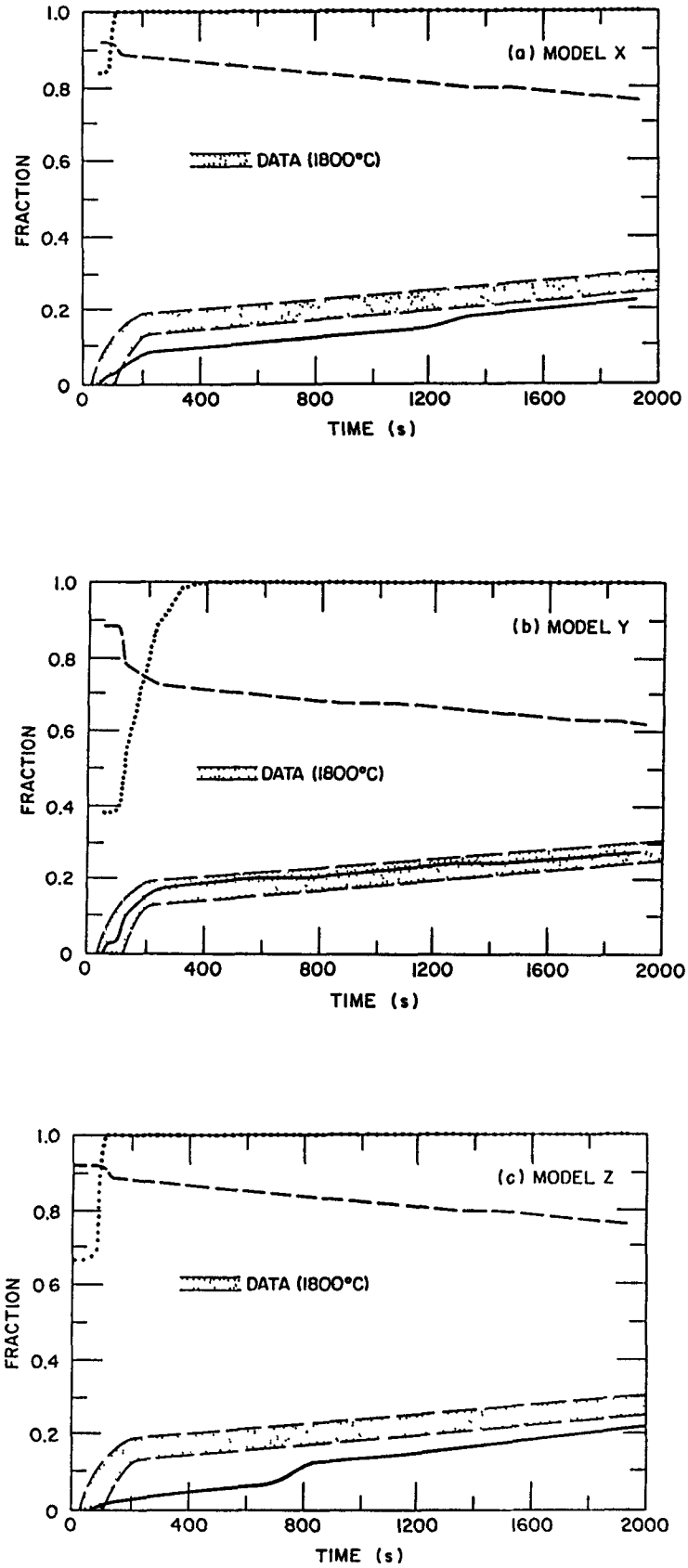

Fig. 9.
Fractional gas release (solid line), fraction of gas retained in grain lattice (dashed line), and fraction of gas in fission-gas bubbles (dotted line), as a function of time for the 1800°C postirradiation anneal experiment of Small (Refs. 35 and 54), calculated with (a) FASTGRASS Model X, (b) FASTGRASS Model Y, and (c) FASTGRASS Model Z, measured values for fractional gas release

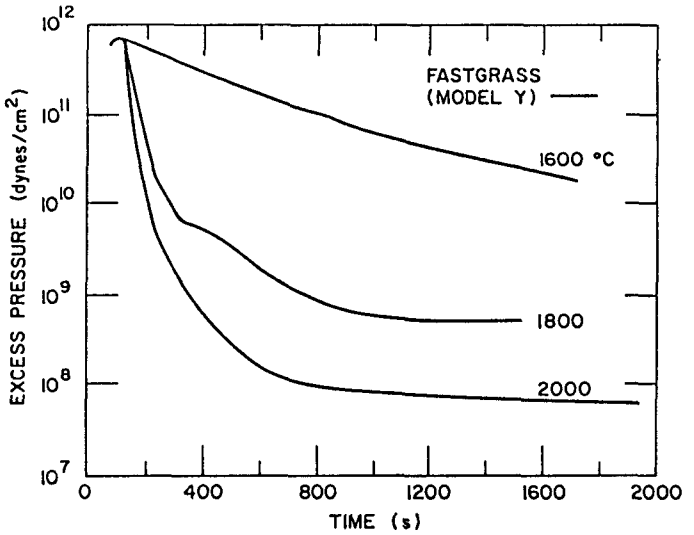

Fig. 10.
Bubble excess pressure as a function of time for three values of the hold temperature, calculated with FASTGRASS Model Y

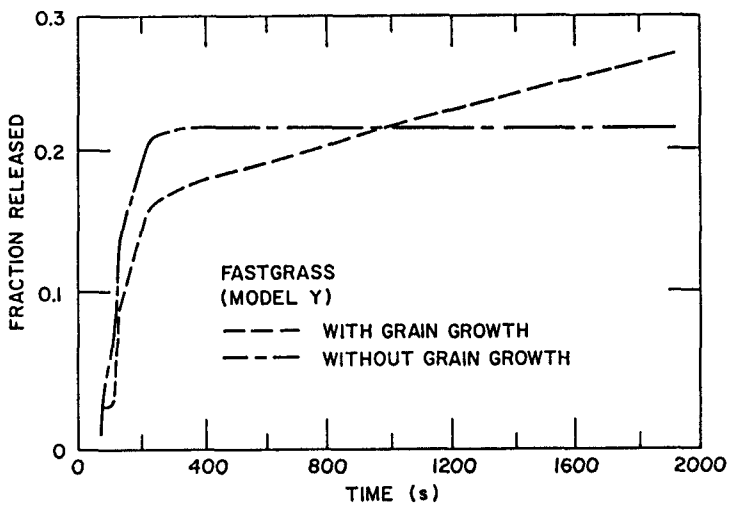

Fig. 11.
Fractional gas release as a function of time for the Small[35] 2000°C post-irradiation anneal experiment with and without the effects of a grain-growth /grain-boundary sweeping model, calculated with FASTGRASS Model Y

effectively zero). Calculations performed with the grain-growth/grain-boundary-sweeping model predict that the grains grow, on average, from an initial size of 8 μm to a final size of ≈8.5 μm. This magnitude of grain growth is consistent with the measured[35] pre and posttest mean linear grain sizes of 5.6 ± 0.3 μm and 7.14 ± 3.65 μm, respectively.

4.4 In-Pile Gas Release

Figure 12 shows predicted fission-gas release as a function of fuel burnup, and compares these results with the data of Zimmermann.[56] Uranium dioxide fuel with a fission rate of 10^{14} f cm^{-3} s^{-1} was used in these experiments. A temperature gradient of 1000°C s^{-1} and grain diameters between 1 and 10 μm were used for the calculation. Four different sets of

calculated curves were generated for average fuel temperatures of 1250, 1500, 1750, and 2000 K. The use of relatively small grain diameters for the calculation of the low-temperature Zimmermann[56] data agrees with the results obtained by other authors.[57] Presumably, the use of relatively small "effective" grain diameters is required to simulate, to some degree, subgrain-boundary formation, which may have occurred in this fuel. The 1250- and 1500-K data are bracketed by predictions based on 1- and 2.5-μm grain sizes, respectively. The 1500- and 2000-K data are bracketed by predictions based on 2.5- and 5-μm, and 5- and 10-μm grain sizes, respectively. Again, agreement between theory and data is reasonable.

Figure 13 shows calculated end-of-life gas release for fuel irradiated in the Carolinas-Virginia Tube Reactor (CVTR), the H. B. Robinson (HBR) No. 2 Reactor, and the Saxton Reactor, compared with measured values. Also shown in Fig. 13 are the predicted and measured end-of-life releases of Turnbull-Friskney[58] and Zimmermann.[56] To supply FASTGRASS with the proper operating conditions for the CVTR, HBR, and Saxton irradiations, FASTGRASS was coupled to an experimental LWR fuel-behavior code generated by modifying[59] the LIFE fuel-performance code. As is evident from Fig. 6, theory predicts the data reasonably well for fission-gas release between 0.2 and 100% and for burnups between 0.7 and 10 at.% (~7000-100,000 MWd/MT). The largest differences between predictions and

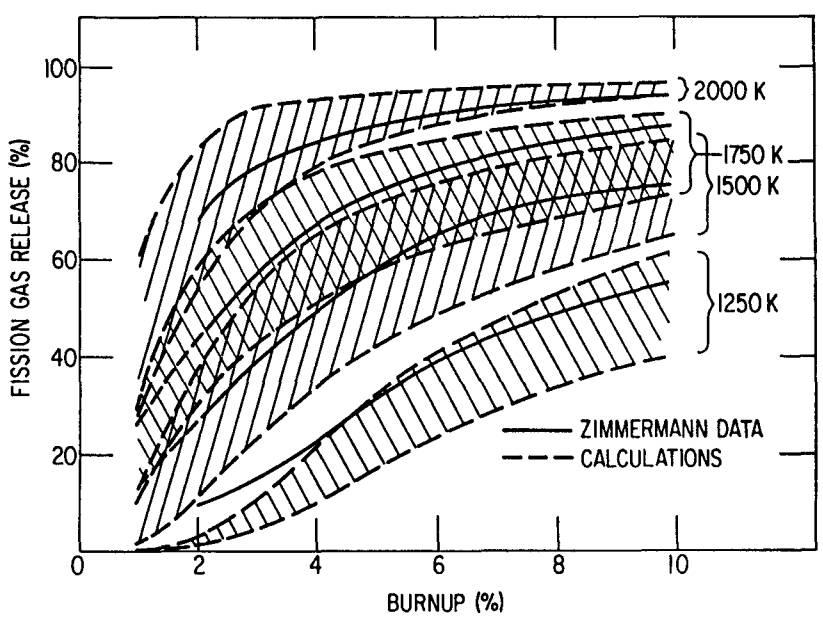

Fig. 12. Predicted fractional fission-gas release at 1250, 1500, 1750, and 2000 K, compared with the data of Zimmermann[56]

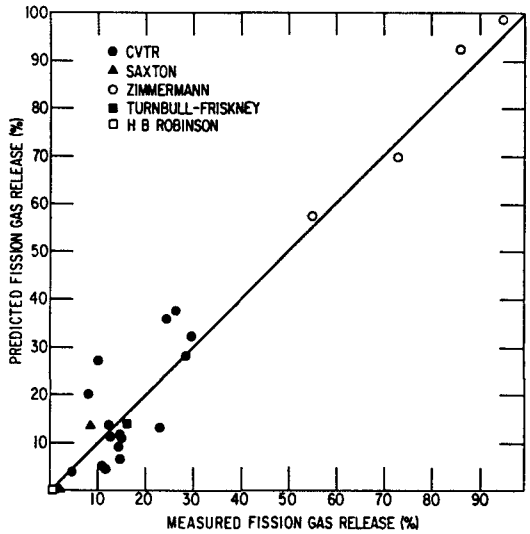

Figure 13.
Comparison of theoretical predictions with measured end-of-life gas release. The diagonal line indicates perfect agreement between theory and experiment.

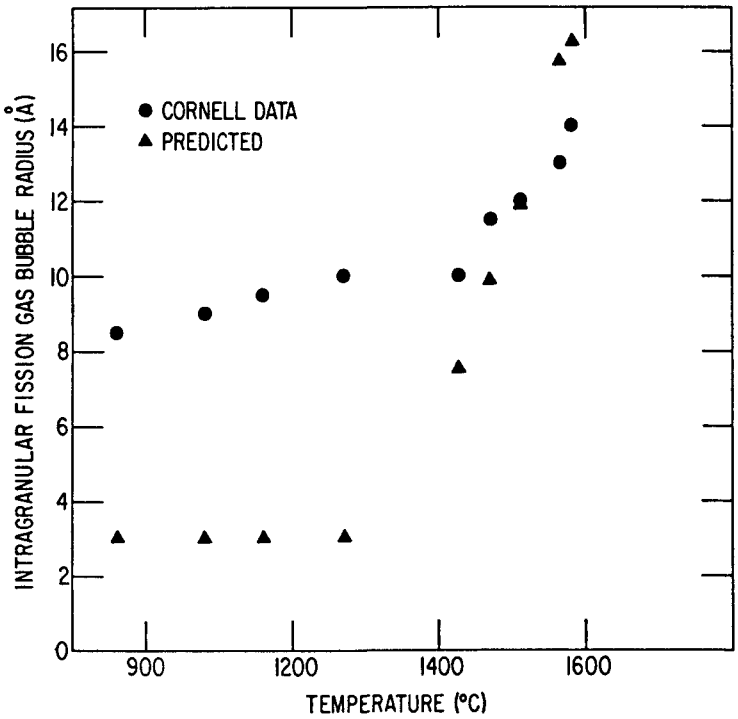

Fig. 14.
Predicted average bubble size, compared with the data of Cornell[60]

measurement occur for the CVTR irradiations. These differences are attributed to uncertainties in power history and to uncertainties in the LIFE calculation of fuel temperatures.

4.5 Average Size of Fission-Gas Bubbles

Figure 14 shows predicted average bubble size compared with the data of Cornell et al.[60] The data of Ref. 60 were obtained from transmission

electron micrographs of thin foils that were prepared from an irradiated UO_2 pellet (which had acquired a burnup of 3.2 x 10^{25} fm^{-3} in 40 days) so that the temperature dependence of the intragranular bubble size could be determined. Intragranular bubbles were observed in material where the estimated irradiation temperature was in the 860–1580°C range. Figure 14 shows that theory underpredicts the bubble size measured by Cornell[60] for fuel temperatures below ~1400°C. For temperatures greater than ~1400*C, the predicted average bubble sizes agree reasonably well with the experimental observations. The discrepancy between the predicted (average) and measured bubble size for fuel temperatures below ~1400°C could result from a discrepancy between the measured bubble diameters and the actual average size of the distribution, owing to the presence of small bubbles below the limit of experimental resolution.

4.6 Retained Fission Gas

Figure 15 shows predicted total retained fission gas at 3 and 12 at.% burnup as a function of UO_2 irradiation temperature, compared with the unrestrained data of Zimmermann.[56] Zimmerman's data in Fig. 15 are for burnups greater than 3 at.% and presumably include the entire burnup range covered by the experiments. The predicted values of total retained fission gas agree reasonably well with the data. As shown in Fig. 15, above 3% burnup and at temperatures of ≈1600K and higher, burnup exerts no influence on the retained–gas concentration. In addition, the amount of retained gas decreases as the irradiation temperature increases; at low temperatures, fission–gas retention is relatively high.

To evaluate the retained fission gas, Zimmermann[56] ground the irradiated fuel in a ball mill to particle sizes noticeably smaller than 1 μm. The fission gas released during the grinding is called "gas in pores." Zimmermann[56] states that this gas originates from intragranular pores and bubbles with diameters down to 10 nm and from gas that was retained on the grain boundaries. After grinding, the powdered fuel was dissolved in nitric acid. The fission gas released during the dissolution process was in solution within the fuel matrix or in very small intragranular bubbles, and is thus called "gas in the matrix."

Figure 16 shows predicted retained fission gas in the matrix at 3 and 12 at.% burnup as a function of irradiation temperature, compared with the

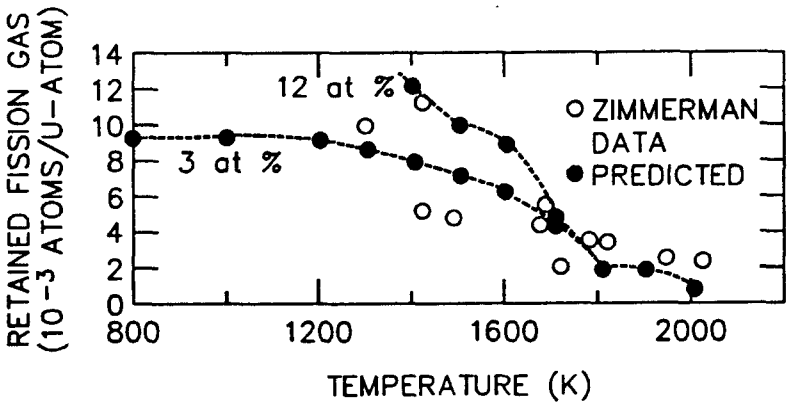

Fig. 15. Predicted retained fission gas at 3 and 12 at.% burnup, compared with the data of Zimmermann[56] at burnups above 3%

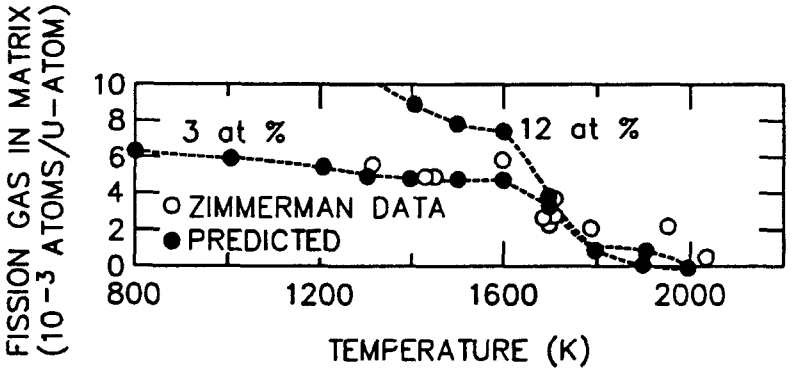

Fig. 16. Predicted retained fission gas in matrix at 3 and 12 at.% burnup, compared with the data of Zimmermann[56] at burnups above 3%

data of Zimmermann[56] for burnups greater than 3%. Again, the agreement between theory and experiment is quite good.

Figure 17 shows predicted retained gas in pores at 3 and 12 at.% burnup as a function of irradiation temperature, compared with the data of Zimmermann[56] for burnups greater than 3%. In contrast to the reasonable agreement between theory and experiment for the total retained gas and the gas retained in the matrix (Figs. 15 and 16, respectively), the results for the fission gas retained in pores are consistently below the average of the measured values. The reason for this discrepancy is not clear in that the retained gas in pores plus the retained gas in the matrix should equal the

total retained gas (as in the predicted results). Note that Zimmermann's[56] data do not, in general, obey this sum rule. Given that the predicted results for the total retained gas and the gas retained in the matrix are in reasonable agreement with the data (Figs. 15 and 16), the predicted results for fission gas retained in pores should agree with a consistent set of data obtained for these conditions.

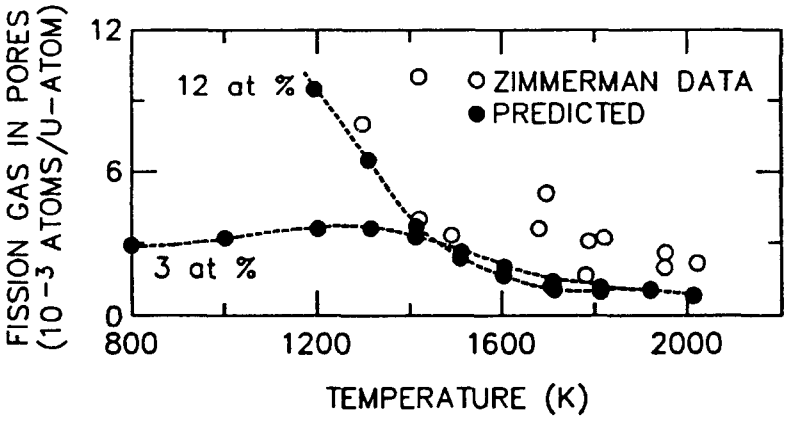

Fig. 17. Predicted retained fission gas in pores at 3 and 12 at.% burnup, compared with the data of Zimmermann[56] at burnups above 3%

4.7 Fission–Gas Swelling

Figures 18 and 19 show predicted rates of swelling due to retained fission gas as a function of irradiation temperature, compared with the results obtained by Zimmermann,[61] for UO_2 fuel irradiated over the burnup ranges of 0–1, 1–2, 2–3, 3–4, and 4–5 at.%. Zimmermann[61] obtained the swelling results shown in Figs. 18 and 19 by comparing the external volume changes of the UO_2 with calculated values for UO_2 densification (i.e., irradiation–enhanced sintering of oxide fuel). In general, the predicted swelling rates obtained with FASTGRASS agree reasonably well with the results obtained by Zimmermann.[61]

Figure 18 shows a very strong temperature dependence of the swelling rate at low burnups. However, with increasing burnup (Fig. 19), the swelling rate and the temperature dependence diminish, owing to saturation of the fission–gas swelling rate caused by the enhanced release of fission gas at increased values of fuel burnup (see Fig.12).

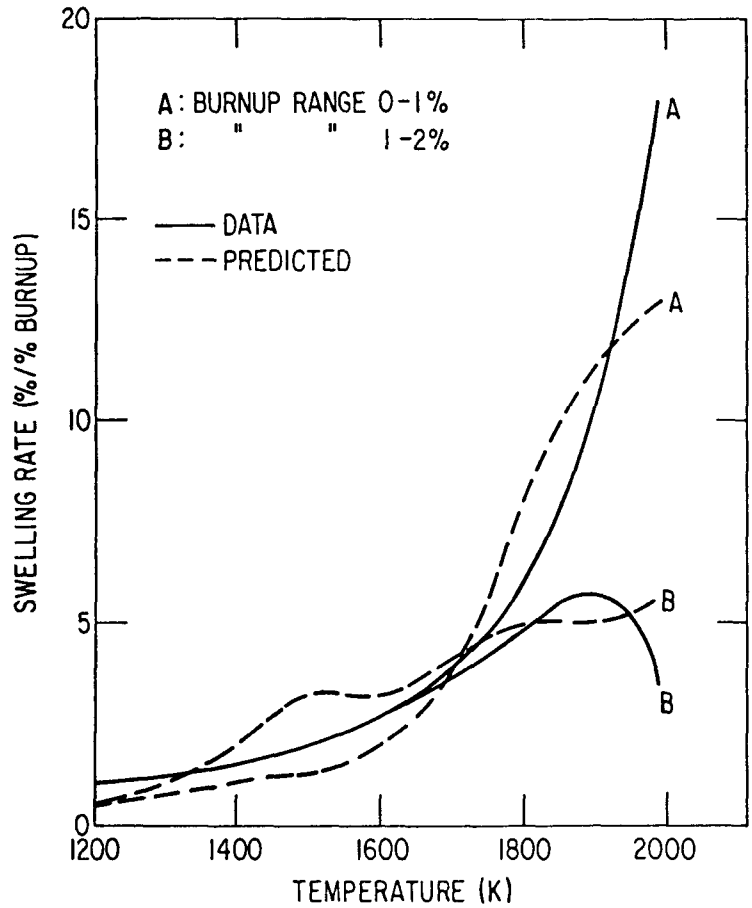

Fig. 18. Predicted swelling rates as a function of fuel temperature, compared with the data of Zimmermann,[61] for burnups of 0–1% and 1–2%

4.8 Microcracking during Transient Conditions

The ability to determine whether microcracking will occur during a given thermal transient is an important element in the prediction of fuel temperatures and fission-product release.[7,8] Microcracking can reduce the thermal conductivity, F_c, of UO_2 to ~50% of the F_c value in dense fuel.[62,63] A change of this magnitude will have a strong effect on calculated temperature profiles. As an example, calculations of the centerline temperature of fuel that had undergone a thermal transient induced by a direct electrical heating (DEH) technique[61,62] vary by as much as 600 K, depending on whether or not microcracking is considered.

As a first-cut approach to modeling ductile-brittle behavior of oxide fuels, a model based on the work of DiMelfi and Deitrich[63] has been

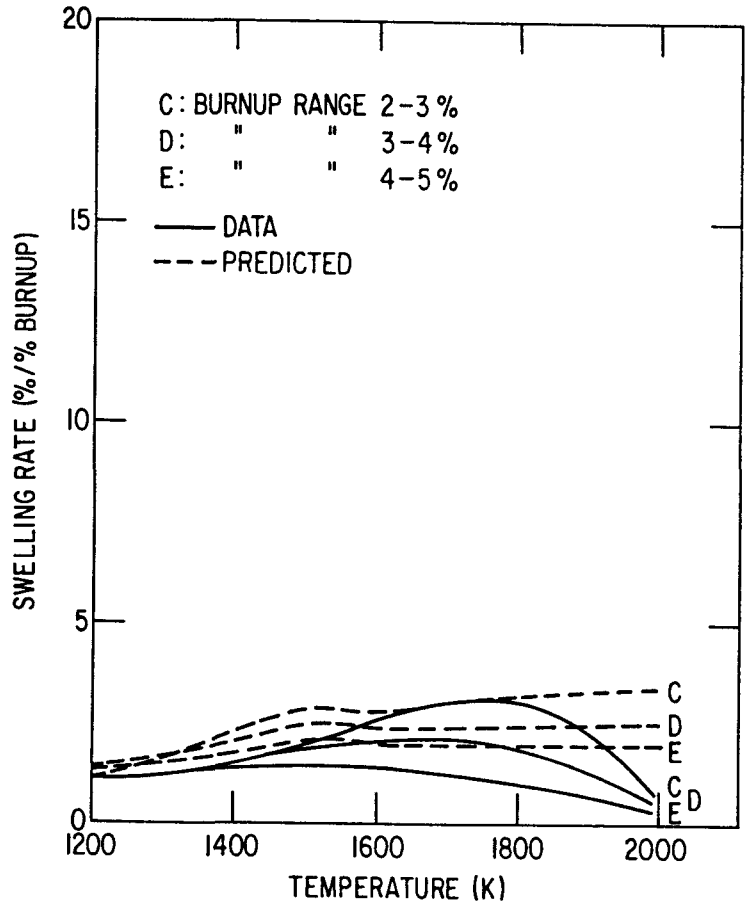

Fig. 19. Predicted swelling rates as a function of fuel temperature, compared with the data of Zimmermann,[61] for burnups of 2–3%, 3–4%, and 4–5%

incorporated into FASTGRASS (see Appendix A). This model estimates the growth rate of a grain boundary bubble under the driving force of internal pressurization. The volume growth rates due to crack propagation and to diffusional processes are compared to determine the dominant mode of volume swelling. Knowledge of the mechanical properties of UO_2 is not required.

The FASTGRASS model was executed with a fuel behavior code[59] for the steady-state irradiation of a fuel rod in the HBR reactor to generate the required initial conditions for transient analysis. The HBR fuel had average heat-generation rates of 22.4 and 17.7 kW/m in the first and second cycles, respectively, and reached a maximum burnup of 3.14 at.%. Subsequently, FASTGRASS was executed with a transient-temperature code[61,62] for a series of DEH tests. The calculational scenario is as follows (see Fig. 20).

Based on DEH-test operating conditions, the radial transient-temperature profile is calculated and subsequently used for the calculation of the fission-gas response. In turn, the fission-gas behavior results are used for the calculation of fuel microcracking. If microcracking occurs, the fission-gas release, retention, and swelling results are updated accordingly. Finally, the microcracking results are passed back to the transient-temperature calculation, where the thermal conductivity expression is modified, and the calculation proceeds to the next time-step.

Figures 21-23 show the predicted pore-solid surface area per unit volume, S_V, as a function of pellet radius for DEH Tests 22 and 32, 34 and 29, and 33 and 37, respectively, and measured values[11] of S_V for the same tests (the measured pore-solid surface is assumed to be produced mainly by fuel microcracking).

In general, considering the complex synergistic nature of the phenomena and the relatively wide range of test conditions, the predicted results agree remarkably well with the data. For example, there is reasonably good agreement between theory and data for both Tests 33 and 37, which had heating rates of 22 and 234 k/s, respectively (Fig. 23). The greatest discrepancy between the predictions and experiments occurs for

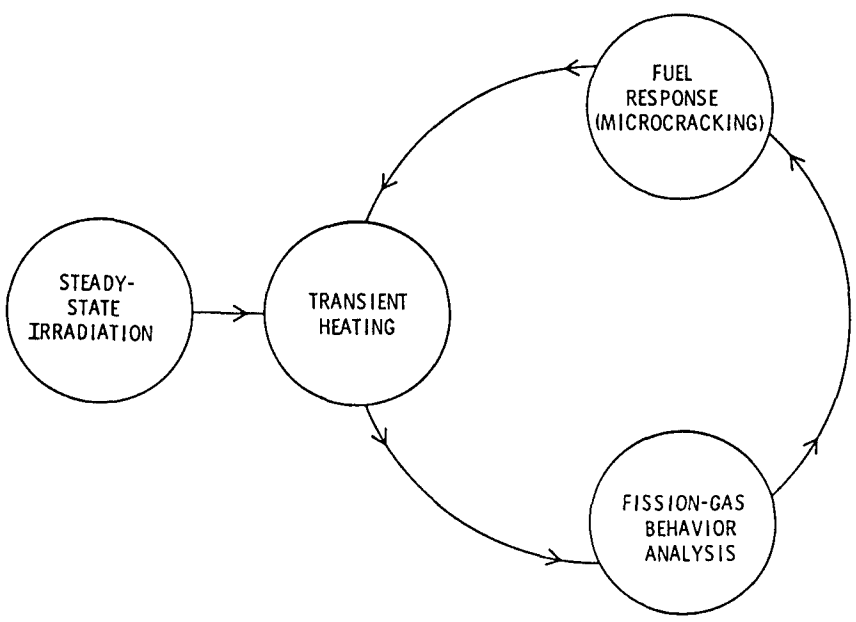

Fig. 20. Interrelationship between fuel fracturing (microcracking), temperature scenario, and fission-gas-bubble response

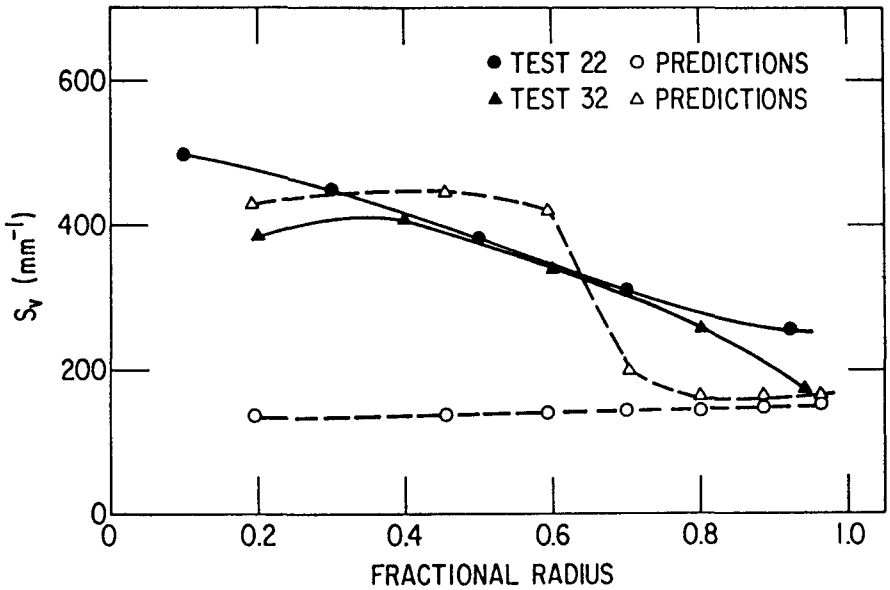

Fig. 21. Predictions of pore–solid surface area, S_v, as a function of pellet radius for Tests 22 and 32, compared with the data of Gehl[62]

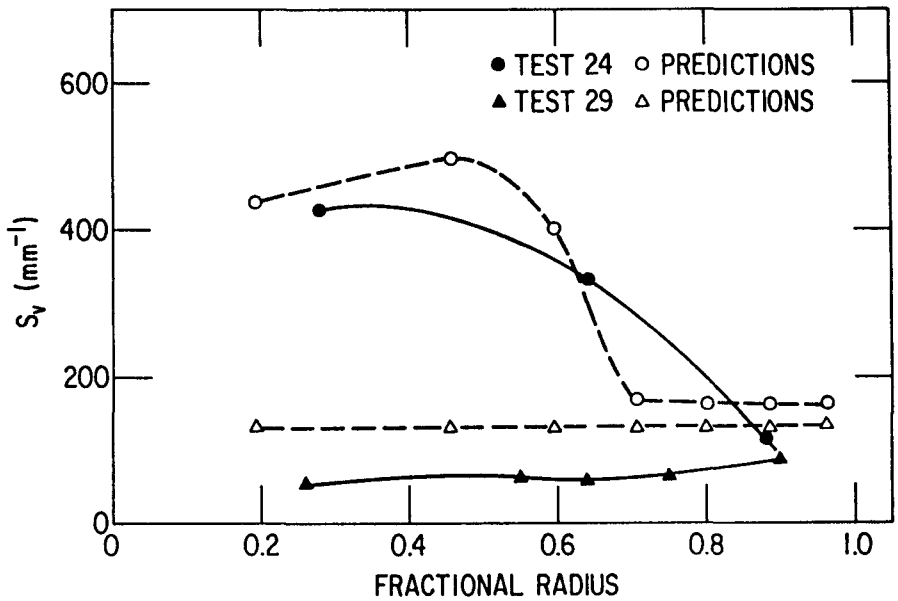

Fig. 22. Predictions of pore–solid surface area, S_v, as a function of pellet radius for Tests 24 and 29, compared with the data of Gehl[62]

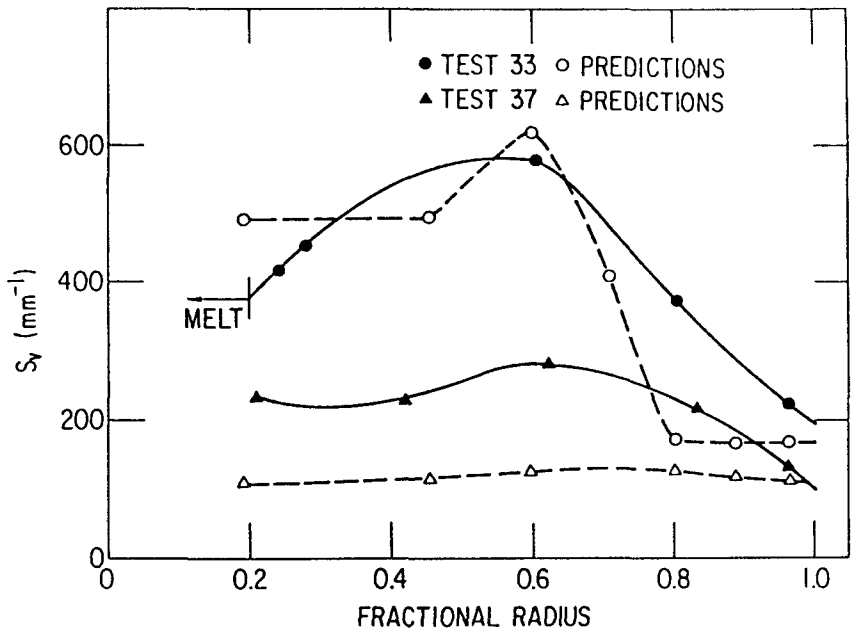

Fig. 23. Predictions of pore–solid surface area, S_v, as a function of pellet radius for Tests 33 and 37, compared with the data of Gehl[62]

Test 22 (Fig. 21), where the theory underpredicts the data obtained near the center of the pellet by more than a factor of two. The implication of this underprediction of fuel microcracking is that the calculated fuel temperatures will be low, with a resultant underprediction of fission-product release (see Fig. 20). This scenario will be addressed further in the following section.

4.9 Transient Fission–Gas Release

Figure 24 shows the predictions for transient fission–gas release for ten transient DEH tests on irradiated UO_2 fuel. Nine tests were on fuel irradiated in the HBR reactor and one test was on fuel irradiated under relatively high–power, load–following conditions in the Saxton reactor.[61]

Except for Test 22 (12% gas release measured), the predictions are in reasonable agreement with the measured values. There appears to be relatively uniform scatter of the predicted vs. the measured values on either side of the diagonal line, indicating random, rather than biased, uncertainties. Random uncertainties are most likely associated with the calculation of fuel temperatures. The complex synergism among radial heat

flux, fuel microcracking, and fission-gas response has already been discussed in Section 4.8 above (see Fig. 20). In addition, the actual transient-temperature profiles for the DEH tests contain asymmetries due to nonuniform heating associated with the inhomogeneity of the DEH test pellets. These asymmetries have not been quantified and were not included in the analysis of the DEH tests.

FASTGRASS predicts that 2.3% gas release occurred during DEH Test 22, compared to the measured value of 13.1% (Fig. 24). As discussed in Section 4.8 above, and shown in Fig. 21, the theory also underpredicts (by more than a factor of two near the pellet center) the amount of pore/solid surface area generated during DEH Test 22 by fuel microcracking. Based on the discussion of the synergism involved in the determination of radial heat flux (represented pictorially in Fig. 20), this underprediction of fuel microcracking should lead to underprediction of fuel temperatures and, hence, to an underprediction of fission-gas release. Because relatively reasonable predictions for fuel microcracking were made for the other DEH tests (Figs. 21-23), the predictions for fuel temperatures and fission-gas release in those tests should also be reasonable (if the fission-gas response theory is accurate). Indeed, they are, as demonstrated in Fig. 24.

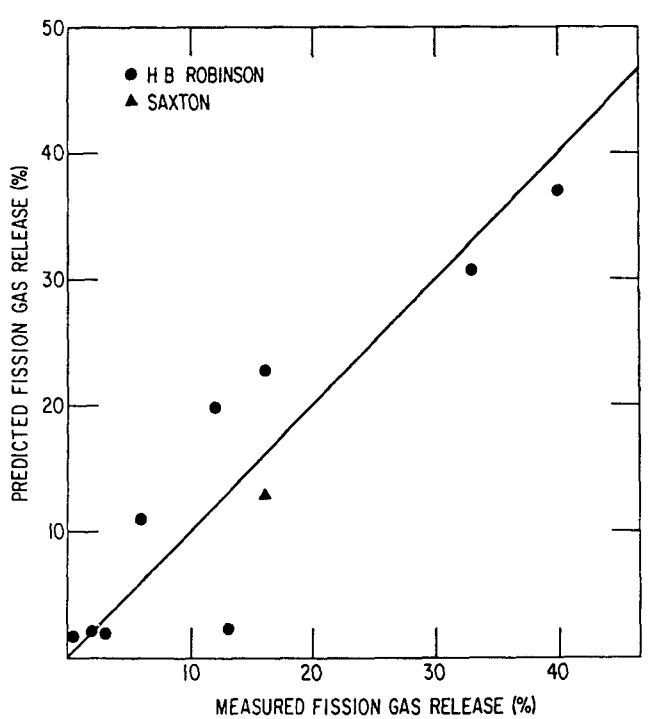

Fig. 24.
Predictions of the theory of transient gas release vs. experimentally measured values from ten DEH tests. The diagonal line indicates perfect agreement between prediction and observation.

5 FASTGRASS Theory of Fission–Product Behavior in Solid Fuel: UO_2/Fission–Product Chemistry

The FASTGRASS model for reactive VFP and AEFP release is based on two major assumptions: 1. because the VFPs and AEFPs are known to react with other elements to form compounds, a realistic description of VFP/AEFP release must include the effects of chemistry on behavior, and 2. because the noble gases have been shown to play a major role in establishing the interconnection of escape routes from the interior to the exterior of the fuel, a realistic description of VFP/AEFP release must include, a priori, a realistic description of fission–gas release and swelling. The physical reasonableness of these assumptions has been supported, thus far, by good agreement between model predictions and actual observation. FASTGRASS treats only stable fission products, i.e., no provisions have been included for radiolytic decay. A special version of FASTGRASS has been utilized to assess the behavior of short–lived fission products.[2]

Based on the work of Tam et al.,[64] the following system of equations is used to assess Cs and I sequestering behavior in UO_2 fuel:

$$2Cs(g) + UO_2(c) + O_2(g) \rightarrow Cs_2UO_4(c), \tag{60}$$

$$2Cs(g) + Mo(c) + 2O_2(g) \rightarrow Cs_2MoO_4(c), \tag{61}$$

$$Cs(g) + I(g) = CsI(c), \tag{62}$$

where g and c designate gas and condensed phases, respectively.

Tellurium (Te) is considered non–reactive within the fuel matrix. The physical basis for the primary reactions governing the chemical behavior of I and Cs in UO_2–based fuel is reasonably well established and documented in the literature.[64–66] However, the internal fuel rod chemistry governing Ba and Sr release is less certain and no mechanistic model exists at this time for the estimation of the release behavior of these elements from severely damaged fuel. Rather, the release of these fission products is based solely on empirical correlations obtained from a limited data base. Here we postulate a basis for estimating such Ba and Sr release.

Barium and Sr belong to the Group II (alkaline earth) elements. As discussed in Ref. 67, evidence indicates that Ba and Sr may be present in

the fuel as simple oxides, uranates, molybdates, or zirconates. The simple oxides and the molybdates would be the most stable of these compounds; compounds formed with Sr tend to be more stable than the corresponding Ba compounds. In general, the formation of such compounds can be expected to immobilize Ba and Sr within the fuel matrix, and thus limit their release potential. Therefore, of particular interest with respect to release modeling is the establishment of a basis for estimating the amount of Ba and Sr that remains in the more mobile elemental atomic form, versus the quantities of these fission products that react to form less volatile species.

A qualitative guide to the chemical state of fission-product Ba and Sr in oxide fuel is their affinity for oxygen. The stability of fission-product Ba and Sr, as elements or as oxides in the presence of UO_2, depends on the difference between the free energy of the fission-product oxide and the fuel oxygen potential. For fission-product compounds with free energies below that of the fuel oxygen potential, an oxide is predicted; for compounds with free energies above that of the fuel oxygen potential, a stable element is predicted. Comparison of the O potential of stoichiometric UO_2 fuel with the free energies of formation of Ba and Sr fission-product oxides clearly indicates that Ba and Sr have a high propensity to form oxides. Stoichiometry also plays an important role: hyperstoichiometric fuel tends to show an enhanced potential for the formation of fission-product oxides.

The Ba and Sr reactions of interest are as follows:

Barium	Strontium
$Ba + 1/2\ O_2 \rightarrow BaO$	$Sr + 1/2\ O_2 \rightarrow SrO$
$Ba + Zr + 3/2\ O_2 \rightarrow BaZrO_3$	$Sr + Mo + 2\ O_2 \rightarrow SrO$
$BaO + Mo + 3/2\ O_2 \rightarrow BaMoO_4$	$SrO + UO_2 + 1/2\ O_2 \rightarrow SrUO_4$
$BaO + UO2 + 1/2\ O2 \rightarrow BaUO_4$	

The alkaline earths also exhibit the potential to form iodides. However, because high-yield Cs has a higher free energy of formation with I than do Ba and Sr, the potential for CsI formation is greater, and tends to limit the formation of Ba and Sr iodides. Thus, for all practical purposes, the above reactions can be expected to control the internal fuel rod chemistry of Ba and Sr. The free energies of formation, ΔG, for some of the above reactions, and for several relevant Cs reactions, are presented in Table 7; they are based upon values suggested in Ref. 68.

Table 7. Free Energy of Formation of Ba and Sr Fission Product Oxides

Reactants[a]	Product	Free Energy, ΔG (cal/mol product)	Temperature (K)
Barium			
Ba(c) + 1/2 O_2(g)	BAO(c)	−117713 + 16.7T	298–983
Ba(l) + 1/2 O_2(g)	BAO(c)	−133186 + 24.56T[b]	983–2122
Ba(c) + 1/2 O_2(g)	BaO(g)	−31367 − 12.95T	298–983
Ba(l) + 1/2 O_2(g)	BaO(g)	−38373 − 6.76T	983–2268
BaO(c)	BaO(g)	98138 − 33.21T	–
Ba(c) + U(c) + 2O_2(g)	$BaUO_4$(c)	−473010 + 87.3T	298–1403
UO_2(c) + BaO(c) + 1/2 O_2	$BaUO_4$(c)	−81517 + 22.32T	–
Strontium			
SrO(c)	SrO(g)	135344 − 36.42T	298–2938
Sr(c) + 1/2 O_2(g)	SrO(c)	−141156 + 22.92T	298–1041
Sr(l) + 1/2 O_2(g)	SrO(c)	−142835 + 24.55T	1041–1654
Sr(g) + 1/2 O_2(g)	SrO(c)	−174079 + 43.44T	1654–2938
Cesium			
Cs(g) + I(g)	CsI(s)	−73041 + 15.81T	–
2Cs(g) + UO_2(c) + O_2(g)	Cs_2UO_4(c)	−233152 + 91.62T	–
2Cs(g) + Mo(c) + 2O_2(g)	Cs_2MoO_4(g)	−325372 + 86.52T[c]	952–2892

[a]c, g, and l designate crystalline, gas, and liquid phases, respectively.
[b]The value of ΔG listed in Ref. 68 is incorrect.
[c]The value of ΔG listed in this analysis is ΔG = −297715 + 79.166T.

In addition to the formation of oxides, uranates, molybdates, and zirconates, which can be expected to be dispersed throughout the fuel matrix, evidence supports the possibility that Ba and Sr aggregate into inclusions that effectively form a separate phase within fuel (i.e., physical and chemical properties determined by inclusion composition rather than

fuel properties). However, the consensus among various researchers is that, in normally irradiated fuel, both Ba and Sr exist primarily in the fuel matrix in oxide form and not as a prime constituent of metallic inclusions. Because of uncertainties in composition, oxidation state, homogeneity, and the indication that Ba and Sr are not major inclusion constituents, holdup of these elements via metallic inclusion sequestering will not be considered in this analysis. Indeed, one would expect that inclusions containing Ba and Sr would be primarily of the oxide form rather than metallic.

Equilibrium fission–product distributions for the various phases of the fuel/fission–product system at 1500 K have been calculated.[67,68] The calculations are based on UO_2 fuel at 2 at. % burnup, an O–to–U ratio that is slightly hyperstoichiometric, and a 10% void volume in the fuel. Such an equilibrium distribution may not be achieved at 1500 K in a transient sequence, because release of the fission products to voids and bubbles may be too slow. Moreover, the estimates of solutions of fission–product oxides in urania are based on sparse data. In spite of these limitations, thermochemical equilibrium calculations indicate that the most probable distribution of Ba and Sr in the UO_2 is as follows:

Barium Partitioning in UO_2 (%)		Strontium Partitioning in UO_2 (%)	
BaO	59	SrO	96
$BaUO_4$	35	$SrMoO_4$	4
$BaMoO_4$	4		
$BaZrO_4$	2		

In view of the thermochemical conditions in fissioned UO_2 fuel discussed above, FASTGRASS assumes that the following reactions dominate Sr and Ba sequestering effects within the UO_2 matrix:

$$Sr(s) + 1/2\ O_2(g) = SrO(c) \tag{63}$$

$$SrO(c) = SrO(g) \tag{64}$$

$$Ba(s) + 1/2\ O_2(g) = BaO(c) \tag{65}$$

$$BaO(c) = BaO(g) \tag{66}$$

$$UO_2(c) + BaO(c) = 1/2\ O_2(g) = BaUO_4(c) \tag{67}$$

where s represents atoms in solution, and c and g represent crystalline and gas phases, respectively.

For the Sr and Ba reactions, the concentration of nine chemical species [Sr, SrO(c), SrO(g), O_2, Ba, BaO(c), BaO(g), $BaUO_4$(c), and UO_2] must be determined to specify the fraction of fission–product Sr and Ba that is available for release from the fuel matrix either in atomic form, or as an oxide. Six additional chemical species result from the I and Cs reactions (I, Cs, CsI, Cs_2UO_4, Cs_2MoO_4, and Mo). From the law of mass balance, the total fractional atom concentration of Sr, Ba, Cs, I, and Mo equals the sum of their respective fission yields, i.e.,

$$C_{Sr}^{T} = C_{Sr} + C_{SrO(c)} + C_{SrO(g)} = 0.0926\ \mathrm{BU}, \tag{68}$$

$$C_{Ba}^{T} = C_{Ba} + C_{BaO(g)} + C_{BaO(g)} + C_{BaUO_4} = 0.0682\ \mathrm{BU}, \tag{69}$$

$$C_{Cs}^{T} = C_{Cs} + C_{CsI} + 2C_{Cs_2UO_4} + 2C_{Cs_2M_oO_4} = 0.1882\ \mathrm{BU}, \tag{70}$$

$$C_{I}^{T} = C_{I} + C_{CsI} = 0.011\ \mathrm{BU}, \tag{71}$$

$$C_{Mo}^{T} = C_{Mo} + C_{Cs_2MoO_4} = 0.2348\ \mathrm{BU}, \tag{72}$$

where C_i^T= total fractional concentration of species i (e.g., Sr, Ba) generated as a function of fractional burnup, BU, and C_i = fractional concentration of the individual chemical forms of species i. The concentrations of O_2 and UO_2 can be assessed from standard models as a function of temperature, O/U ratio, burnup, and fuel density; thus, seven of the fifteen concentrations are known. The eight remaining equations can be obtained from the law of mass action. For the reaction(s) Sr + 1/2 O_2(g) = SrO(c), Eq. 63, the equilibrium constant, K_1, can be expressed in terms of the free energy of formation, ΔG, and the concentration of the reactants and products, i.e.,

$$K_1 = \exp\frac{-\Delta G_1}{RT} = \frac{a_{SrO(c)}}{C_{Sr}P_{O_2}^{1/2}}, \tag{73}$$

where ΔG_1 is obtained from Table 7, P_{O_2} is the oxygen partial pressure, and $a_{SrO(c)}$ is the activity of SrO(c). For the reaction Ba(s) + 1/2 O_2(g) = BaO(c), Eq. 65, the equilibrium constant, K_2, can be similarly expressed as

$$K_2 = \exp\frac{-\Delta G_2}{RT} = \frac{a_{BaO(c)}}{C_{Ba}P_{O_2}^{1/2}}. \tag{74}$$

The remaining six equations, [Eqs. 60–62, 64, 66, and 67] can be expressed in terms of the corresponding free energies of formation and concentrations of the reactants and products in a similar manner.

To utilize the free energies given in Table 7 for the reactions described by Eqs. 63 and 65, one must know the corresponding solution energies for Ba and Sr. The values used in this analysis for Ba and Sr are 46,700 and 33,000 cal/mol, respectively.

The activities of the various reaction products in a condensed phase can be written as an activity coefficient times the concentration of the reaction product [e.g., $a_{BaO(c)} = \alpha_{BaO(c)}C_{BaO(c)}$]. It is assumed that all the condensed–phase Ba, Sr, and Cs reaction products are distributed uniformly within the UO_2 matrix so that $\alpha_i = 1$, where i denotes the particular reaction product.

Following the analysis of CsI formation in UO_2 given by Cronenberg and Osetek,[69–70] it is assumed that the formation of the reaction products, CsI(g), SrO(g), and BaO(g), requires the presence of reaction sites, which are primarily microbubbles containing the noble fission gases Xe and Kr.

The activities of the gas–phase reaction products, i.e., CsI(g), BaO(g), and SrO(g), are equal to their corresponding partial pressures, P_{CsI}, P_{BaO}, and P_{SrO}. Once these partial pressures have been calculated, they can be used in conjunction with an equation of state of the Van der Waals form,

$$P(V - BN) = NkT,$$

where B is the Van der Waals constant, V is the bubble volume, and n is the number of atoms of CsI(g), SrO(g), or BaO(g) in the bubble in atoms/cm^3, to calculate the quantity of CsI(g), SrO(g), and BaO(g) in the material. Because

the bubble volume, V, is calculated directly in FASTGRASS, no remaining unknowns are present in this calculation.

The oxygen partial pressure is calculated according to the analysis of Blackburn and Johnson,[68] and is given by the following expression:

$$P_{O_2}^{1/2} \doteq \frac{(\phi-2)+\left[(\phi-2)^2+4B(3-\phi)(\phi-1)A\right]^{1/2}}{2B(3-\phi)/\phi}, \tag{75}$$

where A = exp(78300/T − 13.6), B = exp(16500/T − 5.1), and ϕ = O/U.

The value of ϕ can be calculated by taking into account the fissioning of ^{235}U and the formation of the oxides and uranates given in Eqs. 60–72, i.e.,

$$\phi = \phi_o + \frac{Kt}{N_m^o}(\phi_o - \alpha) - \alpha, \tag{76}$$

where $\alpha = C_{SrO(c)} + C_{Sr)(g)} + C_{BaO(c)} + C_{BaO(g)} + C_{BaUO_4} + 2C_{Cs_2UO_4} + 4C_{Cs_2MoO_4}$, N_m^o is the initial number of heavy–metal atoms, t is the irradiation time, and ϕ_o is the starting O/U ratio. In general, because f and T are functions of time, Eq. 76 is phrased in differential form and integrated over time.

Simultaneous solution of this coupled system of equations, Eqs. 60–72, 75, and 76, yields equilibrium concentration as a function of fuel burnup and temperature. The amount of Sr and Ba that is predicted to be retained in the fuel in atomic form, or in the vapor phase in microbubbles is assumed available for release, whereas all other species are assumed to be immobilized within the fuel microstructure.

Once the fractions of atomic Sr and Ba are known, their mobility through the fuel microstructure is assessed. CsI(g), BaO(g), and SrO(g) are assumed to migrate within fission–gas bubbles. The migration of atomic I, Cs, Ba, and Sr is handled in a fashion analogous to that of the noble gases; the concentrations of these species within the grains and on the grain boundaries are described with equations of the form shown by Eq. 1. Cs, I, Sr, and Ba gas atom diffusivities are taken to be the same as that of Xe. The

specific variables associated with these equations are defined in Table 2. These calculations for fission-product chemistry and migration are performed sequentially, as a function of time. This method of calculating VFP/AEFP behavior is reasonable as long as the chosen integration time-steps are small enough so that a quasichemical equilibrium is maintained.

6 FASTGRASS Theory of Gas Bubble Behavior in Degraded Fuel

A wide range of material interaction and phase transformation phenomena can be expected at the elevated temperatures associated with severe core-damage accidents; one of the more significant is the steam-cladding (of Zircaloy) reaction, with ZrO_2 and oxygen-stabilized alpha-Zircaloy [α-Zr(O)] byproducts.

6.1 Effect of Fuel Liquefaction

Figure 25 presents the pseudobinary equilibrium diagram for UO_2 and oxygen-saturated α-Zr(O). As indicated, oxygen-saturated α-Zr(O) will dissolve UO_2 if the two are in contact at temperatures in excess of ≈2170 K. A eutectic melt is formed with a 5% mole fraction of UO_2, whereas, at higher UO_2 compositions, there exists a mixture of liquid with a $(U\text{-}Zr)O_2$ solid component that is analogous to a slush. A mixture of two liquids (i.e., $L_1 + L_2$) occurs at temperatures above ≈2673 K, when the UO_2 mole composition is between ≈23% and 85%.

Such parameters as fuel pellet microcracking, oxidation state, wetting characteristics, and time at temperature also exert a profound influence on the dissolution process. Until the influence of such parameters can be established from a systematic data base, modeling of dissolution effects on fission-product release must, of necessity, rely primarily on empirical evidence. For present purposes, two limiting conditions on fuel dissolution will be considered: *grain boundary dissolution (2673 K > T > 2170 K)*, where limited attack of molten α-Zr(O) on the fuel microstructure results in a residual U-rich melt phase at grain boundaries, which effectively acts as a melt pathway for the escape of fission products to the pellet surface; and *fuel matrix dissolution (>2673 K)*, where more extensive attack of molten α-Zr(O) on the fuel microstructure results in dissolution of the entire grain structure over a portion of the fuel pellet radius so that fission-product

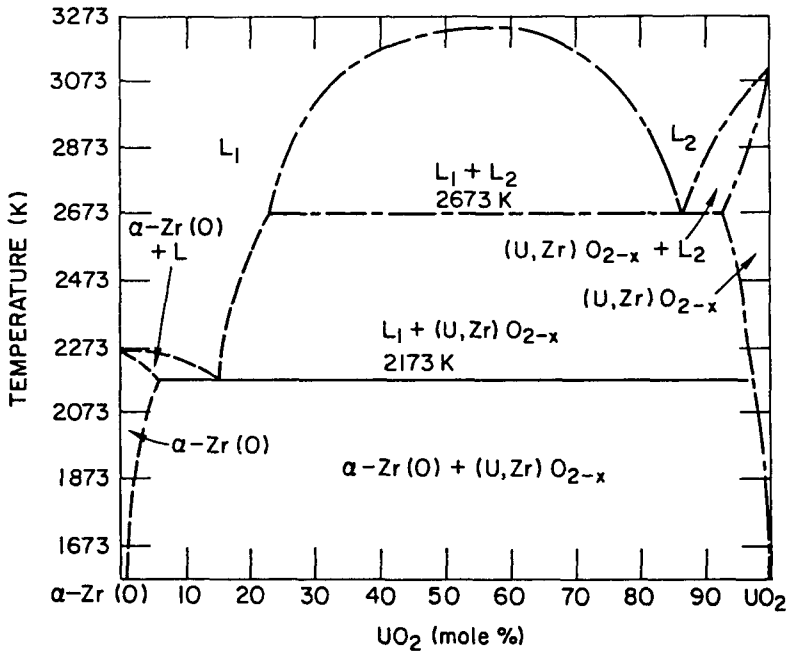

Fig. 25. Equilibrium pseudobinary phase diagram between UO_2 and oxygen-saturated α-Zr(O)

transport is controlled by microbubble and atomic diffusion in a sea of liquefied fuel.

Models describing fission-gas release behavior for these two limiting conditions have been developed and incorporated into FASTGRASS. For grain-boundary-type dissolution, release of fission products occurs primarily by fission-product migration through the liquefied U, or U-Zr lamina (or film), to the fuel surface. For fuel-matrix-type conditions, release occurs by fission-product migration through the bulk melt to a free surface. Gas bubble mobility in the U/U-Zr melt can occur via bubble rise in a viscous liquid, evaporation/condensation, and volume diffusion, where the dominant mechanism is primarily dictated by bubble size.

6.2 Effect of Fuel Dissolution

For relatively large bubbles (see Fig. 26) in the absence of a strong temperature gradient, escape will be dominated by macroscopic forces, i.e., buoyancy effects, through the liquefied lamina, to the surface of the fuel (the lamina is assumed to be 1-2 μm thick and exist along the liquefied grain

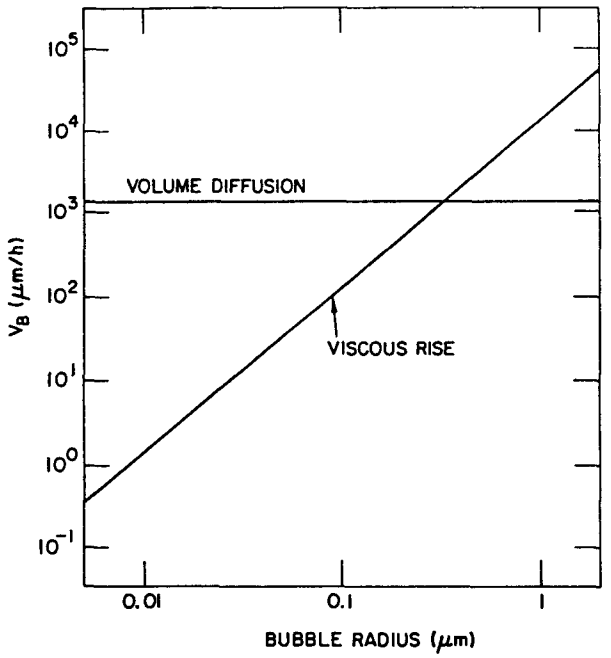

Fig. 26.
Size dependence of bubble velocities in liquid UO_2 in a temperature gradient of 100 K/cm at 2200 K

boundaries). This is in contrast to release processes in solid fuel, where release can occur directly upon the arrival of fission gas at the grain edges, if a stable network of interconnected porosity is encountered.

Modeling of bubble rise in a viscous liquid is based on an estimate of the time that is necessary for a pore to rise from the interior of the melt to the free surface. An approximation of the bubble velocity can be obtained by assuming that bubble interference during an increment of time is negligible and variations in properties along the distance of travel are minimal. Under such assumptions, the classical expression for bubble rise in a viscous liquid can be employed. If a submerged, rigid bubble is allowed to rise from rest in the liquid, it will accelerate until it reaches a constant terminal velocity, V_b. In this situation, the effects of gravity, F_g, and drag, F_d, are just balanced by the effects of buoyancy, F_b; $F_b = F_g + F_d$, i.e., the balance of the equilibrium force for such steady-state bubble rise can be written as

$$\frac{4}{3}\pi R_b^3 \rho_L g = \frac{4}{3}\pi R_b^3 \rho_g g + 6\pi R_b \mu_L V_b, \tag{77}$$

where R_b is the bubble radius, ρ_L is the liquid fuel density, g is the gravitational constant, ρ_g is the gas density in the bubble and μ_L is the viscosity of liquefied fuel.

Noting that $\rho_L >> \rho_g$, one can express the terminal rise velocity as

$$V_{b,t} = \frac{2R_b^2 \rho_L g}{9\mu_L}. \tag{78}$$

Because the liquid lamina can be expected to have a snakelike random structure in a partially dissolved fuel pellet, direct vertical bubble rise is unlikely. Bubble migration is, therefore, viewed as upwardly biased in a snakelike path, so that the effective rise velocity, V_t, is taken to be half (between zero and the terminal velocity) the terminal velocity, i.e., $V_b = 1/2\ V_{b,t}$.

Fission–gas bubbles can also migrate in the liquid by a volume diffusion mechanism. The diffusivity of a bubble of radius R_b, migrating by volume diffusion, is

$$D_b = \frac{3\Omega}{4\pi R_b^3} D_u, \tag{79}$$

where Ω is the molecular volume and D_u is the U–atom diffusivity. The U–atom diffusivity in molten UO_2 is based on the Sutherland–Einstein model and is given by

$$D_u = \frac{kT}{4\pi r_a \mu_L}. \tag{80}$$

The velocity of a bubble moving by a volume diffusion mechanism in the presence of a temperature gradient, ΔT, is expressed by

$$V_b = \frac{D_u Q_v^*}{kT^2} \nabla T, \tag{81}$$

where Q^*_v is the volume diffusion heat of transport.

For larger bubbles in the presence of a relatively large temperature gradient, vapor transport can strongly dominate both buoyancy–driven bubble rise and volume diffusion. For this case, the bubble velocity is given by

$$V_b = \frac{D_v \Omega \alpha P_0 \Delta H_v}{k^2 T^3} \exp\left(-\frac{\Delta H_v}{kT}\right) \frac{3}{2} \nabla T, \tag{82}$$

where Ω is the atomic volume, $P_0 \exp(-\Delta H_v/kT)$ is the equilibrium vapor pressure, ΔH_v is the heat of vaporization for the rate-diffusing species of the fuel, D_v is its diffusivity in the vapor contained in the void, and $\alpha \leq 1$ measures any deviation from equilibrium vapor pressure at the pore surface. D_v is obtained from the kinetic theory of gases and is defined as follows:

$$D_v = \frac{2kT}{3\pi\sigma^2 P}\left[\frac{2kT}{\pi}\left(\frac{1}{m_1} + \frac{1}{m_2}\right)\right]^{1/2}, \tag{83}$$

where $\pi\sigma^2$ is the collision cross section between the diffusing species and the principal component of the gas phase in the void, P is the total gas pressure in the void ($P = 2\gamma/R + P_h$, where P_h = pressure in the surrounding liquid and γ = surface energy), and m_1 and m_2 are the masses of the diffusing species and the principal component of the gas phase, respectively.

Figures 26 and 27 show bubble velocities as a function of bubble radius obtained with Eqs. 78–83 at 2200 and 3125 K. Figures 26 and 27 correspond to temperature gradients of 100 and 5000 K/cm, respectively. The values of the various parameters used in the above equations are listed in Table 8.

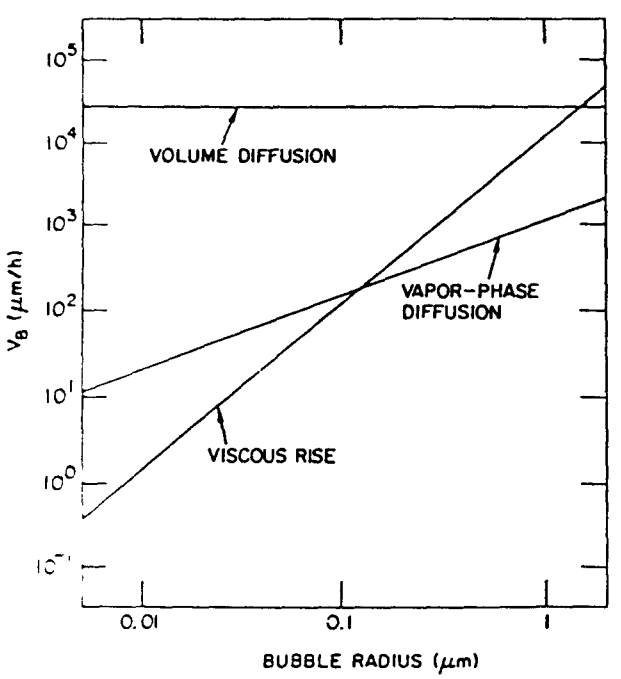

Fig. 27.
Size dependence of bubble velocities in liquid UO_2 in a temperature gradient of 5000 K/cm at 3135 K

Table 8. Values of Various Parameters Used in FASTGRASS

Symbol	Value
ρ_L	$8.72\ g/cm^3$
μ_L	$4 \times 10^{-2}\ g/s^2$
r_a	$1.42 \times 10^{-8} cm$
Q_v	$4.8 \times 10-12$ ergs
P_0	4.16×10^{-4} dynes/cm^2
ΔH_v	1×10^{-11} erg
$m_1(UO_2)$	4.48×10^{-22} g
m_2 (Xe)	2.19×10^{-22} g
D_g	$2.1 \times 10^{-4}\ e^{-91000/RT}\ cm^2/s$
Db[a]	$\frac{1.486 \times 10^{-11} e^{-108000/RT}}{R_b^{2.09}} cm^2/s$
D_e D_f	$R_i \le R_s$: $\frac{3.42 \times 10^6 \Omega^{4/3} e^{-108000/RT}}{\pi R_i^2 \left(R_s^2\right)^2} cm^2/s$
	$R_i > R_s$: $\frac{3.42 \times 10^6 \Omega^{4/3} e^{-108000/RT} \sin\left(\frac{R_s}{2R_i}\right)^2}{\pi R_i^2 R_s^2} cm^2/s$
R_s	1.12×1^{-6} cm
δ	1.12×10^{-4}
λ	5×10^{-7} cm
b_o	$2 \times 10^{-17}\ cm^3$
σ_b	$0.01\ cm^2/cm^3$
σ_e	0.02
γ	$1601.4 - 0.345T\ erg/cm^3$ (solid)
γ_L	$450\ erg/cm^3$ (liquid)
D_u	$2.0\ e^{-64200/T}\ cm^2/s$
$D_{gb}W$	$3.1 \times 10^{-8} e_{-}^{24000/T}\ cm^3/s$

[a]For nonequilibrium conditions, FASTGRASS utilizes a theoretical model for the diffusion of overpressurized fission-gas bubbles, developed by Rest.[7] This model is summarized in Appendix D.

From Fig. 26, it can be seen that, for small bubbles (<1 μm) and small values of the temperature gradient (≈100 K/cm), volume diffusion dominates bubble motion. On the other hand, large bubbles (≥1 μm), in the absence of significant temperature gradients, move primarily under the forces of buoyancy. In liquid UO_2 with temperature gradients ≥ 5000 K/cm (see Fig. 27), bubbles with radii of up to ≈1 μm move primarily by volume diffusion, whereas bubbles with radii greater than 1 μm move primarily by viscous rise.

Bubbles moving in a liquefied medium can coalesce and grow. Because FASTGRASS considers only a single bubble size class per distinct morphological fuel region (i.e., the average-size bubble), the rate of change of the bubble density, C_b, for a bubble of radius R_b, moving by random and biased migration in a liquefied lamina (e.g., a destroyed grain boundary region) is given by [see Eq. 14, and subsequent discussion]

$$\dot{C}_b = -\left(16\pi R_b D_b + \alpha_b \pi R_b{}^2 V_b\right) C_b^2, \tag{84}$$

where α_b is a parameter that incorporates the effects of a distribution of bubble sizes, and V_b is given by either Eq. 78, 81, or 82. The value of $\alpha = 4\pi$ makes the second term on the RHS of Eq. 84 correspond to the product of the bubble density and the interaction volume swept out by each bubble.

For fuel matrix dissolution, FASTGRASS considers the interaction between gas atoms in solution and two distinct bubble size populations: those that had been in the fuel lattice prior to fuel dissolution and those that had been on the grain boundaries or in a liquefied lamina. The coalescence probability for these bubbles is given by

$$P(R_1, R_2) = 2\pi(D_1 + D_2)(R_1 + R_2) + \pi(R_1 + R_2)^2 (V_2 - V_1), \tag{85}$$

where R_1, D_1, V_1 and R_2, D_2, V_2 are the radius, diffusivity, and velocity of bubble size distribution 1 and 2, respectively. Prior to fuel liquefaction/dissolution, the bubbles are assumed to be spherical in the bulk, lenticular on the grain faces, and ellipsoidal on the grain edges. Subsequent to fuel liquefaction/dissolution, all bubbles are assumed to be spherical.

FASTGRASS analyses of the PBF-SFD 1-1 test indicate that liquefaction-induced fission-product release depends on initial coalescence and growth of relatively small (0.04-μm-diameter) bubbles in the liquefied material due

to a volume diffusion mechanism (i.e., the fuel used in SFD 1-1 was trace-irradiated and populated with a distribution of extremely small bubbles before the onset of liquefaction/dissolution, (see Fig. 26). Whereas volume diffusion (i.e., self diffusion of the U^{4+} ion) is relatively slow in solid UO_2, it appears to be a significant factor in the motion of small bubbles in liquefied UO_2. The growth of small bubbles in the liquefied material is predicted to occur mainly by the volume diffusion mechanism until the bubbles reach sufficient size (see Fig. 26). Subsequently, the release of fission gas (and other fission products trapped in the bubbles) is dominated by the motion of relatively large (≈1-μm-diameter) bubbles under buoyant forces.

7 Validation 2: Comparison between Predictions and Data for Fission-Product Release during Severe-Accident Conditions

FASTGRASS predictions of fission-product release behavior have been compared with three sets of data: 1. the data obtained by Parker and Barton,[42] based on out-of-reactor induction heating experiments on declad, crushed low-burnup (1000) fuel; 2. data from high-temperature, in-cell heating tests on irradiated high-burnup LWR fuel in a flowing stream atmosphere, performed at ORNL;[41] and (3) data from the in-reactor PBF-SFD Tests,[26] in which 1-m-long, trace-irradiated (89 MWd/t) and normally irradiated (35000 MWd/t) fuel rods were tested under accident conditions.

7.1 Comparison with Out-of-Reactor Data

7.1.1 Data of Parker and Barton

In Table 9, the data of Parker and Barton[42] are compared with FASTGRASS predictions of Xe, Ba, and Sr release at four fuel temperatures and two values of fuel burnup. Parker and Barton[42] heated irradiated UO_2 specimens for ≈5.5 h in an inert environment. Because fuel fragments with unknown values of open pore/solid surface area were used in most of the tests, a quantitative comparison between prediction and experiment is difficult. To simulate the fragmented state of the test samples, 10 and 25% of the grain boundaries were assumed to be fractured for the 1000- and 4000-MWd/t samples, respectively. As is evident from Table 9, the FASTGRASS predictions follow the trend observed for Xe, Sr, and Ba release as a function of temperature and burnup. For low-burnup irradiations, most of the Ba and Sr is predicted to be in atomic form rather than in a

sequestered state; thus, it is available for diffusional release. During the rather long time at the indicated temperature (≈5.5 h), FASTGRASS predicts significant release. This prediction is borne out by the data; e.g., in the case of the 4000-MWd/t fuel fragments, the measured Ba release was ≈18% at 1780°C and ≈60% at 1980°C. The corresponding FASTGRASS-predicted values follow the trend of these data, i.e., FASTGRASS predicted 11% and 57%, respectively. The Parker and Barton[42] data (Table 9) show some anomalous behavior. For example, at 1000 MWd/t and 1610°C the measured Ba release is a factor of two larger than the Xe gas release. This type of reported behavior is even more pronounced for the case of I and Cs release (not shown in Table 9), where measured I and Cs releases were up to four times higher than the Xe release.

Information on the predicted release mechanisms for these fission products is presented in Table 10. Results for Sr are similar to those for Ba. Most intragranular release during these low-burnup tests is predicted to occur by a grain-growth/grain-boundary-sweeping mechanism. Grain-growth/grain-boundary-sweeping effects are expected to be less important

Table 9. Xe, Ba, and Sr Release Data of Parker and Barton, Ref. 42, Compared with FASTGRASS Predictions

Temp. (°C) (°F)	Burnup (MWd/t)	Percent Released					
		Xe		Ba		Sr	
		Data	Predicted	Data	Predicted	Data	Predicted
1400	1000	0.5	0.2	1.8	0.009	0.06	0
2552	4000	6	2	0.5	0.002	0.08	0
1610	1000	6	3.5	12	1.3	0.2	0.03
2930	4000	14	9	15	0.5	0.5	0.02
1780	1000	14	12	21	9	3.7	1
3236	4000	42	29	18	11	6	1
1980	1000	49	27	51	26	10	17
3596	4000	71	69	60	57	33	23

[a]Fragments of irradiated fuel, weighing 0.1–0.2 g, were held at the indicated temperatures for 5.5 h.

Table 10. Predicted Intragranular Migration of Xe and Ba in 4000–MWd/t Fuel Fragments during the Parker and Barton Tests (Ref. 42)

Temp. (°C)	Product	Percent Released to Grain Boundary by Diffusion	Percent Released to Grain Boundary by Grain Boundary Sweeping
1400	Xe	72	28
	Ba	8	92
1780	Xe	11	89
	Ba	12	99
1980	Xe	8	92
	Ba	14	86

in higher burnup fuels, because of increased fission products present on the grain boundaries, which retard boundary movement, and because of sequestering of Ba and Sr by O in the fuel during fissioning.

As is shown in Table 11, the Ba and Sr species migrating in the fuel are predicted to be primarily in atomic form (this is also valid for Cs, not shown in the table). Very little BaO(g), SrO(g), and CsI is calculated to exist in bubbles, owing to their relatively low vapor pressure (e.g., compared to the noble gases) and the limited available bubble volume for 4000–MWd/T irradiated fuel. These calculations indicate that if BaO(g), SrO(g), and CsI(g) exist outside of the fuel, the molecules were formed, for the most part, either in the fuel open porosity or at the fuel surface, and not within fission–gas bubbles.

7.1.2 Fission–Product Behavior in High–Burnup Fuel during ORNL In–Cell Heating Tests with No Fuel Liquefaction

Figures 28 and 29 show FASTGRASS predictions of fission–gas and Cs release for ORNL Tests HI–1 and HI–3,[41,71–74] and compare them with corresponding measured quantities. The effects of fuel liquefaction are not considered here, but will be discussed in Section 7.1.3. Tests HI–1 and HI–3 were conducted for 30 min at 1673 K and 20 min at 2273 ± 50 K, respectively, within a flowing–steam environment. The fuel specimens were 20–cm–long sections of HBR fuel rod irradiated to 28,000 MWd/MTU. To

Table 11. Predicted Chemical Form of Retained Ba (4000 Mwd/t)

Temp. (°C)	Form	Lattice	Faces	Edges
1400	Ba	0.25	0	0
	BaO(c)	5.75	0	0
	BaO(g)	0	0	0
	$BaUO_4$	94	0	0
1610	Ba	5.5	0	0.1
	BaO(c)	23	0	0.4
	BaO(g)	0	0	0
	$BaUO_4$	70	0	1
1780	Ba	22	0	7
	BaO(c)	26	0	8
	BaO(G)	0	0	0
	$BaUO_4$	28	0	9
1980	Ba	16	0	50
	BaO(c)	6	0	19
	BaO(g)	0	0	0
	$BaUO_4$	2	0	7

correctly assess the state of the fuel prior to the test, a thermally and mechanically coupled model, consisting of FASTGRASS and the LIFE-LWR fuel behavior code, was used for the in-reactor irradiation period.[59] The total gas released during the irradiation was ≈0.2%.

The value of Q for stoichiometric $UO_{2.00}$ was used for both test simulations. This resulted in predictions of no grain growth for HI-1 and a 26-45% increase in grain size for HI-3. These grain growth predictions are consistent with microscopic observations. Scanning electron micrographs of HBR fuel specimens before and after Test HI-3 show that the grain size before transient heating was ≈6 μm, whereas post-test examination indicates an ≈50% increase in grain size. More detailed microscopic results are presented in Ref. 75.

To reflect the reported experimental uncertainty in temperature for Test HI-3, each part of Fig. 29 includes three predicted curves, which correspond to test temperatures of 2273 ± 50K. Also shown in Fig. 29 are

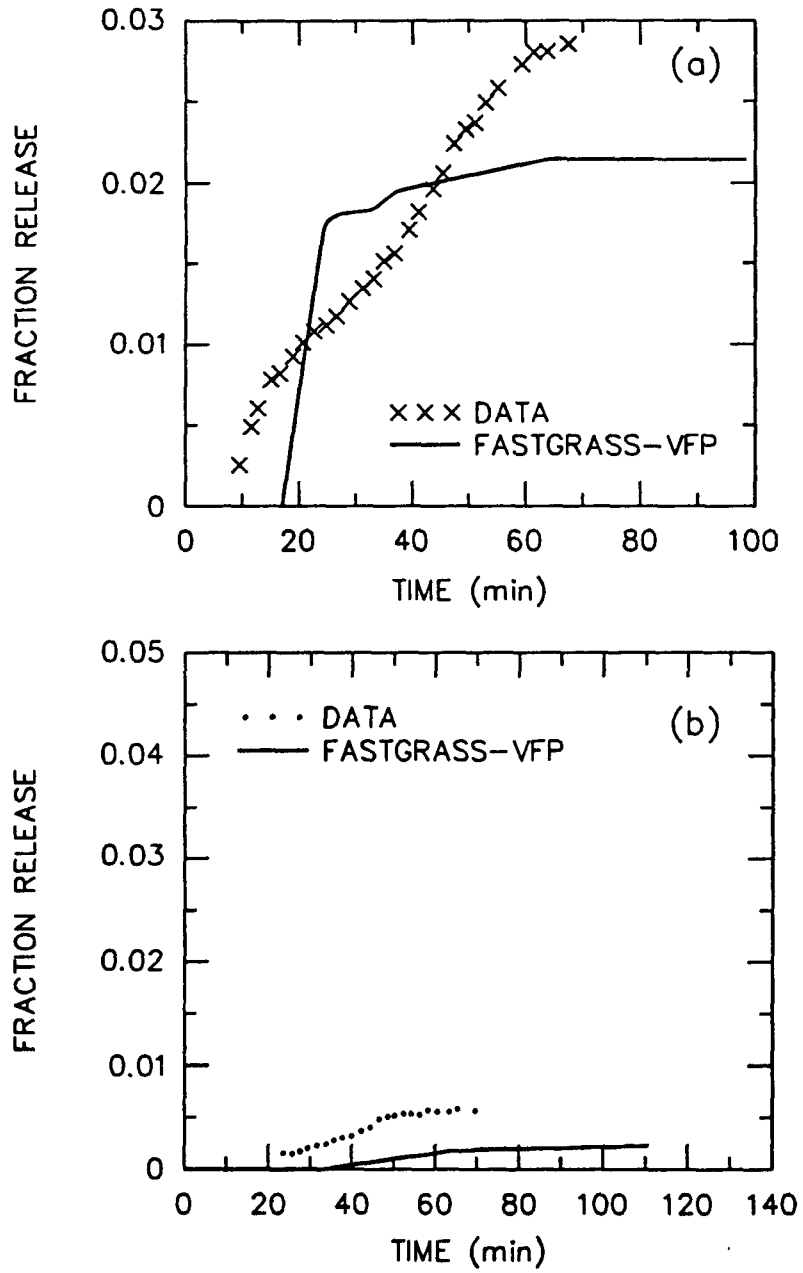

Fig. 28. FASTGRASS–VFP predictions of (a) fission–gas and (b) Cs release during ORNL Test HI–1, compared with measured values

the predictions in the absence of grain growth. On the basis of reasonable agreement between predictions and data for fission–gas and Cs release when a grain–growth/grain–boundary–sweeping mechanism is operative (Fig. 29), and between predicted and observed end–of–test grain size, it is concluded that grain boundary sweeping of fission products is a key mechanism for moving fission products from within the grains to the grain boundaries under HI–3 test conditions.

Whereas partial oxidation of the cladding was observed after Test HI–3, no visual evidence of appreciable fuel oxidation was detected. This result is

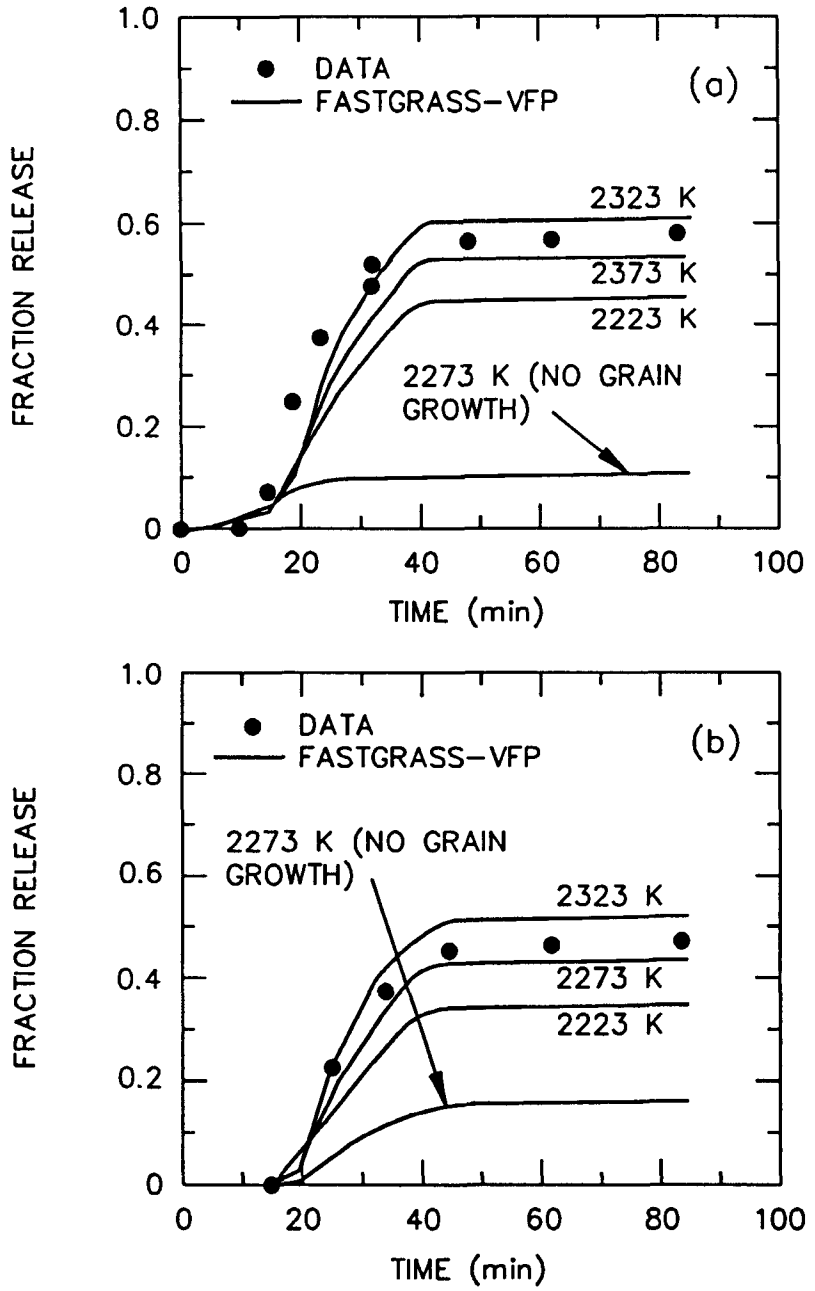

Fig. 29. FASTGRASS–VFP predictions of (a) fission–gas and (b) Cs release during ORNL Test HI–3, compared with measured values

consistent with the use of the stoichiometric grain growth law within FASTGRASS for HI–1, HI–3, and HI–4 (see Section 7.1.3) test conditions.

Figure 30 shows FASTGRASS predictions of fission–gas and Cs release for Test HI–2. The HI–2 test specimen was similar to specimens used in Tests HI–I and HI–3. Test HI–2 was conducted for 20 min at ≈1973 K in flowing steam. Metallographic examinations[74,75] of the tested fuel specimen revealed extensive fractures in the cladding, essentially complete oxidation to ZrO_2, and evidence of fuel–cladding interaction. Thus, it seems likely that fuel oxidation did occur during Test HI–2, in contrast to Tests HI–1,

HI-3, and HI-4. Each part of Fig. 30 shows predicted curves obtained with both the stoichiometric ("nominal") grain growth activation energy (maximum fuel temperature = 1973 ± 50 K), as well as predictions for the case of no grain growth (maximum fuel temperature = 1973 K). For cases where hyperstoichiometric grain growth activation energy was used, there is reasonable agreement between theory and experiment. Thus, both the experimental results available to date and the FASTGRASS analyses (Fig. 30) indicate that the UO_2 diffusivities were enhanced to some extent during Test HI-2 owing to UO_2 oxidation to UO_{2+x}.

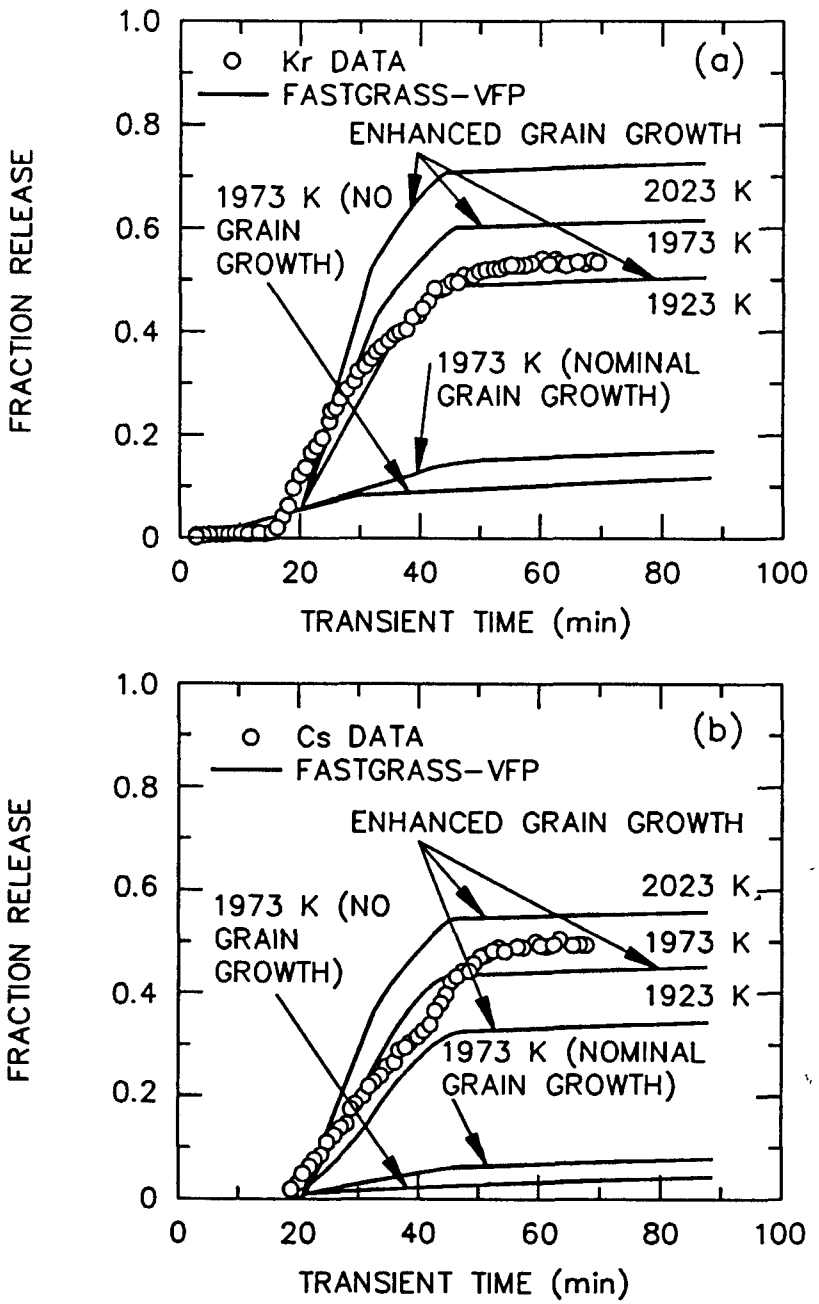

Fig. 30. FASTGRASS-VFP predictions of (a) fission-gas and (b) Cs release during ORNL Test HI-2, compared with measured values

7.1.3 Fission–Product Behavior in High–Burnup Fuel during ORNL In–Cell Heating Tests with Fuel Liquefaction

Figure 31 shows FASTGRASS predictions of fission–gas release for Test HI–3 with and without the effects of fuel liquefaction, compared with experimental observations. As discussed in Section 7.1.2 and shown in Figs. 29 and 31, the FASTGRASS calculations made under the assumption of no liquefaction are in good agreement with the data. The calculations made under the assumption that fuel liquefaction occurred in Test HI–3 (Fig. 31) show a degradation in the fission–gas release, and do not agree with the data. The reason for this result is that, during fuel liquefaction, the resultant enhanced growth of fission–gas bubbles in the liquefied lamina bordering the UO_2 grains reduces grain growth rates and grain boundary sweeping of intragranular fission products into the liquefied region. In addition, just subsequent to fuel liquefaction, fission–product release rates are reduced owing to decreased mobility in a viscous medium, compared to vapor transport through interconnected tunnels. The effect of reduced grain growth rates during fuel liquefaction is demonstrated in Fig. 32, which shows FASTGRASS predictions for grain growth during Test HI–3 with and without the effects of fuel liquefaction. Also shown in Fig. 32 is the reported grain size observed in the posttest fuel. As shown in Fig. 32, the predicted grain size without the effects of fuel liquefaction is consistent with the observations, whereas the calculated grain size for the case of fuel liquefaction is substantially below the reported values. The FASTGRASS results for fission–gas release and grain growth during Test HI–3 in the absence of fuel liquefaction are consistent with the result that only minimal evidence of fuel liquefaction was observed in Test HI–3.

Figure 33 shows FASTGRASS results for fission gas release during Test HI–4 with and without effects of fuel liquefaction, compared with the experimental observations. The fuel specimen for Test HI–4 consisted of a 20.3–cm–long fuel segment from a rod that had been irradiated in the Peach Bottom–2 reactor to about ≈10,100 MWd/MTU. Again, FASTGRASS–LIFE–LWR was used to simulate the irradiation period prior to the transient test. About 9% fission–gas release occurred from this rod during the irradiation. Test HI–4 consisted of 20 min at a temperature of 2273 ± 50 K in a flowing steam–helium atmosphere.

Grain boundary liquefaction of the fuel, i.e., formation of liquid U at temperature, was observed in portions of the fuel, principally near large

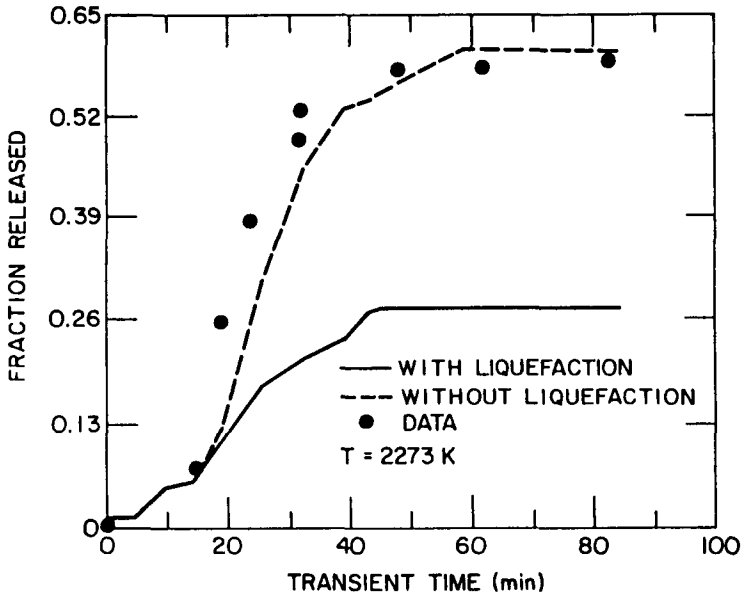

Fig. 31. FASTGRASS predictions of fission-gas release during ORNL Test HI-3 (max. fuel temperature = 2273 K) with and without the effects of fuel liquefaction, compared with measured values

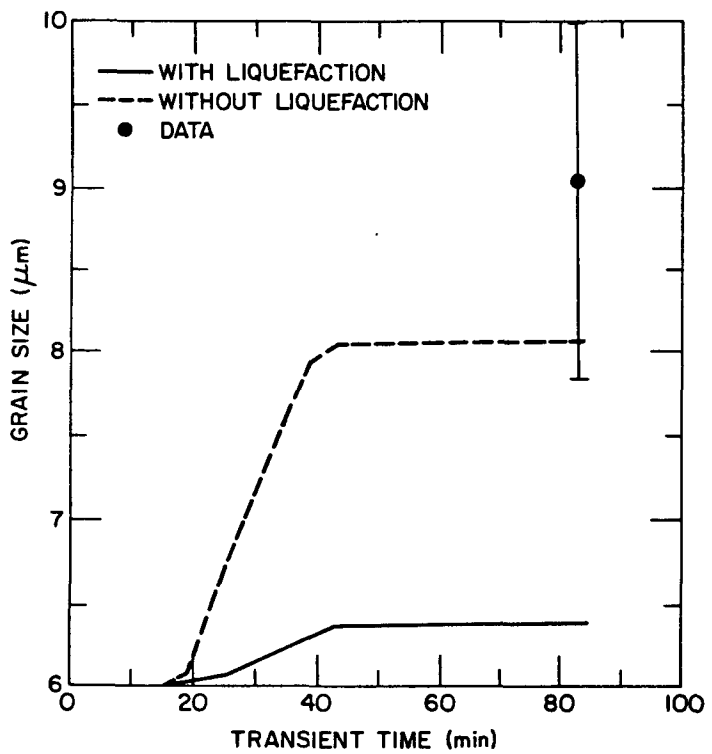

Fig. 32. FASTGRASS predictions of grain growth during ORNL Test HI-3 with and without the effects of fuel liquefaction, compared with measured values

amounts of Zircaloy.[75] As shown in Fig. 33, the FASTGRASS results for fission-gas release during Test HI-4 under liquefaction conditions are consistent with this observation. The calculations made under the assumption of no fuel liquefaction effects substantially overpredict the reported data. In addition, the FASTGRASS prediction of <10% increase in grain size is consistent with the observation of no grain growth within a 15% uncertainty range.

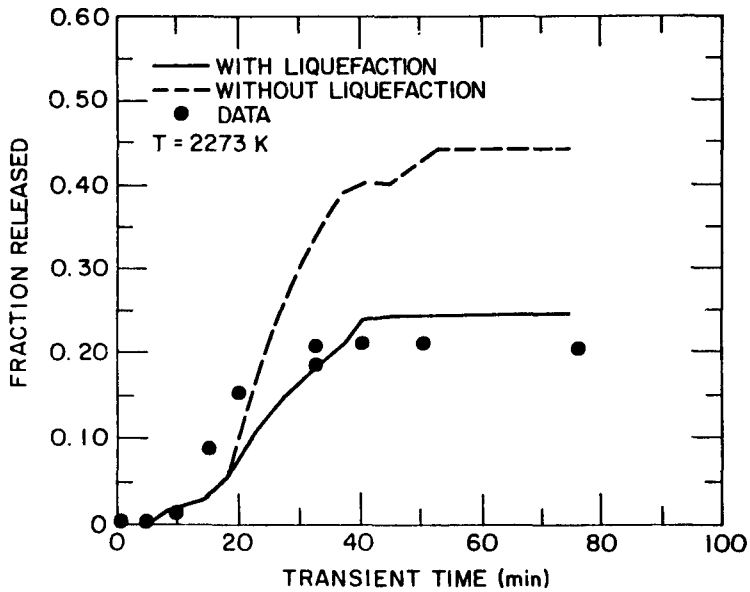

Fig. 33. FASTGRASS predictions of fission-gas release during ORNL Test HI-4 (max. fuel temperature = 2273 K) with and without the effects of fuel liquefaction, compared with measured values

7.2 Comparison with In-Reactor Data

The PBF-SFD test series[26,76] was initiated to obtain data on fission-product behavior under conditions of severe core degradation similar to those experienced at TMI-2. Each test was performed with 1-m-long Zircaloy-clad UO_2 fuel rods arranged in a 6 x 6 array, with corner rods missing. Trace-irradiated fuel (≅90 MWd/t) was used in the first and second tests, and normally irradiated fuel (≅30,000 Md/e) was used in the last two tests. The high-temperature fuel destruction phase of each test was achieved by reducing the inlet flow of coolant to the test bundle and increasing reactor power; the results were coolant boiloff, clad ballooning and rupture, Zircaloy and fuel oxidation by steam, clad melting and relocation, and release of noble gases and VFPs from the severely damaged fuel rods.

7.2.1 Fission-Product Behavior in Trace-Irradiated Fuel during SFD Tests in the PBF Reactor with No Fuel Liquefaction

The SFD-ST experiment consisted of a 32-rod bundle of PWR-type fuel rods, 0.91 m long and enclosed in an insulated shroud. The bundle was subjected to a slow heatup (≈2 h) in an O-rich environment to ≈1400 K in the lower part of the fuel bundle and ≈1800 K in the upper portion of the bundle and then rapid heatup (≈10 min) to 2400 K, followed by a rapid quench and coolant reflood. Considerable cladding oxidation and melting,

fuel liquefaction, and fuel fragmentation occurred. The SFD 1-1 test also consisted of a 32-rod bundle, but the temperature transient consisted of a rapid heatup (≈30 min) in a steam-starved environment to 2400 K, followed by a slow cooldown (≈20 min) without a rapid quench. The effective burnup levels for SFD-ST and SFD 1-1 are 88.9 and 79.1 MWd/MTU, respectively.

In Fig. 34, the measured fission-gas release rates for SFD-ST are compared with the release rates predicted by FASTGRASS on the basis of both the stoichiometric (nominal) and hyperstoichiometric (enhanced) grain growth activation energies. The enhanced grain growth activation energy, which is assumed to be activated at a time when the peak fuel temperatures exceed 1900 K, gives rise to a release-rate curve that simulates the trend of the ST data, whereas the nominal value of Q gives release rates that are approximately an order of magnitude below the data at fuel temperatures >1900 K. Such differences in predicted release characteristics due to grain-growth/grain-boundary-sweeping effects are further illustrated in Fig. 35, which shows *intra*granular fission-gas retention during SFD-ST as predicted by FASTGRASS. If nominal grain

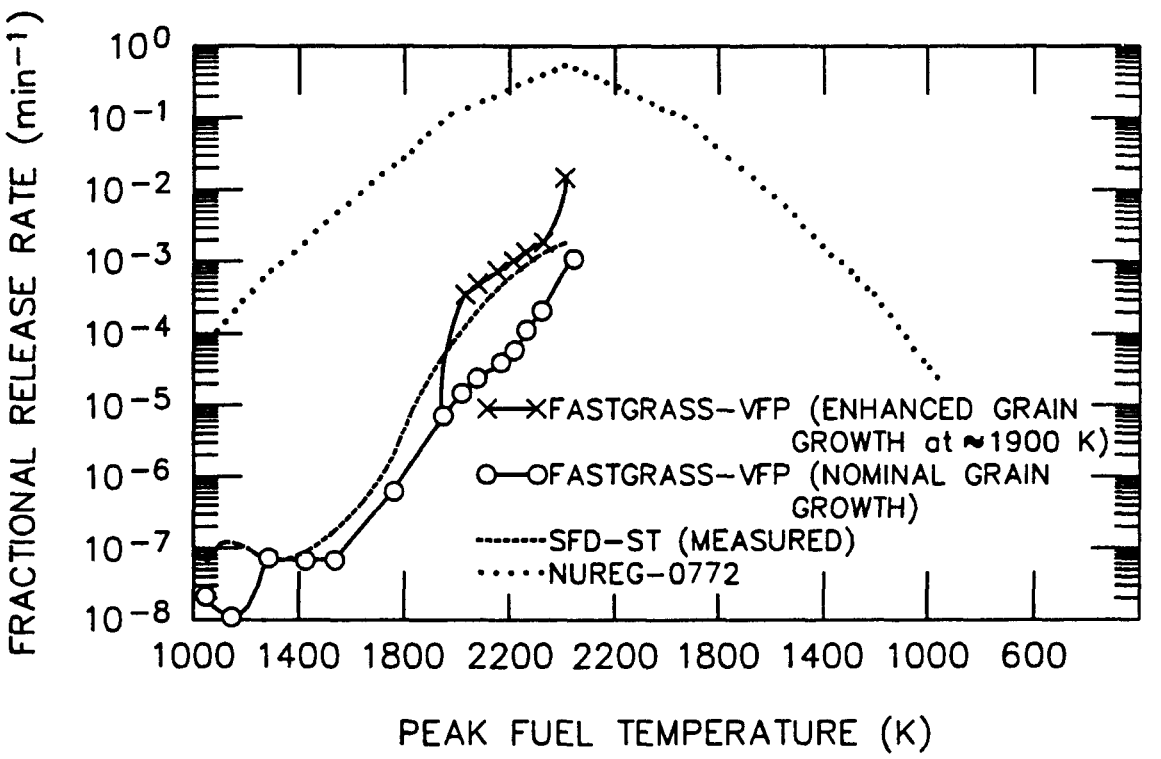

Fig. 34. FASTGRASS-VFP predictions of fission-gas release rates during the SFD-ST experiment, compared with measured values and those obtained from NUREG-0772 (Ref. 21)

growth occurs, the majority of the fission gas is predicted to remain trapped within the grain interior, with a total fractional retention of >80% even as fuel temperatures approach 2400 K. However, if the grain growth is enhanced owing to fuel oxidation, a much larger fraction of the *intra*granular gas is swept to grain boundaries, with only ≈10% retention within grains at fuel temperature of ≈2400 K. Such predictions clearly illustrate the important influence of the grain-growth/sweeping process on the morphology and attendant release behavior of gaseous and volatile fission products.

Figure 36 shows FASTGRASS predictions of grain growth in the hottest fuel region of SFD-ST for cases of nominal and enhanced grain growth. Theory predicts a more than twofold increase in grain size (for a 10-μm initial grain size) when hyperstoichiometric grain growth activation energy is invoked. Because the steam flow conditions of the SFD-ST scoping test produced an oxidizing environment, enhanced grain growth appears appropriate for this analysis. The analysis is also consistent with the fuel-oxidation-enhanced grain growth noted in the PBF-SFD scoping test, where both U_4O_9 precipitates and a substantial increase in grain size were noted upon posttest fuel examination.

In Table 12, FASTGRASS-VFP predictions for fission-product release during SFD-ST are compared with measured values. The calculations shown in Table 12 were made by assuming that requench provided the appropriate mechanisms (e.g., fuel fracturing) for the release of most of the fission products predicted to be on the grain boundaries. (FASTGRASS-VFP does not currently contain a model for requench-induced processes, e.g., grain boundary fracturing.)

As was stated previously, the value of the activation energy, Q, for grain boundary motion in hyperstoichiometric UO_2 was determined by the requirement that the integrated *intra*granular Xe release, as calculated by FASTGRASS-VFP, must be consistent with measured total (end-of-test) release values for SFD-ST. Thus, agreement between predicted Xe release values and SFD-ST-measured values, shown in Table 12, is a consequence of this procedure when used to determine a value of Q for oxidized UO_2. However, the successful interpretation of the HI 1-4 test series (Figs. 28-33) and of the trends of the PBF test fission-gas-*release-rate* data (e.g., Fig. 34), and the reasonable agreement between the predicted integral releases

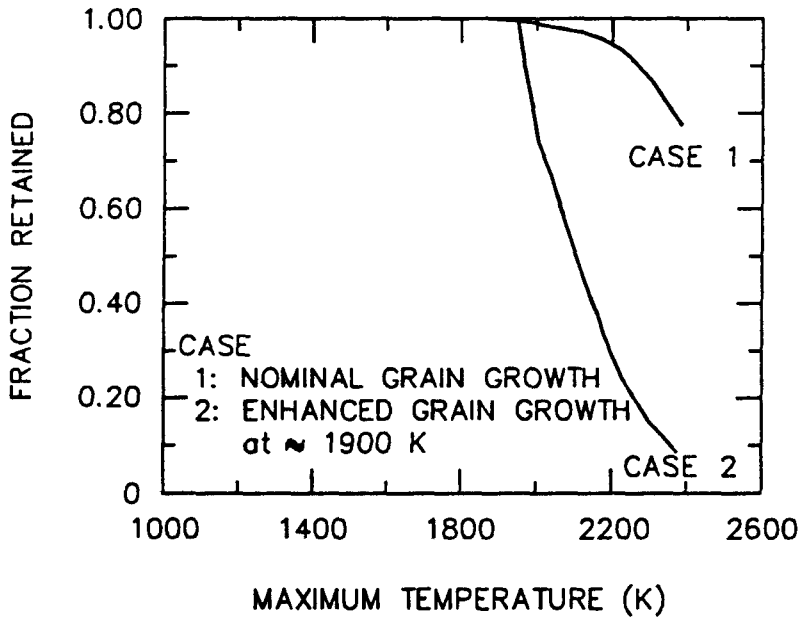

Fig. 35. FASTGRASS–VFP predictions of fission gas retained intragranularly at the hottest fuel region during the SFD–ST experiment, just prior to quench

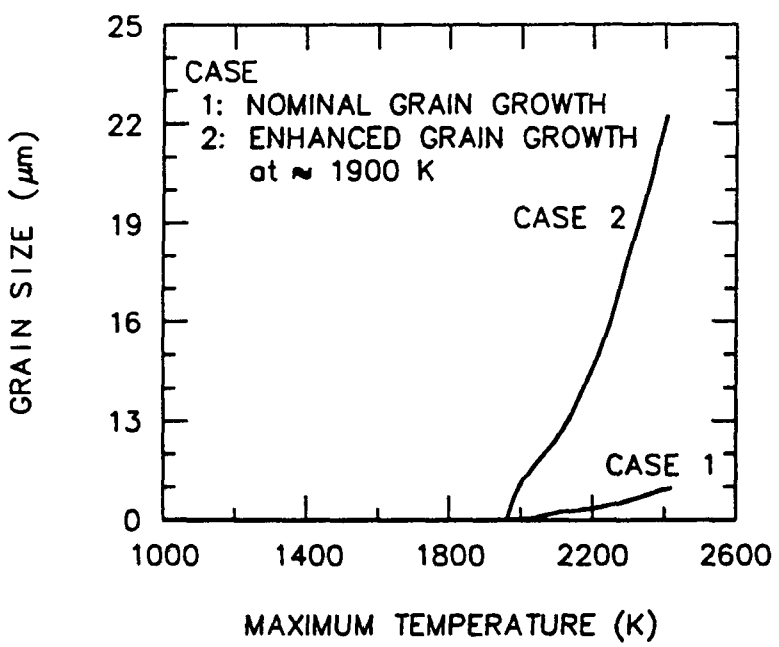

Fig. 36. FASTGRASS–VFP predictions of grain growth in the hottest fuel region during the SFD–ST experiment

of I and Cs and the PBF data (e.g., as shown in Table 12), support the hypothesis set forth in this report.

The results of the FASTGRASS calculations indicate that, in the absence of a requench (and fuel liquefaction), very little fission-product release would have occurred during SFD–ST. The reason for this is that, owing to the low concentrations of fission gas in this trace-irradiated, low-burnup fuel, very little interconnection of fission-gas bubbles is predicted to occur

Table 12. FASTGRASS–VFP Predictions of Fission–Product Release during the SFD–ST Test, Compared with Measured Values

Fission Product	Fraction Released	
	FASTGRASS–VFP Calculation	Collection Tank Measurement
Xe	0.50	≈0.50[a]
Cs	0.39	≈0.32
I	0.51	≈0.49

[a]Obtained from integration of release rate data.

on the grain faces and along the grain edges. This is in contrast to the ORNL transient tests on high–burnup fuel described earlier. The previously described relatively high concentration of fission gas in the high–burnup fuel enables a high degree of bubble interconnection to occur, with subsequent venting of retained fission products.

7.2.2 Fission–Product Behavior in Trace–Irradiated and High–Burnup Fuel during SFD Tests in the PBF Reactor with Fuel Liquefaction

FASTGRASS analyses indicate that for trace–irradiated fuel, most of both fission gases and volatiles (I and Cs) are retained within the interior of individual grains either as individual atoms or as newly nucleated *intra*granular microbubbles. FASTGRASS–VFP calculations indicate that such morphology will exist until grain growth causes the sweeping of *intra*granular microbubbles to grain boundaries. Because grain growth normally requires fuel temperatures in excess of 1900 K, significant release during the heatup phase of these PBF/SFD tests is precluded. Only when temperatures above 1900 K cause destruction of the grain boundary structure (by liquefaction, eutectic fuel melting and/or quench–induced processes such as grain boundary fracturing) is significant release predicted for such low–burnup fuel.

Test data for the PBF–SFD 1–1 and 1–4 tests are presented in Table 13. The SFD 1–1 transient consisted of a slow heatup of trace–irradiated (89 MWd/t) fuel to ≈1600 K, followed by a rapid heating that is driven by

Table 13. Percentage Fission-Product Release Measured during Two PBF-SFD Tests, Compared with FASTGRASS Predictions

Species	SFD 1-1			SFD 1-4		
	Data	Total Release	Potential Liquefaction Release	Data[a]	Total Release	Potential Liquefaction Release
Noble Gas	6.0±3.0	4.4	3.9	30-51	42	15
I	12	4.6	4.0	24	42	15
Cs	9.4	4.9	4.3	42	35	12.5
Te	≅0.3	0.15	0.13	<0.5	0.3	0.1
Ba	≅0.5	0.9	0.8	—	12	4
Sr	—	0.3	0.25	—	14	5

[a]Excluding irreversible deposition and filter content.

cladding oxidation in the upper regions of the fuel bundle. The peak fuel temperatures in most of the fuel rods were ≥2650 K. A significant amount of liquefaction/dissolution occurred in the SFD 1-1 test. In the SFD 1-4 test,[77] the transient closely matched that of SFD 1-1; however, irradiated (≈35,000 MWd/t) fuel rods were used in the SFD 1-4 test bundle. The liquefaction/dissolution scenario for SFD 1-4 was assumed to be identical with that of the SFD 1-1 test.

The spatial and axial temperature profiles provided to FASTGRASS were derived from calculations of the SCDAP computer model[77] and were adjusted to the best-estimate temperature profile. The initial effective grain size was 8 μm. The general lack of fuel oxidation during the SFD 1-1 test dictates a grain growth model driven only by temperature. The ≈7% fuel dissolution noted during postirradiation examination was simulated in FASTGRASS by allowing one of the ten fuel nodes to go into total dissolution (monotectic melting temperature = 2650 K), while four of the remaining nodes were modeled to have grain boundary liquefaction (liquefaction temperature = 2150 K). Because relocation information was not supplied, the cylindrical fuel geometry was maintained by FASTGRASS throughout the simulated transient.

In Fig. 37, the FASTGRASS-predicted fission-gas release rate for the SFD 1-1 test is compared with measured release rates. FASTGRASS calculations are shown with and without the effects of fuel liquefaction/dissolution. The release rates predicted by FASTGRASS with the effects of liquefaction/dissolution agree quite well with the trend of the release rates measured by SFD 1-1. In Fig. 38, FASTGRASS-calculated percent noble-gas release for SFD 1-1 are shown with and without the effects of liquefaction/dissolution. In Table 13, the FASTGRASS noble-gas release fractions are compared with the results of the on-line and grab-sample measurements. FASTGRASS calculations made with the effects of liquefaction/dissolution predict releases that are in better agreement with measured values.

The calculated SFD 1-1 noble-gas release (Fig. 38) is ≈4.4%, with liquefaction occurring at ≈2000 s. As indicated in Table 13, ≈3.9% noble-gas release is predicted from nodes that experience liquefaction, the remainder (0.5%) being released during solid-phase fuel heatup. Although enhanced release is still relatively low (4.4% total), bubble size for trace-irradiated fuel is quite small (≅10 Å diameter), and the mobility of the bubbles in liquids increases with increasing size.

Figure 39 shows GRASS-SST- and FASTGRASS-calculated bubble size distribution in liquefied UO_2 just subsequent to fuel dissolution for Tests

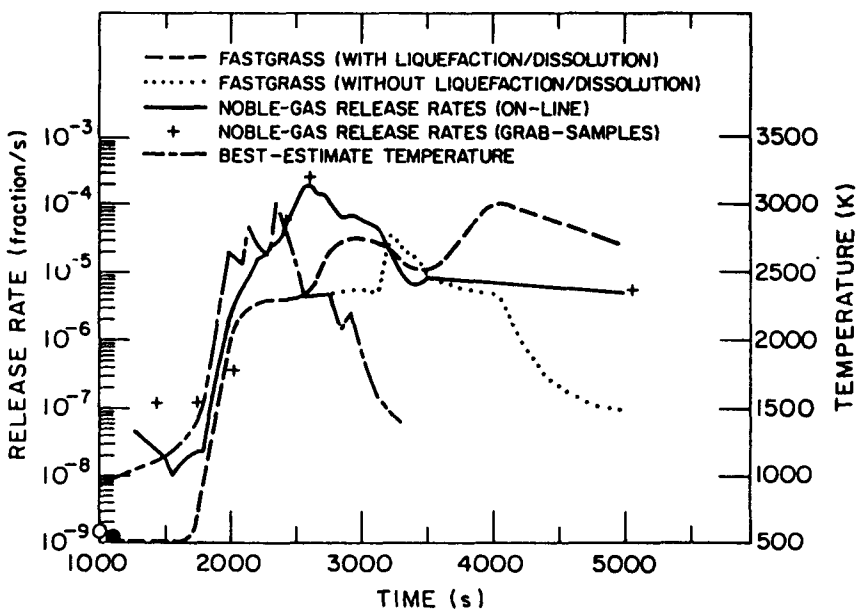

Fig. 37. FASTGRASS-calculated fission-gas release rates for SFD 1-1 with and without the effects of liquefaction/dissolution, compared with the measured values

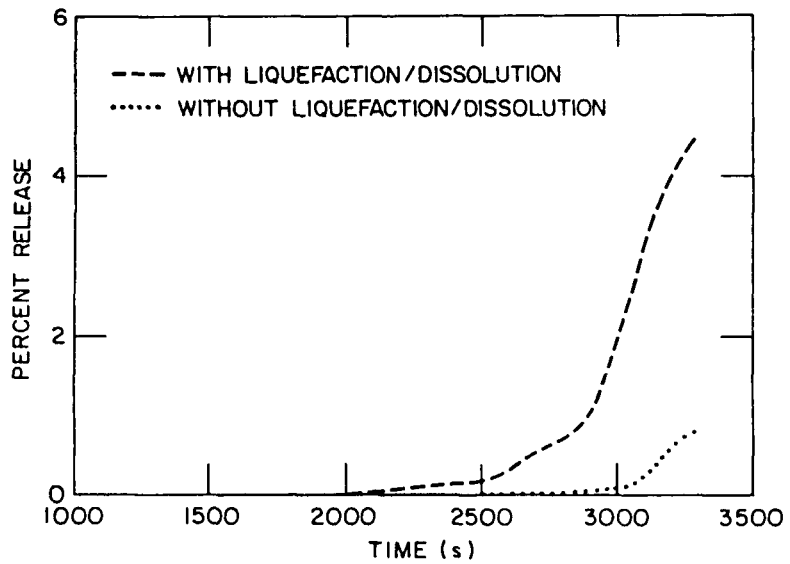

Fig. 38. FASTGRASS-calculated percent noble-gas release for SFD 1-1 with and without the effects of fuel liquefaction/dissolution

SFD 1-1 and SFD 1-4. (FASTGRASS considers two bubble size classes for fuel that has undergone dissolution, corresponding to bubbles that existed within the bulk and on the grain boundaries just prior to the phase change.) Also shown in Fig. 39 are the calculated results for SFD 1-1 just after fuel re-solidification. For the trace-irradiated SFD 1-1 fuel, the more detailed GRASS-SST mechanistic model shows that the peak in the bubble size distribution in liquid fuel occurs at a bubble diameter of ≈0.015 μm. For the irradiated fuel of SFD 1-4, GRASS-SST shows a bubble size distribution in liquid fuel with the peak occurring at a bubble diameter of ≈0.06 μm. The calculated bubble size distribution for SFD 1-4 is both higher and broader than that for SFD 1-1. Thus, as the bubble velocity in the liquefied fuel depends on bubble size (e.g., see Fig. 26), and the bubble coalescence rate depends additionally on bubble density, e.g., see Eq. 84, gas bubble escape from liquefied fuel (and thus the escape of other fission products which are swept out by the bubbles, e.g., I and Cs) will, in general, be much greater for normally irradiated fuel than for low-burnup fuel. Figure 39 also shows that FASTGRASS tends to approximate the GRASS-SST bubble size distributions (at least at the onset of dissolution) by calculating a high density of smaller than "average" size bubbles (i.e., the peak of the distribution), and a low density of larger than "average" size bubbles.

As the system evolves in the liquefied state, the FASTGRASS-calculated bubble sizes come into better agreement with those calculated by GRASS-SST. This is shown in Fig. 39 by the GRASS-SST-calculated bubble size distribution for SFD-1-1 just subsequent to fuel resolidification, and the

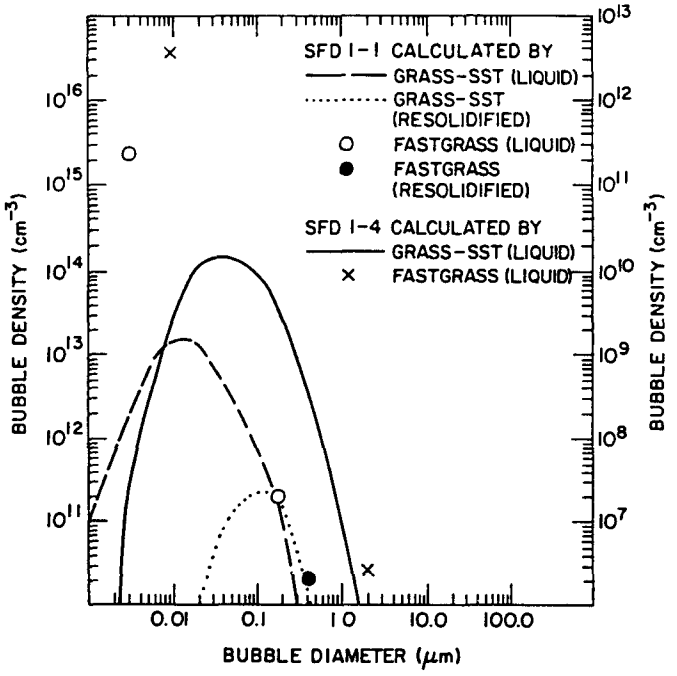

Fig. 39. GRASS–SST– and FAST–GRASS–calculated bubble size distribution in liquefied fuel just subsequent to fuel dissolution for SFD 1–1 and SFD 1–4, and FASTGRASS-calculated results for SFD 1–1 just subsequent to fuel resolidification

corresponding FASTGRASS–calculated value. The predicted releases are on the order of 50%. The results for SFD 1–4 do not appear in Fig. 39 because the predicted releases approached 100%. These results demonstrate that, in low–burnup fuel (e.g., SFD 1–1, TMI–2), appreciable fission–product retention in previously molten fuel is possible.

The curves shown in Figs. 37 and 38 incorporate the FASTGRASS grain–growth–fission–product–sweeping model. In view of the postirradiation examination findings of little fuel oxidation, the FASTGRASS simulation of the SFD 1–1 test incorporated grain growth kinetics, which were activated solely by temperature. The initial grain size was taken as 8 μm, and end–of–test calculated grain size was ≈12 μm. This compares favorably with the 10–12–μm grain size found during postirradiation examination of fuel debris samples. Although only limited grain growth is estimated by FAST–GRASS, the effect of such grain growth on the sweeping of fission gas from the grain interior to grain boundaries during solid–phase fuel heatup is pronounced. As shown in Table 14, FASTGRASS predicts that 3–85% of the retained gas in the undissolved pellets is trapped on the grain boundaries during solid–phase fuel heatup. However, once liquefaction temperatures (2150 K) are reached, partial release of this previously entrapped gas inventory is predicted to commence, with release occurring over the slow cooldown period, when the liquefied fuel was slowly cooled to a resolidified debris mass. Subsequent microcracking of fuel upon

termination of cooldown provides an additional mechanism (not considered here) for the added fission-product release that we noted late in the test.

Table 13 also shows release fractions measured during the SFD 1-1 and 1-4 tests and the FASTGRASS VFP/AEFP-calculated release fractions. As indicated, the FASTGRASS predictions are in reasonable agreement with the reported data. However, because the SFD 1-1 and 1-4 temperature and liquefaction/dissolution scenarios are somewhat uncertain, these results should be considered qualitative rather than quantitative. For the trace-irradiated fuel of the PBF-SFD 1-1 test, low release is predicted (Table 13). Approximately 1% of the Ba and 0.3% of the Sr are predicted to migrate to grain boundaries and to be trapped there during solid-phase fuel heatup. During fuel liquefaction/dissolution, this inventory of Ba and Sr is predicted to be released. This prediction agrees well with the test data (<1% measured release). Reliable data on Ba and Sr release for the SFD 1-4 test are not available at this time.

Shown in Table 13 is the quantity of fission products predicted to be released through the liquefied regions of the fuel after fuel heatup and during fuel cooldown. For the SFD 1-1 test, essentially all of the fission products are predicted to be released during the slow cooldown of liquefied fuel to a reconfigured solid debris mass. The reason for this result is that, during solid-phase heatup, in trace-irradiated fuel, it is calculated that very little open porosity exists on the grain boundaries. Thus, fuel liquefaction provides release paths for entrapped fission products. In the higher burnup SFD 1-4 fuel, fission-product release is partitioned between release by liquefaction and release through networks of open porosity. The greater degree of open porosity in the irradiated SFD 1-4 fuel is due to much higher concentrations of fission gas on the grain boundaries, and thus more extensive interlinkage to the fuel surface.

Table 14 presents the FASTGRASS-calculated behavior of I and Cs for SFD 1-1. The fission product I shows the same release characteristics as Xe and no CsI formation is predicted. Iodine is predicated to remain in atomic form and diffuse through the fuel matrix in a manner similar to that of Xe. This observation is supported by the work reported in Refs. 69 and 70. On the other hand, fission-product Cs either reacts with the fuel to form Cs uranate or migrates in atomic form. Because both I and Mo are fission products and are widely dispersed in the fuel matrix for trace-irradiated

Table 14. FASTGRASS–Calculated I, Cs, and Xe Morphology for Test SFD 1–1

Axial Node	Maximum Temperature (K)	Fuel Liquefaction/Dissolution	Fission Product Inventory Trapped on Grain Boundaries (%)					
			Xe	I	Cs	CsI	Cs_2UO_4	Cs_2MoO_4
1[a]	2349	Yes	17.6	21.8	26	0	0	0
2[b]	3025	Yes	—	—	—	—	—	—
3	2862	No	85.4	86.8	20.3	0	63.7	0
4	2662	No	69	72.6	9.2	0	61.8	0
5	2663	No	78.3	80.1	22.9	0	54.8	0
6[a]	2438	Yes	17	18.8	19.1	0	1.82	0
7[a]	2437	Yes	29.8	28.3	5.8	0	26	0
8[a]	2436	Yes	29.4	26.9	1.6	0	29.1	0
9	2439	No	35	32.5	2.0	0	21	0
10	2213	No	3.3	13.1	15.4	0	1.2	0

[a]Grain boundary liquefaction temperature = 2150 K.
[b]Monotectic melting temperature = 2650 K.

conditions, essentially no formation of CsI and $CsMoO_4$ is predicted for the SFD 1-1 fuel.

Table 15 presents the FASTGRASS-calculated release characteristics of Sr and Ba for the SFD 1-1 conditions. Both Sr and Ba react with the fuel or with O freed from the fissioning UO_2 to form BaO, $BaUO_4$, and SrO. The chemical affinity of Ba and Sr for O results in near-total sequestering of Sr and Ba as oxides or uranates within the fuel matrix or at grain boundaries and at the fuel open porosity.

Table 15. FASTGRASS-Calculated Ba and Sr Morphology for Test SFD 1-1

Axial Node	Maximum Temp. (K)	Fission-Product Inventory Fuel Liquef./Dissol.	Trapped at Grain Boundaries (%)				
			Ba	BaO	$BaUO_4$	Sr	SrO
1[a]	2349	Yes	0.14	1.9	14	0	12.6
2[b]	3025	Yes	--	--	--	--	--
3	2862	No	0	0.9	82	0	82.2
4	2662	No	0	0.4	67.3	0	64.9
5	2663	No	0	0.9	76.4	0	75.3
6[a]	2438	Yes	0	0.7	29.7	0	25.9
7[a]	2437	Yes	0	0.1	23.7	0	18.4
8[a]	2436	Yes	0	0.5	18.3	0	13.8
9	2439	No	0	0.25	21.5	0	17.6
10	2213	No	0	0.09	3	0	1.7

[a]Grain boundary liquefaction temperature = 2150K.
[b]Monotectic melting temperature = 2650K.

8 Comparison of FASTGRASS with Empirical Models

The NUREG-0772[78] fission-product release correlations (sometimes referred to as the CORSOR correlations) assume, for molten fuel, 100% instantaneous release of noble gases and the volatiles I and Cs. In contrast, release of these fission products from solid fuel is predicted to occur within about 10 min at temperatures exceeding ≈2000°C (2273 K). However, the

PBF-SFD data indicate that substantial fission product can be retained in liquefied fuel. FASTGRASS analysis of these test data supports these observations (see Section 7.2.2). For the trace-irradiated SFD 1-1 fuel, it is predicted that the low concentration of fission products in the fuel matrix will prevent appreciable bubble nucleation and growth, and hence, appreciable bubble escape velocities (see Figs. 26 and 27). For higher burnup fuels, the amount of release, although in general much greater than from trace-irradiated material, is still dependent on bubble mobility, fuel geometry, and time at fuel liquefaction temperatures.

Figures 40-42 show FASTGRASS predictions of noble gas, Cs, and Ba integral release fractions for fuel irradiation to a 3 at.% burnup condition and the following heating/cooldown scenario:

1. Preirradiation to 3 at.% burnup at a temperature of 1500 K (simulated normal reactor power operation).

2. Cooldown to 500 K (simulated reactor shutdown).

3. Simulated decay heat/loss-of-coolant accident, with a heatup rate of 2 K/s to temperatures in the 1800-2800 K range, with the fuel then held at constant temperature for up to several hundred hours.

This heating scenario is similar to that used at ORNL for the HI test series; (however, the HI test hold times were ≈30 min. Figure 40 shows the FASTGRASS-predicted fractional release for Xe. One hundred percent fission-gas release from solid fuel is predicted by FASTGRASS after an ≈11-min hold at 2800 K (fuel heatup took ≈19 min), whereas a hold period of ≈10 h is required at 2200 K to produce the same 100% fission-gas releases. The effect is even more dramatic at lower temperatures. The NUREG-07772 correlations predict 100% release at 2800 and 2200 K in ≈1 min and 10 min, respectively. Thus, the FASTGRASS mechanistic code predicts a much slower release rate than the NUREG-0772 correlation, even for normally irradiated fuel (30,000 MWd/t).

Figure 41 shows similar results for Cs release. For fuel temperatures of 2000-2800 K, the Cs release is similar to the Xe release. For lower temperatures (1800 K), the Cs release is somewhat lower than the Xe release. At lower fuel temperatures, the Cs tends to become sequestered in

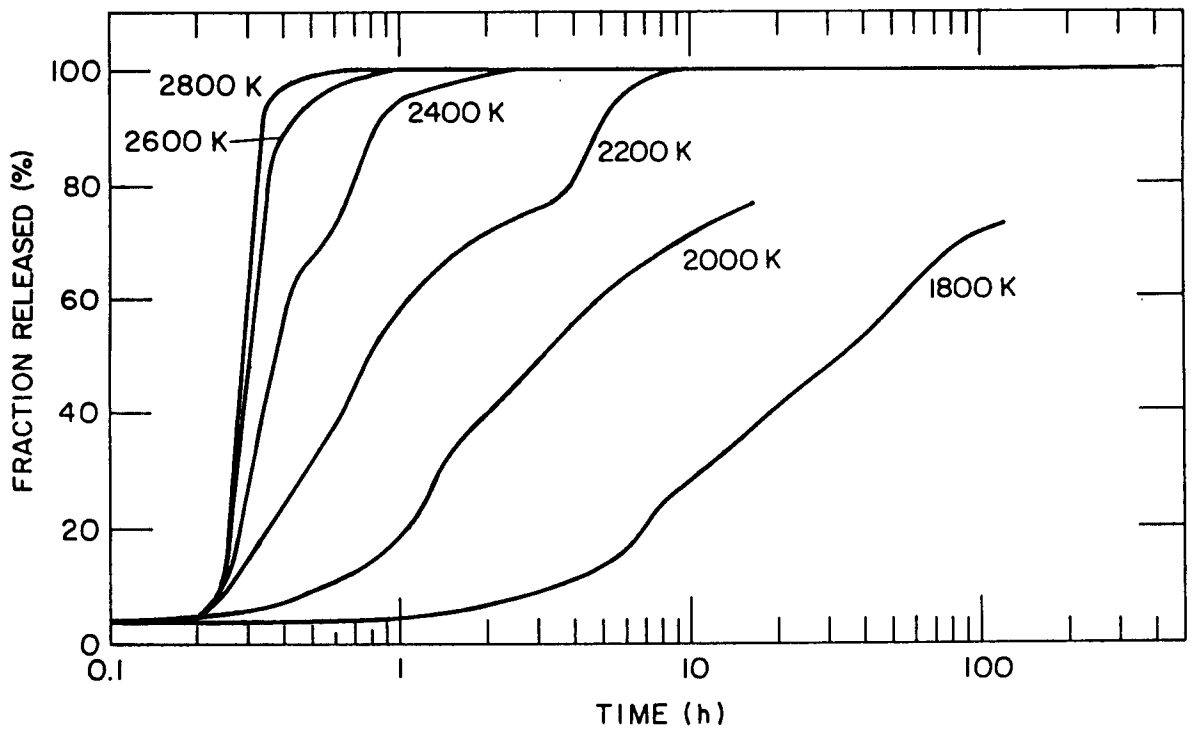

Fig. 40. FASTGRASS-calculated fission-gas release during fuel heatups to 1800–2800 K and during subsequent hold periods

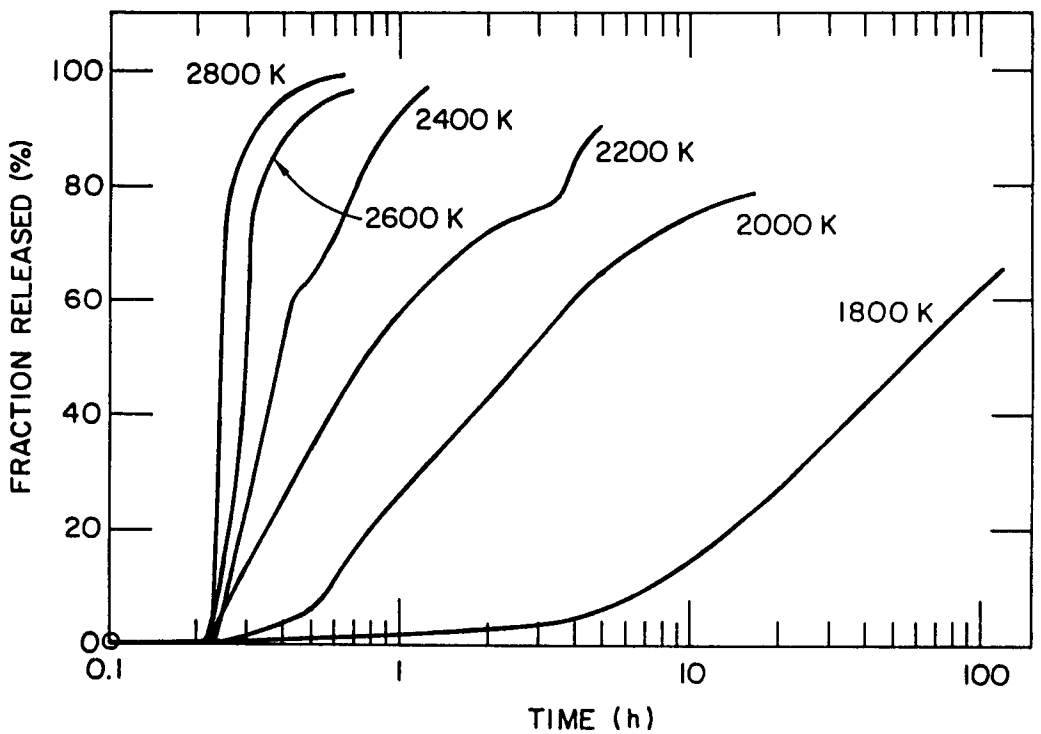

Fig. 41. FASTGRASS-calculated Cs release during fuel heatups to 1800–2800 K and during subsequent hold periods

the fuel as Cs_2UO_4 and Cs_2MoO_4, although, even in the absence of such chemical effects, the FASTGRASS model would predict lower rates for release of atomic Cs by bubble transport than the NUREG–0772 correlation.

Figure 42 shows FASTGRASS–calculated results for Ba. Virtually no release (i.e., <1%) occurs for fuel temperatures below 2000 K and hold times of several hundred hours. At 2200 K, the calculated Ba release is as follows: 14% after ≈4 h, 57% after a hold of ≈1 h at 2400 K (fuel heatup took ≈16 min), and 98% after a hold of ≈21 min at 2800 K. The limited release of Ba at temperatures below 2200 K is due to extensive sequestering of Ba as BaO(c) and $BaUO_4$(c) within the fuel matrix for this normally irradiated fuel.

Figure 43 shows the results of the theory for 16 ORNL transient fission-product release tests compared with measured values.[71–73] The data shown in Fig. 43 are part of the data base used to derive the NUREG–0772 release rate correlations. The temperatures were ramped to values of 500–1600°C and held for various lengths of time before test termination. In general, the agreement between theory and experiment is reasonable. A range of predicted values is shown for three tests in Fig. 43; the values correspond to

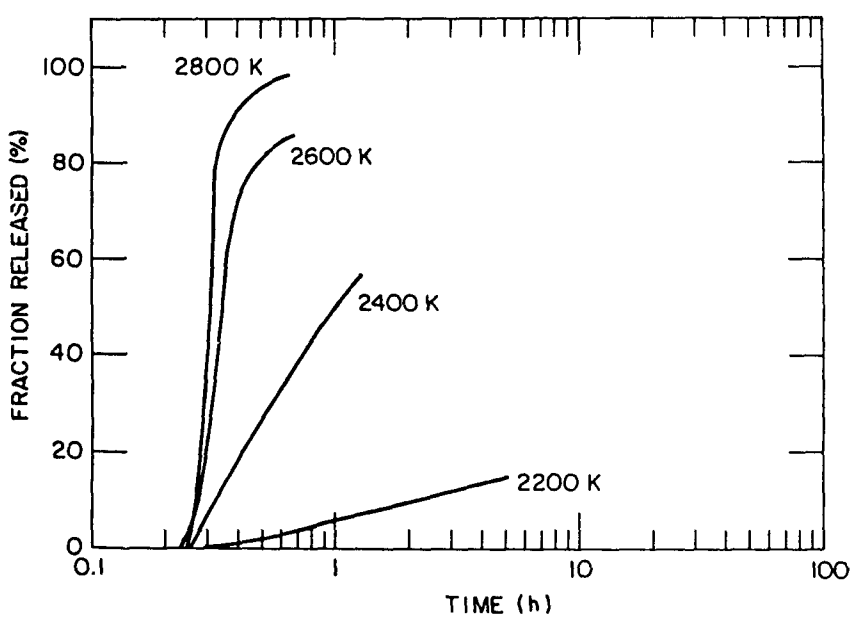

Fig. 42. FASTGRASS-calculated Ba release during fuel heatups to 2200–2800 K and during subsequent hold periods

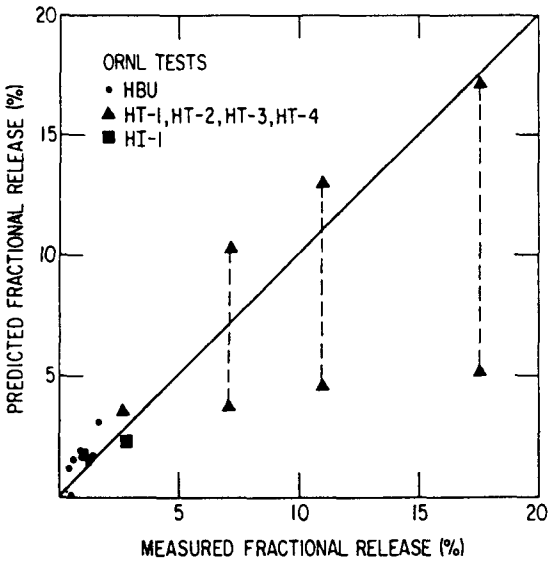

Fig. 43.
Predictions of transient gas release vs. experimentally measured values from the ORNL HBU, HT, and HI tests. The diagonal line indicates perfect agreement between theory and experiment

reported uncertainties[79] in the fuel temperatures during the test. The temperature uncertainties in these tests are attributed to combined heat from rapid oxidation of cladding and higher levels of ohmic energy deposition.

Figure 44 presents FASTGRASS–calculated average fission–gas release rates (obtained from the linear portion of the fractional release curves shown in Fig. 40), plotted against the reciprocal of the absolute temperature and compared with various ORNL data and the NUREG–0772 release rate curve. The linear fit to the ORNL release data from *horizontally* tested (HI) rods results in a curve that lies between the somewhat high NUREG–0772 correlations and the FASTGRASS predictions. The series of points above 10^{-1} fraction/min (at $4.5 \times 10^4/T$) are from Test HI–6, which was a short-time test (≈1 min), and the series of points at $\approx 3.5 \times 10^{-2}$ fraction/min (at $\approx 5.0 \times 10^4/T$) are from Test HI–2, which most likely experienced fuel oxidation. These points should be excluded from the comparison with the FASTGRASS curve, because this curve represents release from stoichiometric, solid fuel only, and for hold times representative of the linear portion of the fractional release curves shown in Fig. 40. The ORNL noble–gas release data from *vertically* tested (VI) fuel rods closely mirror the FASTGRASS curve. These findings support a mechanistic approach to modeling fission–product release, rather than the temperature–only empirical correlation employed in NUREG–0772.

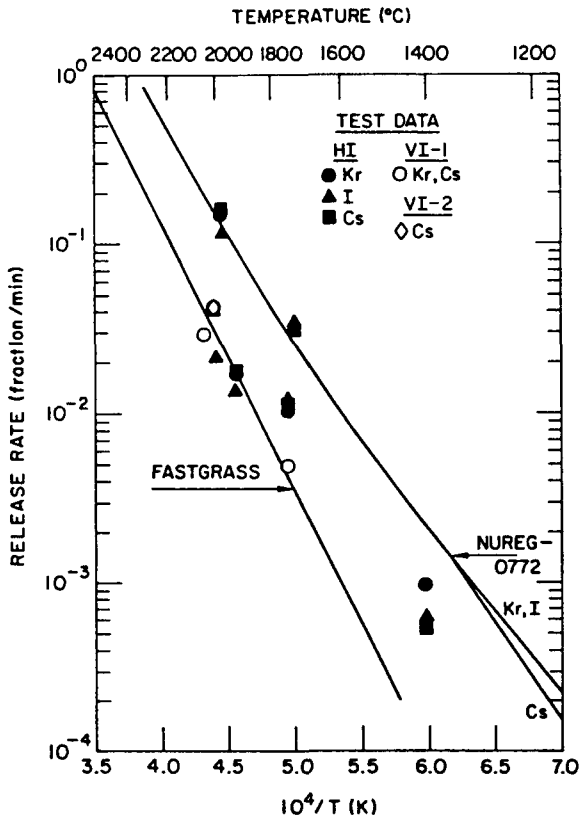

Fig. 44. FASTGRASS-calculated release rates from solid fuel obtained from the fractional release curves shown in Fig. 40, compared with various ORNL data and the NUREG 0772 release rate correlation

9 FASTGRASS Input Description

Description of Driver Input for FASTGRASS–VFP/PARAGRASS–VFP

Card No.	Variable Name	Description
1		
	ITLE	descriptive title
	IRSTAR	IRSTAR = 0: Normal execution
		IRSTAR = 1: Problem restart; program reads restart dump from Unit 15
1a		
	DUMP1	Defines Unit 15 for reading restart dump (IBM PC version only)

DUMP2	Defines Unit 16 for writing restart dump (IBM PC version only)	

2

GRS	Initial amount of gas in fuel cladding.	
FL	Fuel rod length (cm)	
NF	Total number of axial sections	
KF	Total number of radial rings	
JPL	Unused	
IVFP	IVFP = 0:	Calculation is done for noble gases and for Te, I, Cs, Ba, Sr
	IVFP ≠ 0:	Calculation is done for noble gases only
KPL	Unused	
NRD	NRD = −1:	Van der Waal EOS
	= 0:	Harrison EOS
	= 1:	Hard-sphere EOS
J1 J2	Calculation is done for axial fuel sections J1 through J2	
	Note: Input is done for axial fuel sections 1 through NF	
MF	Unused	
NXO	NXO = 0, 1	Option for O/M calculation NXO = 0 is nominal value

3

I PROG(I) Identifier	This card set provides the capability of modifying any member in labelled COMMON/PROG/PROG(183). Last card of this set must have I = blank or zero. This card set is read in subroutine ZRDWR.

4

DELT	Time step (s)	
NPRINT	Printout option	
	NPRINT ≤ 1:	No printout
	NPRINT = 2:	Partial printout for axial totals and rod totals only
	NPRINT > 2:	Full printout
INPLQ	Fuel liquefaction/dissolution option	
	INPLQ = 0:	No action
	INPLQ ≠ 0:	Read in card set #4E
IREAD	IREAD = 0:	No change in fuel properties and operating conditions for this time step
	IREAD = 1:	Fuel operating conditions to be updated for this time step; read in card sets #5 through #10
	IREAD = 2:	Fuel operating conditions and fuel properties to be updated for this time step; read in card sets #5 through #14
IOX	Fuel oxidation option	
	IOX = 0: No action	
	IOX ≠ 0: Read in card set #4D	

IP	IP = 0: No action IP = 1: Read in card sets #15 through #18 IP = 2: Read in card sets #15 through #18, print card sets #16 through #18
M1	Temporary variable, ICL is the tellurium sequestering option M1 = 0: No action M1 > 0: ICL = 1; tellurium sequestered by cladding M1 < 0: ICL = 0; Te not sequestered; retained Te released from cladding
IRSTAR	IRSTAR < 0: Halt calculation, write restart dump on unit 16, write summary printout IRSTAR > 2: Read in card set #3 in subroutine ZDWR IRSTAR other: No action
INV	Option to input fission-product inventories
INV = 0:	No action
INV > 0:	Read in card set #4B
INV < 0:	Read in card set #4C
ITRAN	ITRAN = 0: Steady-state mode ITRAN ≠ 0: Transient Mode
M2	Temporary variable, MCRK is microcracking option M2 = 0: No action M2 > 0: MCRK = 1; do not invoke microcracking model M2 < 0: MCRK = 0; invoke microcracking model
KFLX	Radial flux depression option KFLX = 0: All FDP (K,J) = 1; do not include card set #9

		KFLX = 1: Include card set #9 to define (FDP(K,1),K = 1,NF). Code will internally set (FDP(K,J) = FDP(K,1),J-2,NF)
		KFLX = 2: Include card set #9 to define J sets of (FDP(K,J),K = 1,KF)
	NCRK	Option to input grain boundary fracturing data
		NCRK = 0: No action
		NCRK ≠ 0: Read in card set #4A
	M3	Temporary variable; NOPT is grain growth option
		M3 = 0: No action
		M3 > 0: NOPT = M3
		M3 < 0: NOPT = 0
		NOPT = 0: No grain growth/grain boundary sweeping
		NOPT = 2: Empirical grain growth law
		NOPT = 3: Theoretical grain growth law
	NOTE:	ICL, MCRK, and NOPT are initialized to zero at the beginning of the run
4A	ALP(K,J)	Fraction of grain boundary area per unit volume separated by microcracks
4B	XGT(1-6)	Fission-product inventories in fuel for noble gases (1), Te (2), I (3), Cs (4), Ba (5), Sr (6) in grams. Note that if XGT(I) <0, that particular inventory remains unchanged. This option is invoked after beginning of a case.
4C		Initialization of fission-product inventories and associated variables NNF = NKF = 1 If INV < -1, NNF = NF, NKF = KF

		This card set consists of NNF * NKF sets of data. For SV and CI, the index N refers to 1: gas in lattice 2: bubbles in lattice 3: bubbles on face 4: bubbles on edge
	SV(N,K,J),N=1,4	Temporary variable that holds the radii (cm)
	CI(N,K,J),N=1,4	Temporary variable that holds apportionment factors. (CI(1) + CI(2) + CI(3) + CI(4) = 1.0
	GOU(N,K,J),N=1,6	Temporary variable that holds the XGT(I) as in card set #4B above. If NNF = 1 and NF >1, results (2 through J) = results(1)
4D	NXKJ(J)	Indices specifying grain growth activation energies for each axial section NXKJ(J) = 1: nominal; no fuel oxidation NXKJ(J) = 2: enhanced; fuel oxidation
4E	ISUM(J)	Temporary variable; ILIQ(J) is a flag that controls liquefaction/dissolution for each axial section ISUM(J) = 0: No action ISUM(J) ≠ 0: ILIQ(J) = 1 ILIQ(J) = 0: No liquefaction/dissolution However, if temperature > TKAUML (= PROG(79) = 3123), begin melting. Code will then internally set ILIQ(J) = 5. Should temperature later become < TKAUML, ILIQ(J) – 5 ILIQ(J) = 1: No action until temperature > TKLIQ (= PROG(81) = 2170), Whereupon ILIQ(J) is set internally to 2 and TLIQS(J) is calculated. After TLIQS(J) seconds and temperature is still > TKLIQ, ILIQ(J) is internally set to 3 and lique–

faction is assumed to occur. If temperature > TKDIS (= PROG(80) = 2650), dissolution is assumed to occur, ILIQ(J) is internally set to 4. Should temperature become < TKSOL (= PROG(82) = 1373), ILIQ(J) = -ILIQ(J) enables code to remember that section J experienced liquefaction/dissolution

If IREAD ≠ 0, go to card #15

5A	TS(K,J)	Temperatures at boundaries of regions (K,J)(K)
6A	TK(K,J)	Average temperature of regions (K,J) (K)
7A	POW(J)	Linear power in axial sections (kW/ft)
8A	PRSO(K,J)	Average hydrostatic pressure in regions (K,J) (psi)
9A	FDP(K,J)	See KFLX on card #4
10A	PLENP	Plenum pressure (psi) (not used)

If IREAD = 2, go to card #15

12A	RS(K,J)	Radius of the boundary of region (K,J)(cm)
13A	POROS(K,J)	Average fractional porosity in region (K,J)
14A	GRSIZ(K,J)	Average grain diameter in region (K,J) (cm)

If IP = 0, go to card #4

15		
	TMAX TDMIN TDMAX	The code will execute until the total time ≥ TMAX or the minimum fuel temperature TK (K,J) ≤ TDMIN or the maximum temperature TK(K,J) ≥ TDMAX
	IPRINT JPRINT IWRITE	(If NPRINT = JPRINT, printout for every IPRINT time step will be provided with NPRINT = IWRITE
	IPOW	IPOW = 0: Do not read in POW(J) IPOW = 1: Read in POW(J)
16	TD(K,J)	Temperatures TS(K,J) incremented by TD (K,J) during DELT
17	DPOW(J)	Power incremented by DPOW(J) during DELT

If IPOW = 0, go to card #4

18	POW(J)	Linear power in axial section J (kW/ft)

Repeat sequence starting with #4

Dictionary of Variables in COMMON/PROG/PROG(183)

Index	Variable Name	
1 - 9	A(1-9)	Parameters in the calculation of the UO_2 yield strength
10	AADC1	Pre-exponential factor for gas atom diffusion coefficient (cm^2/s)
11	AADC2	Activation energy for gas atom diffusion (cal)

12	ACON	Parameter that relates grain boundary area per unit volume to the equivalent grain diameter
13	ALFA	Used to define DRC (in ZRDWR); to be used in defining DRDT (in RDCAL in equilibrium model for radii calculations
14	ASTAR	Fraction of areal coverage of grain face by bubbles required for channel formation
15	ATMVOL	Volume associated with one molecule of fuel (cm^3)
16	AVN	Avogadro's number
17-22	BADC(1-6)	Coefficients in the semi-empirical/ phenomenological expression for intragranular bubble diffusivities
23	BOLTZ	Boltzmann's constant (ergs/K)
24	BVCRIT	Critical value of grain edge swelling required for long-range tunnel interlinkage
25	CALCA	Proportionality constant between theoretical and actual boundary separation rate
26	CD	Characteristic crack diameter (cm)
27	CRT	Relative error permitted in the integration
28	CR1	Relative error permitted in the bubble radius calculation
29	DELHV	Molar heat of vaporization (ergs/mole)
30 31	DU1(1) DU1(2)	Pre-exponential factors in expression for vacancy diffusion, in lattice (1) & in faces and edges (2) (cm^2/s)

32	DU1(3)	Parameter used in calculating the average bubble size in the lattice
33	DU1(4)	Parameter used in calculating the average bubble size on faces or on edges
34	DU2(1)	Activation energy for vacancy diffusion corresponding to DU1(1) above (cal)
35	DU2(2)	Activation energy for vacancy diffusion corresponding to DU1(2) above (cal)
36	DU2(3)	Parameter used in calculating the average bubble size corresponding to DU1(3) above
37	DU2(4)	Parameter used in calculating the average bubble size corresponding to DU1(4) above
38	DZERO	Pre-exponential factor in the expression for surface diffusion of UO_2 (cm^2/s)
39	EPSB	Parameter for the modified hard-sphere equation of state
40	FAWGE	Average number of grain faces per grain
41	FFM	Parameter for the modified hard-sphere equation of state
42	FFN	Parameter for the modified hard-sphere equation of state
43-51	FGPF(1-9)	FGPF(1-9) are the number of noble gas, Te, I, Cs, Ba, Sr, C_sI, B_aO, and S_rO atoms, respectively, produced per fission event
52	FINT	Unused
53	FN	Probability that two colliding atoms stick together to form a bubble nucleus

54	GAMMAL	Surface energy of a liquid/vapor interface (erg/cm^2)
55	GBR(1)	Multiplies RESCON to obtain effective irradiation-induced
56	GBR(2)	re-solution of gas atoms from grain face and edge bubbles, respectively
57	GC	Parameter for the modified hard-sphere equation of state
58-59	G1,G2	Coefficients in the expression for UO_2 surface energy
60	PDSC	Converts hydrostatic stress from lbs/sq. in. to dynes/cm^2
61	PTPL	POROS-PTPL contributes to PRF(K)
62	PZERO	Pre-exponential in the expression for the vapor pressure of the fuel (dynes/cm^2)
63	QS	Activation energy for surface diffusion (ergs/mole)
64	QSSTAR	Heat of transport for surface diffusion (ergs)
65	QSURF	Activation energy for surface diffusion (cal)
66	QVSTAR	Heat of transport for the volume diffusion mechanism (cal)
67	RCV	Universal gas constant, R (cal/K)
68	REDIS	Average distance traveled by an atom ejected from a grain boundary bubble (cm)
69	RESCON	Re-solution constant (cm^3)
70	RG	Gas constant [ergs/(gmol•K)]
71	RHOL	Liquid density (g/cm^3)

72	RLAMS	Proportional to gas atom jump distance (cm)
73	SBCF	Width of distribution of grain-face channel formation probability
74	SIG	Average collision diameter of UO_2 and Xe molecules (cm)
75	SIGMA	Parameter for the modified hard-sphere equation of state
76	SIGPI	Width of distribution of grain edge porosity interlinkage probability
77	TC	Parameter for the modified hard-sphere equation of state
78	THETA	Twice THETA is the dihedral equilibrium angle that a gas bubble makes with the grain boundary
79	TKAUML	Temperature at which melting occurs (K)
80	TKDIS	Temperature at which dissolution occurs (K)
81	TKLIQ	Temperature at which liquefaction occurs (K)
82	TKSOL	Temperature at which solidification occurs (K)
83	UPG	Unused
84	VC	Parameter for the modified hard-sphere equation of state
85	VIS	Viscosity of molten material (g/s•cm)
86	WM1	Molecular weight of UO_2
87	WM2	Molecular weight of Xe

88	XDL(1)	Maximum size of time step H used internally during steady state (s)
89	XDL(2)	Maximum size of time step H used internally during transient (s)
90	XDL(3)	Maximum size of time step H used immediately after dissolution/melting (s)
91	XKP	Ratio of the thermal conductivity of a pore to the thermal conductivity of fuel
92	XK1(1)	Nominal value of parameter in grain growth model, NOPT = 2
93	XK1(2)	Nominal value of parameter in grain growth model, NOPT = 2
94	XK2(1)	Nominal value of parameter in grain growth model, NOPT = 2
95	XK2(2)	Enhanced value of parameter in grain growth model, NOPT = 2
96	XK3(1)	Nominal value of parameter in grain growth model, NOPT = 3
97	XK3(2)	Enhanced value of parameter in grain growth model, NOPT = 3
98	XK4(1)	Nominal value of parameter in grain growth model, NOPT = 3
99	XK4(2)	Enhanced value of parameter in grain growth model, NOPT = 3
100	XK4C	Parameter in grain growth model
101	XMLT	Maximum radius of bubbles on faces during liquefaction (cm)

102	XMLTC	2*XMLTC = thickness of liquified boundary (cm)
103	ZZ1	Unused
104	BUMP(1)	The maximum factor by which SAVG(2) can increase in a given time step H is (1 + BUMP(1))
105	BUMP(2)	The maximum factor by which SAVG(3) and SAVG(4) can increase in a given time step H is (1 + BUMP(2))
106	GBSCE	Grain boundary sweeping efficiency
107	RC	Factor by which SAVG (2 through 4) can decrease
108	SVI(1)	Initial number of gas atoms per bubble in lattice
109	SVI(2)	Initial number of gas atoms per bubble on faces
110	SVI(3)	Initial number of gas atoms per bubble on edges
111	TSC(1)	TSC(1) *CRT is the minimum convergence criterion for Te
112	TSC(2)	TSC(1) *CRT is the minimum convergence criterion for I
113	TSC(3)	TSC(1) *CRT is the minimum convergence criterion for Cs
114	TSC(4)	TSC(1) *CRT is the minimum convergence criterion for Ba
115	TSC(5)	TSC(1) *CRT is the minimum convergence criterion for Sr
116	TSC(6)	Unused
117	VFN(1)	I solubility coefficient

118	VFN(2)	Cs solubility coefficient
119	VFN(3)	Ba solubility coefficient
120	VFN(4)	Sr solubility coefficient

Indices 121–128 are factors used to assess biased coalescence probabilities when using equal sized particles to characterize a distribution.

121	XOALP(1)	Atoms in lattice
122	XOALP(2)	Bubbles in lattice
123	XOBLP(1,1)	Bubbles on faces
124	XOBLP(2,1)	Bubbles on edges
125	XOBLP(1,2)	Bubbles in liquefied material
126	XOBLP(2,2)	Unused
127	ZZ2(1)	Unused
128	ZZ2(2)	Unused
129	ACI(1)	Parameters in chemical equilibrium model
130	ACI(2)	(activities)
131	ACI(3)	
132	CSDC1	Pre-exponential factor in expression for Cs diffusion (cm^2/s)
133	CSDC2	Activation energy for Cs diffusion/1.987 (cal)
134	GBSC(1)	Grain boundary swelling efficiency factors
135	GBSC(2)	Grain boundary swelling efficiency factors
136	HSOL(1)	Ba solution energy (cal)

137	HSOL(2)	Sr solution energy (cal)
138	OMO	O/M for stoichiometric UO_2 = 2.DO
139	TKLM	Maximum temperature bound in other chemistry model
140	TOL	
141	WKD1(1,1)	
142	WKD1(2,1)	
143	WKD1(1,2)	
144	WKD1(2,2)	
145	WKD2(1,1)	
146	WKD2(2,1)	
147	WKD2(1,2)	
148	WKD2(2,2)	
149	WKE1(1)	
150	WKE1(2)	Parameters in fuel/fission-product chemistry model
151	WKE2(1)	
152	WKE2(2)	
153	WOBS(1,1)	
154	WOBS(2,1)	
155	WOBS(1,2)	
156	WOBS(2,2)	
157	WQ(1,1)	
158	WQ(2,1)	
159	WQ(1,2)	
160	WQ(2,2)	
161	WQ(1,3)	
162	WQ(2,3)	
163	WQ(1,4)	
164	WQ(2,4)	
165	WQ(1,4)	
166	WQ(2,5)	
167	WQ(1,6)	
168	WQ(2,6)	
169	XOMC	

10 FASTGRASS Output Description

	NPRINT ≤ 1: No output = 2: Limited output > 2: Full output
ACAEN	Separated grain boundary area per unit volume (cm^2/cm^3)
ALPHA	Fractional coverage of grain boundary area per unit volume by microcracks
AREA	Surface area of annular region (K,J) through which fission products are migrating (cm^2)
BAL,BAF,BAE,BAOL, BAOF,BAOE	Ba concentrations in lattice, grain faces, and edges, respectively ($\#/cm^3$). The first entry is for after chemistry, the second for before chemistry.
BDBBLE	Intragranular diffusion coefficient of atoms and bubbles (cm^2/s)
BDMODL	Bubble velocity based on BDMODL (cm/s)
BDSURF	Diffusion coefficient for bubble movement, based on surface diffusion (cm^2/s)
BDVOL	Bubble diffusivity due to volume diffusion in a liquid medium (cm^2/s)
BETAB	Intragranular bubble nonequilibrium parameter
BIASA	Same as RANDA, but for biased diffusion
BIASB,BIASBAO,BIASSRO	Same as RANDB, but for biased diffusion
BUK	Fractional burnup
BVEVCD	Bubble velocity for above (cm/s)

BVKJ	Total strain due to gas bubbles
BVLIQ	Bubble velocity due to viscous rise in a liquid medium (cm/s)
BVS	Average swelling strain
BVSE	Fractional gas bubble strain due to bubbles trapped on grain edges
BVSF	Fractional gas bubble strain due to bubbles trapped on grain faces
BVSL	Fractional gas bubble strain due to bubbles trapped in the lattice
BVSURF	Bubble velocity, based on surface diffusion (cm/s)
BVVOL	Velocity of bubbles due to a volume diffusion in a liquid medium in the presence of a temperature gradient (cm/s)
C C	Convergence criteria
CNVF,EQK2	Parameters in chemical equilibrium model
CSL,CSF,CSE, CSIL,CSIF,CSIE	Cs concentrations in lattice, grain faces, and edges, respectively (#/cm^3). The first entry is for after chemistry, the second for before chemistry.
DCIE	Fission-enhanced diffusion coefficient (cm^2/s)
DELT	Time step (s)
DTDT	Heating rate in region (K,J) (K/s)
EGRE	Rate of gas migration from grain faces to edges due to grain face channel formation (s^{-1})

EPRF	Rate of gas atom release due to increased edge tunnel interconnection
ERRG...	Fractional error for Xe, Te, I, Cs, Ba, and Sr
FACE, EDGE	Gas bubble concentration on the grain faces, and edges, respectively (#/cm^3)
FGBAOB	Fraction of grain face area per unit volume covered by bubbles
FGBS (FBGSB,FGBSS)	Fraction of gas (Ba, Sr) arriving at faces due to grain boundary sweeping
FGR	Fractional gas release for noble gases, Te, I, Cs, Ba, Sr
FGRJ,FTERJ,FIRJ, FCSRJ,FBARJ,FSRRJ	Fractional gas release for Xe, Te, I, Cs, Ba, and Sr
FGRMGO	Fraction of generated gas released due to long-range migration processes (e.g., viscous rise in a liquid medium)
GAMMA	Surface tension of UO_2 (dynes/cm)
GASMGO	Gas migration out of annular region (atoms/cm^3)
GBS	Rate of intragranular gas release due to grain boundary sweeping mechanism (s^{-1})
GEN	Generated quantity of noble gases, Te, I, Cs, Ba, Sr, respectively (moles)
GOJ...	Xe, Te, I, Cs, Ba, and Sr released during DELT (moles)
GRD	Grain size (cm)
GSIN	Fission-gas generation rate (atoms/s/cm^3)

H	Current time increment (s)
HH	Current upper limit on the value of H (s)
HNXT	Suggested value for next time increment (s)
IL,IF,IE	I concentrations in lattice, grain faces, and edges, respectively (#/cm^3). The first entry is for after chemistry, the second for before chemistry
ILQ	Flag indicating the current state in liquefaction/ dissolution model

ILQ = 0:	No liquefaction or dissolution
ILQ = 1:	Liquefaction model has been invoked, but liquefaction has not occurred yet because temperature is below TKLIQ (2170 K)
ILQ = 2:	Temperature is ≥ TKLIQ, but TCAP < TLIQS
ILQ = 3:	TCAP ≥ TLIQS. Liquefaction is now occurring
ILQ = 4:	Dissolution is occurring
ILQ = 5:	Melting has occurred (no liquefaction or dissolution). Temperature > TKAUML (3123 K)
ILQ =-3:	Liquefaction has occurred, but material has now solidified due to temperature drop below TKSOL (1373 K)
ILQ =-4:	Dissolution has occurred, but material has now solidified due to temperature drop below TKSOL (1373 K)
ILQ =-5:	Melting had occurred, but material has now solidified due to temperature drop below TKSOL (1373 K)

J	Axial section
JX	NXKJ(J); index to indicate whether nominal or enhanced values of various parameters are being used
K	Radial section
LTCE	Gas atom and gas bubble concentration in lattice (#/cm^3)
OML,OMF,OME	O/M in lattice, on faces, and on edges
OUT	Gas release for noble gases, Te, I, Cs, Ba, Sr, CsI, BaO, SrO, respectively (moles)
PEX	Bubble over-pressure (dynes/cm^2)
POROS	Average as-fabricated porosity in region (K,J)
PPOL,PPOF,PPOE	Partial pressure of oxygen in lattice, on faces, and on edges (dynes/cm^2)
PRF	Pore interlinkage probability fraction at end of current time step
PRFOLD	Pore interlinkage probability fraction during the previous time step.
PRSO	PRSO (K,J) (lbs/cm^2)
RAD	Bubble radii (cm). Note: For grain faces and edges, RAD is the equivalent radius assuming a spherical shape, i.e., lenticular and ellipsoidal bubble geometries are used on grain faces and edges, respectively
RANDA (RANBA,RANSR)	Fraction of gas (BA,SR) arriving at faces due to random diffusion of gas atoms

RANDB,RANBAO, RANSRO	Fraction of bubbles, B_aO and S_rO in bubbles arriving at faces due to random diffusion of bubbles
RATIO	Fractional radius of region (K,J)
REQ	Equilibrium bubble radius (cm)
RET	Retained quantity of noble gases, Te, I, Cs, Ba, Sr, CsI, BaO, SrO, BaO(c), SrO(c), Cs_2UO_4, $Cs_2MoO_4Ba_2UO_4$, respectively (moles)
RGE	Fraction of retained fission product on edges for noble gases, Te, I, Cs, Ba, Sr, CsI, BaO, SrO, BaO(c), SrO(c), Cs_2UO_4, CS_2MoO_4, Ba_2UO_4
RGF	Fraction of retained fission product on faces for noble gases, Te, I, Cs, Ba, Sr, CsI, BaO, SrO, BaO(c), SrO(c), Cs_2UO_4, Cs_2MoO_4, Ba_2UO_4
RGGL,RGGF,RGGE	Fraction retained in the fuel lattice, on the faces, and on the edges, respectively, for Xe, Te, I, Cs, Ba, and Sr
RGL	Fraction of retained fission product in lattice for noble gases, Te, I, Cs, Ba, Sr, CsI, BaO, SrO, BaO(c), SrO(c), Cs_2UO_4, Cs_2MoO_4, Ba_2UO_4
RPIN	Fraction of retained intragranular fission gas that resides in bubbles
RRCON (1-9)	Fractional release rates for noble gases, Te, I, Cs, Ba, Sr, CsI, BaO, SrO, (1/s)
RS(K,J), RS(K+1,J)	Radii of the two boundaries of region (K,J) (cm)
SAVG	Average number of gas atoms/bubble

SRL, SRF,SRE, SROL,SROF,SROE	Sr concentrations in lattice, grain faces, and edges, respectively (#/cm^3). The first entry is for after chemistry, the second for before chemistry.
TAU	Time for which integration has been completed (s)
TCAP	Time elapsed since clad wetting (s)
TEL,TEF,TEE	Te concentrations in lattice, grain faces and edges, respectively (#/cm^3)
TFPV	Fission rate per unit volume in region (K,J) (fissions/cm^3/s)
TGRAD	Temperature gradient in region (K,J) (K/cm)
TKI	Average temperature in region (K,J) (K)
TKIO	Previous value of TKI (K)
TLIQS	Time required for liquefaction front to move across pellet radius (s)
TS(K,J) TS(K+1,J)	Temperatures of the two boundaries of region (K,J) (K)
VOLUME	Volume of the region (K,J) (cm^3)

11 Conclusions

The FASTGRASS analyses discussed in this paper support three major conclusions about fission-product behavior during severe fuel damage conditions:

1. Fission-product behavior in solid fuel strongly depends on fuel microstructure and irradiation history as well as fuel temperatures. This conclusion is most clearly demonstrated by the differences

between fission-product behavior of trace-irradiated fuel (SFD 1-1) and normally irradiated fuel (SFD 1-4, ORNL tests).

2. Fission-product behavior strongly depends on fission-product/fuel chemistry. This conclusion is evident in the differences in behavior of Xe, I, Cs, Ba, and Sr. Cs, Ba, and Sr become sequestered within the UO_2 as oxides, uranates, or molybdates. Formation of BaO(g), SrO(g), and CsI within the fuel is severely limited by their relatively low vapor pressures and the available bubble volume. The behavior of Cs, Ba, and Sr strongly depends on the Po_2 in the fuel. The chemical form of retained fission products is important for accidents where reheating and reliquefaction of fuel debris occurs after the primary accident scenario.

3. Fuel liquefaction/dissolution, fracturing, oxidation, and relocation strongly affect fission-product behavior during severe fuel-damage types of accidents. Fuel liquefaction/dissolution provides rapid escape paths for fission products entrapped in previously solid irradiated fuel (in trace-irradiated fuel, liquefaction/dissolution provides the major release paths). In addition, liquefied fuel provides a mechanism for continued high release, because fuel is slowly resolidified during the cooldown phase of the accident. Fission-product release strongly depends on timing and extent of fuel dissolution and relocation. For trace-irradiated, or very low burnup fuel, appreciable fission-product retention in previously liquefied fuel can occur due to low concentrations of fission products, and limited bubble growth in the liquefied material. For higher burnup fuel (under similar accident conditions), much larger bubble growth is predicted; hence, relatively lower fission-product retention is expected. In addition to liquefaction effects, oxidation of solid fuel leads to enhanced diffusivities and release rates. Fuel fracturing can also provide escape paths for fission products trapped on the grain boundaries of solid fuel.

4. The FASTGRASS mechanistic approach to the prediction of fission product release during severe core-damage accidents compares well with release trends noted in recent in- and out-of-reactor experiments. The FASTGRASS predictions are in much better agreement with the data over a wide range of temperature, fuel burnup, and fuel damage conditions than the present NUREG-0772 temperature-only empirical correlations.

Appendix A: FASTGRASS Model for Determining Ductile/Brittle Fuel Response

The ability to determine whether microcracking will occur during a given thermal transient is an important element in the prediction of fuel temperatures and fission-gas release. In principle, a "classical" mechanical treatment, involving the high-temperature stress/strain relationships of UO_2, could be used to study microcracking. Not only is this approach very complex, but it would require knowledge of the mechanical properties of UO_2, including strain rate effects, at high temperatures. Data in this area are sparse, and are almost nonexistent for temperatures in excess of 2400K.

As a first-cut approach to modeling the ductile/brittle behavior of oxide fuels, the DiMelfi-Deitrich model[63] has been used in the FASTGRASS code. This model estimates the growth rate of a grain boundary bubble under the driving force of internal pressurization. The volume growth rates due to crack propagation and diffusional processes are compared to determine the dominant mode of volume swelling. Knowledge of the mechanical properties of UO_2 is not required.

The underlying structure of the model can be summarized as follows: A fission-gas bubble on a grain boundary is assumed to act as a two-dimensional (cylindrical) crack nucleus. DiMelfi and Deitrich[63] assert that such a crack will propagate if the internal bubble pressure exceeds that required for bubble equilibrium, i.e., if

$$p > \frac{\gamma_s}{\rho} - \sigma, \tag{A1}$$

where

p = internal bubble pressure

γ_s = fuel-gas surface energy

ρ = bubble radius of curvature

σ = tensile stress normal to the boundary.

Further, if a bubble, initially at equilibrium, is subjected to transient heating, the internal pressure will increase above the equilibrium value. Under these conditions, crack propagation will occur unless diffusional

growth of the bubble occurs rapidly enough to maintain equilibrium conditions.

According to the DiMelfi–Deitrich model,[63] during most thermal transients, the initial mode of bubble growth will be crack propagation. The "cracklike" bubble tends to retain its equilibrium shape by diffusional transport of material along the grain boundary. However, if the heating rate is sufficiently high, high–pressure, cracklike growth predominates. Thus, the competition between diffusional growth and crack growth determines whether bubbles tend to remain isolated or rapidly become part of an interconnected network of microcracks.

In the DiMelfi–Deitrich analysis,[63] an attempt is made to predict the dominant mode of bubble growth by comparing the rates of volume swelling due to crack propagation and diffusional growth. In practice, this is done by comparing the instantaneous value of the grain boundary diffusion coefficient, D_i, with the minimum value needed to maintain the equilibrium bubble volume, D_g^{min}. (The derivation of D_g^{min} is discussed in detail in Ref. 63. If $D_i < D_g^{min}$, cracking dominates; this behavior is termed "brittle." If $D_i > D_g^{min}$, diffusional growth or "ductile" behavior dominates.

The minimum diffusion coefficient, D_g^{min}, is given by

$$wD_g^{min} = \left(\frac{mk^2}{\gamma s}\right)\frac{k\lambda AT^2}{HL\Omega(\Delta p)}. \tag{A2}$$

where

w = grain boundary width

m = average number of atoms per bubble arriving at the grain boundary

k = Boltzmann's constant

γ_s = surface energy of UO_2

λ = average bubble spacing in the grain boundary

A = instantaneous heating rate

T = temperature

H = geometric factor

L = bubble length

Ω = molecular volume of UO_2

Δp = pressure in excess of that required for an equilibrium grain boundary bubble.

In deriving Eq. A2, the ideal gas law and zero normal stresses on the grain boundary were assumed. (A conditional equation for D_g^{min} can be derived for the case of nonzero normal stresses on the grain boundary, e.g., see Ref. 63.)

The FASTGRASS code provides the gas bubble input for Eq. A2 as a function of time (i.e., λ, L, m, Δp). We have some reservations about the quantitative aspects of the DiMelfi–Deitrich analysis[63] but use it here as an interim model because it does seem to address the important real physical phenomena.

To evaluate the relative effects of crack growth versus equilibrium bubble growth on such properties as fuel temperature, intergranular swelling, grain boundary areal coverage, interconnected porosity, and gas release, the microcracking results are transmitted back to FASTGRASS and the thermal codes as a function of time. For example, the thermal conductivity, F_c, of UO_2 is given by

$$F_c = F_c^o\left[1.0 - C_2\left(\frac{A_e}{A_c}\right)_i x_i \Delta t_i\right]$$

$$= F_c^o(1.0 - C_2 S_v), \qquad \text{(A3)}$$

where

F_c^o = thermal conductivity of uncracked, stoichiometric UO_2

C_1, C_2 = constants

$(A_c/A_e)_i$ = ratio of the areal coverage of a crack to that of an equilibrium bubble

x_i = projected grain face areal coverage per unit volume of bubbles

Δt = time increment

S_v = pore/solid surface area per unit volume.

The constant C_1 is nonzero whenever $D_i < D_g^{min}$ (see Eq. A2). The effect of microcracking on the thermal conductivity of UO_2, as described in Eq. A3, can result in values for $F_c \approx 50\%$ of the value in dense fuel. A change of this magnitude will strongly affect calculated temperature profiles.

Appendix B: Solution of Harrison's Equation of State with Capillarity Equation

Simultaneous solution of Harrison's Equation of State, Eq. 23, with the capillarity equation, Eq. 20, results in the quartic equation

$$R^4 + \frac{2\gamma}{P_h}R^3 - \frac{3M}{4\pi}\left(DLM + \frac{AT}{P_h}\right)R - \frac{3M}{4\pi}\frac{2\gamma}{P_h}DLM = 0, \tag{B1}$$

which, in general, has four roots and is subsequently carried out by utilizing the Van der Waals equation assuming that $P_h = O$. The algorithm for finding the appropriate root is given below.

The quartic equation in R, Eq. B1 is rewritten with

$$R^4 + a_3R^3 + a_1R + a_0 = 0,$$

$$a_3 = \frac{2\gamma}{P_h} x 10^4,$$

$$a_1 = -\frac{3}{4\pi}M\left(b + \frac{AT}{P_h}\right) x 10^{12},$$

and

$$a_o = -\frac{3}{4\pi}M\,b\frac{2\gamma}{P_h} x 10^{16}, \tag{B2}$$

where the factors of 10 reflect a change in units from cm to microns. It appears that, for physically realistic values of the coefficients, two of the roots are real and two are imaginary. If P_h is positive, only one of the real roots is positive and corresponds to the equilibrium bubble radius.

If P_h is negative, both real roots are positive, the smaller being the stable equilibrium bubble size and the larger the unstable equilibrium bubble size. To find the roots of the quartic equation, the real roots of the resolvent cubic equation are first calculated as follows:

$$y^3 + b_1 y + b_0 = 0, \tag{B3}$$

where

$$b_1 = a_1 a_3 - 4a_0,$$

$$b_0 = -a_1^2 - a_0 a_3^2.$$

For the cubic equation, if

$$b \equiv \frac{b_0^2}{4} + \frac{b_1^3}{27} > 0, \tag{B4}$$

there is only one real root, which is given by

$$u = \left(-\frac{bo}{2} + \sqrt{b}\right)^{1/3} + \left(-\frac{b_0}{2} - \sqrt{b}\right)^{1/3}. \tag{B5}$$

In the case where $b_1 > O$, it may be that u is the difference of two approximately equal numbers. Therefore, the expression for u is rewritten, multiplying it by

$$\frac{\left(-\frac{b_0}{2} + \sqrt{b}\right)^{2/3} + \left(-\frac{b_0}{2} - \sqrt{b}\right)^{2/3} + \frac{b_1}{3}}{\left(-\frac{b_0}{2} + \sqrt{b}\right)^{2/3} + \left(-\frac{b_0}{2} - \sqrt{b}\right)^{2/3} + \frac{b_1}{3}}$$

to obtain

$$u = -\frac{bo}{\left(-\frac{b_0}{2} + \sqrt{b}\right)^{2/3} + \left(-\frac{b_0}{2} - \sqrt{b}\right)^{2/3} + \frac{b_1}{3}}. \tag{B6}$$

Once the root, u, of the resolvent cubic is obtained, the four roots of the quartic equation are given as roots of the two quadratic equations

$$X^2+\frac{a_3}{2}X+\frac{u}{2}=\pm\sqrt{\left(\frac{a_3^2}{4}+u\right)X^2+\left(\frac{a_3}{2}u-a_1\right)X+\left(\frac{u^2}{4}-a_0\right)}, \tag{B7}$$

where the radicand on the right is the perfect square

$$\left(\sqrt{\frac{a_3^2}{4}+uX}\pm\sqrt{\frac{u^2}{4}-a_0}\right)^2.$$

and the sign is chosen according to the sign of the middle term, $\frac{a_3}{2}u-a_1$.

The quadratic equations can be rewritten as

$$X^2+c_1X+c_0=0, \tag{B8}$$

where

$$c_1=\frac{a_3}{2}\pm\sqrt{\frac{a_3^2}{4}+u},$$

and

$$c_0=\frac{u}{2}\pm\sqrt{\frac{u^2}{4}-a_o},$$

with the pairing of the signs chosen according to the value of the term $\frac{a_3}{2}u-a_1$. When this term is >0, the signs are chosen either both positive or both negative; when it is < 0, the signs are chosen one positive and one negative. The roots of the quartic, then, are

$$R=-\frac{c_1}{2}\pm\sqrt{\frac{c_1^2}{4}-c_0}. \tag{B9}$$

The cubic equation has three real roots for the case $b \le 0$. Again, it appears that, for physically realistic cases, only one of the roots is required. When $b = 0$, the root is given by

$$u = 2\left(-\frac{b_o}{2}\right)^{1/3}. \tag{B10}$$

When b < 0, the root is given by

$$u = 2\sqrt{-\frac{b_1}{3}}\cos\left(\frac{\theta}{3}\right), \tag{B11}$$

where

$$\cos\theta = -\frac{b_o}{2} \div \sqrt{\left(-\frac{b_1^3}{27}\right)}.$$

In general, there exists no more than one stable equilibrium bubble radius for a given set of conditions. In the case of a compressive-stress state, the stable radius is given by the single positive real root. In the case of a tensile stress state, there may exist one stable equilibrium bubble radius and one unstable equilibrium bubble radius. There will then be two corresponding positive real roots. The larger of the two is the unstable radius, whereas the smaller of the two is the stable radius. For large tensile stresses, there may be no equilibrium bubble radii and the two positive roots become imaginary. An algorithm that selects the appropriate root has been developed and is utilized. The selection is based on the signs of the three quantities, a_3, $a_3u/2 - a_1$, and u. Only four out of eight possible combinations need be considered. The algorithm is summarized in Table B1. A generally more accurate formula can be written for the case when one of the quantities is defined as a difference. For example, consider the first entry in Table B1, where a_3 is positive and c_1 may be rewritten, after multiplying by $-1/2\left(a_3/2+\sqrt{a_3^2/4+u}\right)$, as $u/\left(a_3+\sqrt{a_3+4u}\right)$. The actual algorithm used is summarized in Table B2. Other combinations of a_3, $a_3u/2 - a_1$, and u are not expected.

The equation of state published by Harrison[22] is in tabular form; therefore, it is necessary to write an algorithm to determine the parameters DLM and AT in Eq. B1. Harrison[22] presents Xe pressures for various values of gas temperature and density. Above about twice the critical temperature, T_c (which is 289.74 K for Xe), the pressure, PT_j, at any given density varies linearly with the reduced temperature, T_R, and is given by

$$PT_j = SL_j \times T_R + BI_j. \tag{B12}$$

The values of SL_j and BI_j are obtained from a least squares fit of PT_j to the published values of the pressure, P. Values of SL_j and BI_j for 17 different values of the density, d_j, are given in Table B3, along with the corresponding values of the molar volume, DI_j. (Pressure calculated in this way is in dynes/cm^2.) DLM and AT are computed with an iterative scheme. If no solution is found, the bubble radius is computed using the hard sphere method.

Table B1. Possible Roots of the Quartic Equation

a_3	$a_3u/2-a_1$	u	c_1	c_0	R
+	+	+	$\frac{a_3}{2}-\sqrt{\frac{a_3^2}{4}+u}$	$\frac{u}{2}-\sqrt{\frac{u^2}{4}-a_0}$	$-\frac{c_1}{2}-\sqrt{\frac{c_1^2}{4}-c_0}$
+	−	−	$\frac{a_3}{2}-\sqrt{\frac{a_3^2}{4}+u}$	$\frac{u}{2}-\sqrt{\frac{u^2}{4}-a_0}$	$-\frac{c_1}{2}-\sqrt{\frac{c_1^2}{4}-c_0}$
−	−	+	$\frac{a_3}{2}-\sqrt{\frac{a_3^2}{4}+u}$	$\frac{u}{2}-\sqrt{\frac{u^2}{4}-a_0}$	$-\frac{c_1}{2}-\sqrt{\frac{c_1^2}{4}-c_0}$
+	+	−	$\frac{a_3}{2}-\sqrt{\frac{a_3^2}{4}+u}$	$\frac{u}{2}-\sqrt{\frac{u^2}{4}-a_0}$	$-\frac{c_1}{2}-\sqrt{\frac{c_1^2}{4}-c_0}$

Table B2. Roots of the Quartic Equation

a_3	$a_3u/2-a_1$	u	c_1	c_0	R
+	+	+	$\dfrac{u}{a_3+\sqrt{a_3^2+4u}}$	$\dfrac{2a_0}{u+\sqrt{u^2-4a_0}}$	$c_1+\sqrt{c_1^2-c_0}$
+	−	−	$\dfrac{a_3}{2}-\sqrt{\dfrac{a_3^2}{4}+u}$	$\dfrac{u}{2}-\sqrt{\dfrac{u^2}{4}-a_0}$	$-\dfrac{2c_0}{c_1+\sqrt{c_1^2-4c_0}}$
−	−	+	$\dfrac{a_3}{2}-\sqrt{\dfrac{a_3^2}{4}+\ddot{u}}$	$\dfrac{u}{2}-\sqrt{\dfrac{u^2}{4}-a_0}$	$-\dfrac{2c_0}{c_1-\sqrt{c_1^2-4c_0}}$
			$-\dfrac{c_1}{2}-\sqrt{\dfrac{c_1^2}{4}-c_0}$	$\dfrac{u}{2}-\dfrac{u^2}{4}-a_0$	$-\dfrac{c_0}{c_1-\sqrt{c_1^2-c_0}}$

Table B3. Numerical Values of SL_j, BI_j, and DI_J Obtained from Harrison's Equation of State

j	SL_j	BI_j	DI_j	d_j
1	4.609549D7	-1.207604D7	595.0918	0.2
2	1.023694D8	-4.706789D7	292.5459	0.4
3	1.703587D8	-1.035440D8	195.0306	0.6
4	2.526025D8	-1.810945D8	146.2729	0.8
5	3.521511D8	-2.785537D8	117.0184	1.0
6	4.731379D8	-3.945201D8	97.51529	1.2
7	6.196518D8	-5.230308D8	83.58454	1.4
8	7.906285D8	-6.534924D8	73.13647	1.6
9	1.008552D9	-7.885254D8	65.01020	1.8
10	1.256461D9	-8.397070D8	58.50918	2.0
11	1.586655D9	-1.060535D9	53.19016	2.2
12	2.031876D9	-1.358462D9	48.75765	2.4
13	2.664192D9	-1.780490D9	45.00706	2.6
14	3.634192D9	-2.429179D9	41.79227	2.8
15	5.312070D9	-3.56662D9	39.00612	3.0
16	8.898734D9	-5.974869D9	36.56824	3.2
17	2.20247D10	-1.472302D10	34.41716	3.4

APPENDIX C: Gas Release Data

Table C1. Summary of Gas Release Data Obtained by Small, Ref. 35, with the Sweep Gas Technique

Temp. (°C)	Release on Heating (%)	Isothermal Release (%)	Total Release (%)
1500	1.5	5.7	7.2
1600	9.3	0.5	9.8
1700	16.1	4.2	20.3
1800	26.4	1.6	28.0
1900	62.3	4.6	66.9
2000	53.4	9.4	62.8

Table C2. Summary of Gas Release Data Measured by Burbach and Zimmermann, Ref. 36

.Temp. (°C)	Burn-up (% FIMA)	Time (min)	Annealing FGR (%)
1800	0.3	2.5	3.9
1800	0.3	2.7	2.3
1800	0.3	16.7	21.0
1800	0.9	3.1	11.8
1800	0.9	5.1	12.3
1800	0.9	15.5	23.6
1800	0.9	30.0	14.6
1800	3.7	2.5	24.6
1800	3.7	5.5	22.2
1900	2.4	16.0	46.6
1900	3.7	3.2	24.4
1900	3.7	4.0	29.3
1900	3.7	4.8	26.6
1900	3.7	7.0	29.7
1900	3.7	15.0	43.2
2000	0.3	2.5	15.0
2000	0.3	4.7	10.1
2000	0.3	7.5	5.4
2000	0.3	15.5	13.2
2000	0.9	5.9	31.3
2000	3.7	2.9	28.4
2000	3.7	8.0	37.7
2000	3.7	15.5	41.9

Table C3. Summary of Gas Release Data[a] Obtained by Killeen and Baker, Ref. 37

Sample	Weight (mg)	Ramp (°C s^{-1})	Temp.[b] (°C)	Time (h)	Release at End of Anneal (%)	Expected Error[c] (%)
3001-A	148.0	0.060	1410	18	0.1	10
3001-B	148.0	0.060	1560	3	4.5	10
3002	211.9	0.077	1540	18	4.5	10
3003	268.8	0.082	1600	17	15.5	10
3004	613.2	0.10	1340	18	<0.1	10
3005	910.9	0.10	1450	64	20.5	15[d]
3006	495.9	0.10	1750	0.3	25.0	15[d]

[a]In Ar/2% H_2 atmosphere.

[b]Measured value. Sample temperature expected to be 10–20° higher.

[c]Expected error is due to calibration and background drift.

[d]Error is higher owing to furnace cracking, which made assessment of the gas flows uncertain. In particular, the fractional release can be expected to be low owing to loss of released gas before counting.

Table C4. Summary of Gas Release Data Obtained by Bridge, Cordall, and Young, Ref. 38

Pellet No.	Anneal	Annealing time (h) At 1400°C	Annealing time (h) At 1650°C	Total measured gas release (%)	Mean grain diameter with Std. Dev.(mm) Unannealed sample	Mean grain diameter with Std. Dev.(mm) Annealed sample
25	266/1	13.5	–	0.18	8.2 ± 1.2	–
25	266/2	12.5	–	5	8.2 ± 1.2	12.0 ± 2.4
22	5HT	12.5	7.25	29	9.4 ± 1.5	11.0 ± 2.0
20	6HT	15.75	7.25	11.23	9.4 ± 1.6	7.4 ± 2.7
24	8HT	12.75	13.75	2.86	8.0 ± 1.2	8.7 ± 2.4
19	9HT	14	12	0.13	8.0 ± 1.2	9.0 ± 1.2
19	10HT	11	50.5	0.37	8.0 ± 1.2	7.8 ± 1.3
10	10/2	–	28.5	25.84	9.5 ± 2.0	8.8 ± 1.6
10	10/3	–	19.5	23.32	9.5 ± 2.0	10.3 ± 1.7
10	10/4	19	23	11.93	9.5 ± 2.0	9.4 ± 1.5
10	10/5	12	18	3.60	9.5 ± 2.0	9.9 ± 1.2

Table C5. Summary of Series-1 (Sealed Capsule) Annealing Experiments by Small, Ref. 39

ID	Annealing Temp. (°C)	Dwell Time (s)	Heating Rate (°C s^{-1})	Specimen Mass (mg)	^{85}Kr Release (mCi ±10%)	^{85}Kr Release (% of Inventory)
1400/300	1400	300	13	51.9	0.02	0.01
1400/600	1400	600	18	47.6	0.02	0.01
1400/900	1400	900	57	30.0	0.42	0.34
1500/300	1500	300	50	72.7	1.72	0.58
1500/600	1500	600	20	52.8	0.11	0.05
1500/900	1500	900	20	28.7	0.09	0.09
1600/300	1600	300	62.5	80.3	9.01	2.75
1600/600	1600	600	20	58.3	4.59	1.93
1600/900	1600	900	62.5	68.0	14.71	5.30
1700/300	1700	300	75	77.2	34.15	10.84
1700/600	1700	600	60	111.8	103.05	44.50
1700/900	1700	900	64	65.2	100.8	37.90

Table C6. Summary of Gas Release Data Obtained by Zimmermann, Ref. 40

Temp. (°C)	Burnup (% FIMA)	Annealing Time (min)	FGR (%)
1400	2.4	180	3.2
1400	3.7	10	12.4
1400	3.7	30	17.4
1400	3.7	60	24.3
1400	3.7	360	12.5
1500	2.4	8	12.2
1500	2.4	30	16.9
1500	2.4	58	15.0
1500	2.4	120	20.8
1500	2.4	180	15.5
1500	3.7	8	19.6
1500	3.7	30	28.2
1500	3.7	180	38.3
1600	2.4	15	16.1
1600	2.4	55	27.5
1600	2.4	115	25.1
1600	3.7	8	28.8
1600	3.7	30	37.3

Table C7. Summary of Data from Fission-Product Release Tests Conducted on Commercial LWR Fuel by Collins, Osborne, Lorenz, and Malinauskas, Ref. 41

Characteristic/Parameter	Test Number					
	HI-1	HI-2	HI-3	HI-4	HI-5	HI-6
Specimen source[a]	HBR	HBR	HBR	PB	Oco	Mont
Specimen length (mm)	203	203	203	203	152	152
Specimen mass[b] (g)	168	166	167	306	133	170
Fuel burnup (MWd/kg)	28.1	28.1	25.2	10.1	38.3	40.3
In-reactor gas release (%)	0.3	0.3	0.3	10.2	4.1	2.0
Steam flow rate (g/min)	0.81	0.76	0.31	0.29	0.30	1.7[c]
Test heatup rate (K/s)	1.2	1.3	2.1	2.3	1.1	2.3
Test temperature (K)	1675	2000	2275	2200	2025	2250
Effective time at test temperature[d] (min)	33.8	22.5	21.3	21.6	21.5	2.5
UO_2 grain size (mm)						
Pretest	2.8	2.8	2.8	6.6	9.2	–
Posttest	3.4	3.9	4.3	6.6	8.9	–
Fuel/cladding interaction	None	Minor	Yes	Yes	Minor	Yes
^{85}Kr fission product release[e] (% of inventory)	3.13	51.8	59.3	31.3	19.9	31.6

[a]Reactors: HBR = H. B. Robinson 2, PB = Peach Bottom 2, Oco = Oconee 1, Mont = Monticello.

[b]Total of UO_2 and Zircaloy.

[c]Average value over test time; rate varied from 0.2 to 2.4 g/min during test.

[d]Includes estimates for heatup and cooldown effects.

[e]Includes ^{85}Kr released during reactor operation.

Table C8. Summary of Gas Release Data Obtained by Parker and Barton, Ref. 42, for UO_2 Heated 5.5 h in Pure Helium

Temp. (°C) (°F)	Irradiation Level (Mwd/ton)[a]	Xe–Kr Gas Release (%)
1400	≈1	0.8
2552	1005	0.8
	1000	0.5
	4000	6.1
1610	≈1	2.7
2930	1005	2.6
	1000	6.0
	4000	14.0
1780	≈1	3.7
3236	1005	12
	1000	14
	4000	42
1980	≈1	12
3596	1005	29
	1000	49
	4000	71

[a]Only the 1 Mdw/ton pellets were full size (7 g). The high-burnup samples were 0.1–0.2-g fragments, with a total weight of 1–2 g.

Appendix D: Mobility of Fission-Gas Bubbles during Normal and Transient Conditions

The Mobility of Overpressurized Fission-Gas Bubbles

The physical basis for this approach is as follows. During equilibrium conditions, bubbles may be faceted, and the rate of motion of a faceted bubble is determined by the frequency of nucleation of steps instead of by the time required for atoms to move from a step on one side of a bubble to a step on the other side.[18] (That is, the atom attachment and detachment rates are slower than predicted by surface diffusion.) However, if the atom attachment and detachment rates increase during transient conditions, higher bubble diffusivities will result.

Because plastic deformation of the UO_2 due to an overpressurized bubble is expected to result in a high density of dislocations around the bubble surface, the diffusivity of such a bubble (if otherwise restricted in its mobility, as the steady-state model assumes) would be expected to increase rapidly. In effect, bubble diffusion would depend more on the time required for atoms to move from a step on one side of a bubble to a step on the other (i.e., surface diffusion) than on the frequency of nucleation of steps.

A Model for the Diffusion of Overpressurized Fission-Gas Bubbles

In an attempt to quantify the ideas presented above, consider the excess internal gas pressure in a bubble of radius r_i that is given by

$$P_i^{ex} = P_i^g(T) - 2\gamma / r_i, \tag{D1}$$

where γ is the effective surface tension and

$$P_i^g(T) = f(r_i, n_i)T \tag{D2}$$

is the gas pressure within the bubble at temperature T. Equation (D2) represents any general gas law where the internal gas pressure is linearly dependent on temperature (ideal gas behavior, Van der Waals, etc.) and $f(r_i,n_i)$ is, in general, a function of the bubble radius and the number n_i of gas atoms/bubble. The term P_i^{ex} is a measure of the resultant pressure

transmitted to the matrix, which vanishes under the initial equilibrium conditions. In Eq. D1, the effect of external stresses has been neglected. Consider a time interval, Δt (s), of the transient during which the fuel temperatures are increasing at a rate dT/dt (°C/s). During this time interval,

$$T = T_1 + \frac{dT}{dt}\Delta t, \tag{D3}$$

where T_1 is the fuel temperature at the beginning of the time interval Δt, and

$$P_i^g(T_1) = f(r_i, n_i)T_1 . \tag{D4}$$

First consider the case where the bubble radius r_i is constant over the time interval Δt. The time τ_i required for the bubble to acquire an excess pressure sufficient to generate an equivalent stress equal to the yield stress σ_y of the surrounding matrix is, using Eqs. D1-D4, given by

$$\tau_i^y = \frac{\sigma_y r_i T_1}{(3\gamma dT/dt)}. \tag{D5}$$

Equation D5 does not take into account the situation in which the bubble may be overpressurized prior to the beginning of time interval Δt. If the bubble was initially in an overpressurized state, Eq. D5 would overestimate the time required for the equivalent stress generated by the overpressurized bubble to become equal to σ_y. On the other hand, if appreciable bubble relaxation occurred during time τ_i^y (i.e., r_i increases), Eq. D5 would underestimate the time required for the equivalent stress generated by the overpressurized bubble to become equal to σ_y.

A rigorous approach to the calculation of the excess internal gas pressure for each bubble of radius r_i, where i varies over the limits of the bubble size distribution, requires the numerical solution of a large set of coupled partial differential equations for the rate of change of bubble radii and the rate of change of the lattice vacancy concentration c_v. Because of code running-time requirements, this approach is outside the scope of FASTGRASS. However, a phenomenological approach to the problem of

bubble overpressurization can be formulated by evaluating τ_i^y as given by Eq. D5 with respect to the bubble relaxation time, τ_i^B.

Let α_i ($0 \le \alpha_i \le 1$) characterize the degree of nonequilibrium in the lattice surrounding a bubble of radius r_i: the larger α_i, the farther the system is from an equilibrium configuration. The change in α_i can be written in terms of α_i and times τ_i^y and τ_i^B as

$$d\alpha_i = (1-\alpha_i)d\left(\tau_i^B / \tau_i^y\right). \tag{D6}$$

Thus, as τ_i^y decreases and τ_i^B increases, the system departs further from its equilibrium configuration. Conversely, as τ_i^y increases and τ_i^B decreases, the system approaches equilibrium. Solving Eq. D6 for α_i gives

$$\alpha_i = 1.0 - \exp\left(-\tau_i^B / \tau_i^y\right). \tag{D7}$$

The bubble relaxation time in Eq. D7, τ_i^B, is given by

$$\tau_i^B(t) = \frac{r_i^s}{C_v^e D_v}, \tag{D8}$$

where C_v^e is the fractional equilibrium vacancy concentration, given by

$$C_v^e = \exp\left(-E_v^f / kT\right), \tag{D9}$$

and D_v is the vacancy diffusion coefficient, given by

$$D_v = D_v^o \exp\left(-E_v^m / kT\right), \tag{D10}$$

where E_v^f and E_v^m are the vacancy formation and migration energies, respectively, and D_v^o is a preexponential factor.

The problem that remains is to relate α_i to bubble diffusivity. This can be accomplished by considering the limits of the bubble diffusivities used in FASTGRASS. During steady-state conditions (i.e., $\alpha_i << 1$), empirical intragranular diffusivities are given by[46]

$$D_i^l = 2.1x10^{-4} \exp(-91{,}000 / kT)(r_l / r_i)^{1.62} \text{ cm}^2/\text{s}. \qquad \text{(D11)}$$

Equation D11 is limited by constraints of compatibility with theoretical treatments of bubble mobility by surface diffusion. The diffusivity of a bubble moving by surface diffusion is given by

$$D_i^s = 2.42x10^{-25} \exp(-108{,}000 / kT) / r_i^4 \text{ cm}^2/\text{s}. \qquad \text{(D12)}$$

Based on the discussions above, the bubble diffusivities during transient heating conditions should be given by Eq. D12 as $\alpha \rightarrow 1$. Thus, using Eqs. D11 and D12, the fission-gas bubble diffusivities can be expressed in terms of the equilibrium parameter, α_i, as

$$D_i = \frac{4.9202x10^{-11} \exp\left[-(91{,}000 + 17{,}000\alpha_i) / kT\right]}{(3365.51 r_i)^{(1.62+2.38\alpha_i)}} \text{ cm}^2/\text{s}, \qquad \text{(D13)}$$

where r_l of Eq. D11 is the radius of a gas atom (0.24×10^{-7} cm). The form of Eq. D13 was chosen to make log D_i a linear function of α_i, i.e., log $Di = \log D_i^l + (\log D_i^s - \log D_i^l)\, \alpha i$.

When $\alpha i \rightarrow 0$, Eq. D13 approaches Eq. D11 for bubble diffusivities based on the isothermal results of Cornell[14] and Gulden.[19] When $\alpha i \rightarrow 1$, Eq. D13 approaches Eq. D12 for bubble diffusivities based on the theory of surface diffusion. For intermediate values of α_i, Eq. D13 lies between the values given by the empirical expression (as a lower limit) and those obtained from the theory of surface diffusion (as an upper limit).

Equation D13 is unique in the sense that it relates bubble diffusivities to fuel yield stress, heating rate, and vacancy mobility, as well as to fuel temperature and bubble radius.

To use Eq. D13, the UO_2 yield stress, σ_y, in Eq. D5 must be determined. In general, σ_y is a complex function of fuel temperature, strain rate, and microstructure (e.g., UO_2 grain size). Experiments designed to measure the UO_2 yield stress under steady-state and transient in-reactor conditions are difficult to perform and adequate data are lacking. The UO_2 yield stress used in the calculation of gas bubble diffusivities, as given by Eq. D13, has

been determined based on the data of Roberts,[80] who conducted conventional load-versus-deflection, strain rate change, and stress relaxation tests on UO_2 20 wt.% PuO_2 specimens in the strain rate range of 0.1-0.4 h^{-1} and at temperatures from 1500 to 1800°C. The specimen, prepared from mechanically blended powders with grain sizes ranging from 2 to 14.5 μm, were deformed in four-point bending in a high-temperature, inert-atmosphere furnace. The most significant observations from these experiments are the strong temperature dependence of the flow stress (flow stress decreases as the temperature increases) and the increase in flow stress with an increase in grain size (in these experiments, the flow stress corresponds to the proportional elastic limit stress).

An analytical expression for the yield stress as a function of the temperature and grain size was obtained from Roberts' data[80] by quadratic regression analysis. Explicitly, for σ_y (in dyn/cm^2),

$$\sigma_y = 9.8 \times 10^5 \exp(\alpha_0 + \alpha_1/T + \sigma_2/T^2) , \qquad \text{(D14)}$$

where

$$\sigma_0 = -57.364866 - 7.0264656d + 0.52281105d^2,$$

$$\sigma_1 = 1.9840863 \times 10^5 + 2.9969484 \times 10^4 d - 2.07175 \times 10^3 d^2,$$

and

$$\sigma_2 = -1.4947535 \times 10^8 - 3.0994649 \times 10^7 d + 2.0330226 \times 10^6 d^2.$$

Equation D14 assumes temperatures between 1500 and 1800°C and grain sizes, d, between 2.0 and 14.5 μm. No further change in the ratio τ_i^B / τ_i^y of Eq. D7 was assumed (all other parameters remained fixed) for temperatures <1500°C or >1800°C.

References

1. R. Wilson, Rev. Mod. Phys. **57**, p. 1, Part II, SI (1985).

2. J. Rest, D. J. Osetek, and J. K. Hartwell, "Isotopic Fission Product Release from Nuclear Fuel under Severe Core Damage Accident Conditions," in *Proc. IAEA Int. Symp. on Source Term Evaluation for Accident Conditions*, IAEA–SM 281/15, International Atomic Energy Agency, Vienna, p. 105 (1986).

3. M. J. Bell, ORIGEN—*The ORNL Isotope Generation and Depletion Code*, ORNL–4628, Oak Ridge National Laboratory, Oak Ridge, TN (May 1973).

4. H. Matzke, *Radiat. Eff.* **53**, 219 (1980).

5. Z. Ronchi and H. Matzke, *J. Nucl. Mater.* **45**, 15 (1973).

6. E. E. Gruber, *Calculation of Transient Fission–Gas Release from Oxide Fuels*, ANL–8143 (1974).

7. J. Rest, *Nucl. Technol.* **56**, 553 (1982).

8. J. Rest, *Nucl. Technol.* **61**, 33 (1983).

9. J. Rest, *J. Nucl. Mater.* **120**, 195 (1984).

10. J. Rest, *J. Nucl. Mater.* **131**, 291 (1985).

11. J. Rest, *Adv. Ceram.* **17**, 223 (1986).

12. J. Rest and A. W. Cronenberg, *J. Nucl. Mater.* **150**, 203 (1987).

13. A. A. Solomon, A. Casagrowda, and J. Rest, *J. Nucl. Mater.* **154**, 332 (1988).

14. J. Rest, *J. Nucl. Mater.* **168**, 243 (1989).

15. J. Rest, *GRASS–SST: A Comprehensive Mechanistic Model for the Prediction of Fission–Gas Behavior in UO2–Base Fuels during Steady–State and Transient Conditions*, NUREG/CR-2437 Vol. I, ANL–78–53 (June 1978).

16. C.–Y. Li, J. Rest, S. Danyluk, and R. B. Poeppel, "GRASS–Code Calculation for the Behavior of Helium in Austenitic Stainless Steels," *in Proc. 2nd ANS Topical Mtg. on the Technology of Controlled Nuclear Fusion*, CONF–760935–PI, Richland, WA, p. 239 (1976); ANL/FPP/TM–74, p. 200 (1977)

17. J. Rest and R. C. Birtcher, *J. Nucl. Mater.* **168**, 312 (1989).

18. J. Rest, G. L. Hofman, and R. C. Birtcher, "The Effect of Crystal Structure Stability on The Swelling in Intermetallic Uranium Compounds," in *Effects of Radiation on Materials: 14th Int. Symp.* ASTM STP 1046, Vol. II, Eds., M. H. Pachan, R. E. Staller, and A. S. Kumar, American Society for Testing and Materials, Philadelphia, p. 789 (1990).

19. J. R. Matthews and M. H. Wood, *Nucl. Eng. Des.* **56**, 439 (1980).

20. E. E. Gruber, *The Role of Bubble–Size Equilibration in the Transient Behavior of Fission Gas*, ANL–78–36 (April 1978).

21. M. V. Speight and W. Beere, *Met. Sci.* **9**, 190 (1975).

22. J. W. Harrison, *J. Nucl. Mater.* **31**, 99 (1969).

23. C. Ronchi, *J. Nucl. Mater.* **96**, 314 (1981).

24. J. Rest, "The Effect of Fission-Gas Bubble Behavior on Microcracking and Fuel Response during Transient Heating of LWR Fuel," in *Proc. Topical Mtg. Fission Product Behavior and Source Term Research*, American Nuclear Society, LaGrange Park, IL, pp. 2-388 (1984).

25. M. F. Osborne, R. A. Lorenz, K. S. Norwood, and R. P. Wichner, "Fission Product Release under LWR Accident Conditions," *in Proc. Int. Mtg. on Light Water Reactor Severe Accident Evaluation*, American Nuclear Society, LaGrange Park, IL pp. TS–4.1–1 (1983).

26. D. J. Osetek et al., in *Proc. Topical Mtg. Fission Product Behavior and Source Term Research*, American Nuclear Society, LaGrange Park, IL, pp. 22-1 (1984).

27. M. V. Speight and G. W. Greenwood, Philos. Mag. **9**, 683 (1964) .

28. D. R. Olander, *Fundamental Aspects of Nuclear Reactor Fuel Elements*, TID-26711-P1, U.S. Technical Information Center, U.S. ERDA, Springfield, VA, p. 320 (1976).

29. J. Belle, in *Uranium Dioxide*, U.S. Government Printing Office, Washington, DC, p. 512 (1961).

30. J. T. Bittel, L. H. Sjodahl, and J. F. White, J. Am. Ceram. Soc. **52**, 445 (1969).

31. J. R. Macewan and J. Hayashi, Proc. Brit. Ceram. Soc. **7**, 245 (1967).

32. J. A. Turnbull, *A Review of Rare Gas Diffusion in Uranium Dioxide*, RD/B/N2405, Berkeley Nuclear Laboratories, Berkeley, GLOS, UK (1972).

33. C. Ronchi and H. Matzke, J. Nucl. Mater. **45**, 15 (1972).

34. J. R. Matthews and M. H. Wood, J. Nucl. Mater. **84**, 125 (1979).

35. G. J. Small, *Fission Gas Release from Uranium Dioxide in High-Temperature Transients*, AERER 12956, Harwell Laboratory, United Kingdom (May 1988).

36. J. Burbach and H. Zimmermann, *Spaltgasverhalten in Bestrahltem UO_2 bei Out-of-Pile-Glühungen*, PNS-Nr. 893/85, Kernforschungszentrum Karlsruhe (June 1985).

37. J. C. Killeen and C. Baker, "Fission Gas Releases during Postirradiation Annealing of UO_2 up to 1750°C," in *Proc. Conf. on LWR Fuel Performance*, Vol. 2, American Nuclear society, LaGrange Park, IL, pp. 4-69 (1985).

38. D. G. Bridge, P. Cordall, and J. Young, *Fission-gas Releases during Post-irradiation Annealing of UO_2 Fuel from WAGR Pins of Burn-up to 5500 MWd/te U*, ND-R-720 (W), Windscale Nuclear Power Development Laboratories, Windscale Cumbria, United Kingdom (July 1982).

39. G. J. Small, "Bubble Development and Fission Gas Release during Rapid Heating of 18 GWd/TeV UO_2," in *Proc. IAEA Specialists' Meeting on Fission Product Release and Transport in Gas-Cooled Reactors*, Berkeley Nuclear Laboratories, Berkeley, GLOS, UK, p. 891 (October 1985).

40. H. Zimmermann, Eur. Appl. Res. Rep.-Nucl. Sci. Technol. **5**, 1349 (1984).

41. J. Collins, M. F. Osborne, R. A. Lorenz, and A. P. Malinauskas, Nucl. Technol. **81**, 78 (1988).

42. G. W. Parker and C. W. Barton, in *The Technology of Nuclear Reactor Safety*, Vol. 2, Eds. T. J. Thompson and J. G. Beckerley, MIT Press, Cambridge, MA, p. 574 (1983).

43. D. A. MacInnes and I. R. Brearly, J. Nucl. Mater. **107**, 123 (1982).

44. C. Ronchi, J. Nucl. Mater. **148**, 316 (1987).

45. I. R. Brearly, P. E. Coleman, P. T. Elton, and D. A. MacInnes, "Thermal Re-solution into Oxide Fuels," in *Proc. Workshop on Fission Gas Behaviour in Safety Experiments*, Ed., F. K. Schmitz, Harwood Academic Publications, London, p. 1159 (1984).

46. R. M. Cornell, *Philos. Mag.* **19**, 539 (1969).

47. A. Holt and H. Matzke, *J. Nucl. Mater.* **48**, 157 (1973).

48. J. Belle, *J. Nucl. Mater.* **30**, 3 (1969).

49. H. Matzke, *Adv. Ceram.* **17**, 1 (1986).

50. M. H. Wood, *J. Nucl. Mater.* **78**, 58 (1978).

51. J. J. Carey and R. A. Valentin, *Evaluation of a Class of Methods for Bounding Steady-State Creep Deformation*, ANL-8016 (February 1974).

52. H. Matzke, in *Harwell Consultant's Symp. on Inert (Rare) Gases in Metals and Ionic Solids*, UKAEA Research Report AERE R-9733, Vol. 2, p. 345 (1980).

53. P. C. Bell and E. F. P. Newson, *Statistics for Business with MINITAB*, The Scientific Press, Palo Alto, California (1985).

54. G. J. Small and D. A. MacInnes, *Singar "A" and "B": Simplified Models for Fission Gas Release in Transients*, AERE R 12803, Harwell Laboratory, United Kingdom (March 1988).

55. C. Baker, Eur. Appl. Phys. Rep.-Nucl. Sci. Technol. **1**, 1 (1979).

56. H. Zimmermann, "Fission Gas Release and Fission Gas Retention in Oxide Fuels, in *Proc. Workshop on Fission Gas Behavior in Nuclear Fuels*, European Institute for Transuranium Elements, Karlsruhe, Germany, p. 35 (1978).

57. C. C. Dollins and F. A. Nichols, *J. Nucl. Mater.* **66**, 143 (1977).

58. J. A. Turnbull and C. A. Friskney, *J. Nucl. Mater.* **58**, 31 (1975).

59. J. Rest, M. C. Billone, and V. Z. Jankus, in *Steady-State LWR Fuel-Rod Performance Code Development, Light-Water Reactor Safety Research Program: Quarterly Progress Report*, ANL-76-121, p. 50 (Dec. 1976).

60. R. M. Cornell, M. V. Speight, and B. C. Masters, *J. Nucl. Mater.* **30**, 170 (1969).

61. H. Zimmermann, "Investigations of Swelling in Oxide Fuels," in *Proc. Workshop on Fission Gas Behavior in Nuclear Fuels*, European Institute for Transuranium Elements, Karlsruhe, Germany, p. 127 (1978).

62. S. M. Gehl, M. G. Seitz, and J. Rest, *Fission Gas Release from Irradiated PWR Fuel during PCM-Type Accidents*, NUREG/CR-0088, ANL-77-80 (May 1978).

63. R. J. DiMelfi and L. W. Deitrich, *Nucl. Technol.* **43**, 328 (1979); ANL/RAS-78-32 (1978).

64. S. W. Tam, P. E. Blackburn, and C. E. Johnson, "Effect of Core Chemistry on Fission Product Release," in *Proc. Int. Mtg. on Thermal Nuclear Reactor Safety*, American Nuclear Society, Chicago, IL, p. 101 (1983).

65. H. Kleykamp, *J. Nucl. Mater.* **131**, 221 (1985).

66. P. Hofmann and J. Spino, *Nucl. Mater.* **127**, 205 (1985).

67. *Report of the Special Committee on Source Terms*, American Nuclear Society, LaGrange Park, IL (September 1984).

68. P. E. Blackburn and C. E. Johnson, *Light Water Reactor Fission Data Assessment*, ANL-82-42 (September 1982).

69. A. W. Cronenberg and D. J. Osetek, *J. Nucl. Mater.* **149**, 252 (1987).

70. A. W. Cronenberg and D. J. Osetek, "Analysis of Iodine Chemical Form for the Severe Fuel Damage Scoping Test and 1-1 Test," in American Chemical Society *Severe Accident Chemistry Symp.*, p. 252 (1986).

71. R. A. Lorenz, J. L. Collins, A. P. Malinauskas, O. L. Kirkland, and R. L. Towns, *Fission Product Release from Highly Irradiated LWR Fuel*, NUREG/CR-0722, Oak Ridge National Laboratory, Oak Ridge, Tennessee (Feb. 1980).

72. R. A. Lorenz, J. L. Collins, A. P. Malinauskas, M. F. Osborne, and R. L. Towns, *Fission Product Release from Highly Irradiated LWR Fuel Heated to 1300-1600°C in Steam*, NUREG/CR-1386, Oak Ridge National Laboratory, Oak Ridge, Tennessee (Nov. 1980).

73. M. F. Osborne, R. A. Lorenz, J. R. Travis, and C. S. Webster, *Data Summary Report for Fission Product Release Test HI-1*, NUREG/CR-2928, Oak Ridge National Laboratory, Oak Ridge, Tennessee (Dec. 1982).

74. R. R. Hobbins, C. E. Johnson, R. A. Lorenz, A. R. Taig, and R. C. Voegl, "An Overview of Fission Product Release Experiments," in *Proc. Topical Mtg. Fission Product Behavior and Source Term Research*, American Nuclear Society, LaGrange Park, IL, p. 1-1 (1984).

75. R. V. Strain, J. E. Sanecki, and M. F. Osborne, "Fission Product Release from Irradiated LWR Fuel under Accident Conditions," in *Proc. Topical Mtg. Fission Product Behavior and Source Term Research*, American Nuclear Society, LaGrange Park, IL, p. 2.1 (1984).

76. D. J. Osetek, "Results of the Four PBF Severe Fuel Damage Tests," in *Transactions of the Fifteenth Water Reactor Safety Information Meeting*, National Bureau of Standards, Gaithersburg, MD, NUREG/CP–0090, p. 1 (1987).

77. D. A. Petti, Z. R. Martinson, R. R. Hobins, C. M. Allison, E. R. Carlson, D. L. Hagrman, T. C. Cheng, J. K. Hartwell, K. Vinjamuri, and L. J. Seifken, *Power Burst Facility (PBF) Severe Fuel Damage Test 1–4 Test Results Report*, NUREG/CR–5163, EG&G, Idaho (1989).

78. *Technical Basis for Estimating Fission Product Behavior during LWR Accidents*, NUREG–0772 U. S. Nuclear Regulatory Commission (June 1981).

79. S. M. Gehl, "UO_2-Zircaloy Reaction and Fission-Product Release under Steam Oxidizing Conditions," in *Proc. ANS Topical Mtg. on Reactor Safety Aspects of Fuel Behavior*, Vol. 2, American Nuclear Society, LaGrange Park, IL, p. 2 (1981).

80. J. T. A. Roberts, "High–Temperature Plasticity of Oxide Nuclear Fuel," in *Symp. Plastic Deformation of Ceramics*, The Pennsylvania State University, p. 1 (1974).

Distribution for NUREG/CR-5840 (ANL-92/3)

Internal

D. R. Diercks
P. E. Domagala
C. A. Malefyt (2)
P. J. Peterson
J. Rest (20)
W. J. Shack
C. E. Till
R. W. Weeks
S. A. Zawadzki
ANL Patent Dept.
ANL Contract File
TIS Files (3)

External

NRC, Washington, for distribution per R3
ANL Libraries (2)
Chicago Operations Office, DOE:
- D. T. Goldman
- F. Herbaty
- A. L. Taboas

Materials and Components Technology Division Review Committee:
- H. Berger, Industrial Quality, Inc., Gaithersburg, MD
- H. Birnbaum, University of Illinois at Urbana–Champaign, Urbana
- R. Buchanan, University of Illinois at Urbana–Champaign, Urbana
- M. S. Dresselhaus, Massachusetts Institute of Technology, Cambridge, MA
- R. A. Greenkorn, Purdue University, West Lafayette, IN
- B. Jones, University of Illinois at Urbana–Champaign, Urbana
- C.-Y. Li, Cornell University, Ithaca, NY
- R. E. Smith, Electric Power Research Institute, NDE Ctr., Charlotte, NC